



ALGERIAN DEMOCRATIC AND POPULAR REPUBLIC
MINISTRY OF HIGHER EDUCATION AND SCIENTIFIC RESEARCH

UNIVERSITY OF SAAD DAHLAB BLIDA 1
INSTITUTE OF AERONAUTICAL AND SPACE STUDIES
AIRCRAFT CONSTRUCTION DEPARTMENT

Final Study Master's Dissertation
Option: SPACE PROPULSION

**Supersonic Flow and Combustion Behavior in a
Dual-Cavity Scramjet: A CFD Study with Global and
Detailed Chemistry**

Realized by:
Mugaba Mvusi Khanya

Supervised by:
Dr. R. RENANE
Dr. R. ALLOUCHE

Defense Date: 07/07/2025

Members of the Jury:

Name	Role
Dr. Neche Ahmed	President
Dr. R. Renane	Supervisor
Dr. R. Allouche	Supervisor
Dr. Bekka Nadir	Examiner
Dr. Oueld Bessi Hamid	Examiner

Academic Year: 2024/2025

Dedication

I dedicate this thesis to my family, mentors, and those who have supported my path from modest origins to the quest for excellence.

To my parents and cherished ones, your steadfast support, sacrifices, prayers, and faith in me have profoundly influenced my development.

To my lecturers and mentors, whose guidance has fostered my intellectual development, your wisdom and encouragement have ignited my enthusiasm for aerospace and space propulsion.

To my friends and colleagues, your support and companionship have rendered the hardships of this trip meaningful.

I dedicate this work to my homeland, Zimbabwe, and to the aspirants throughout Africa who courageously strive for greatness. Let us persist in dismantling impediments and advancing the future of space exploration.

I express my gratitude to God, whose grace has supported me through every adversity, and whose favors continue to facilitate my progress.

This is not the conclusion, but a precursor to even bigger achievements.

MUGABA MVUSI KHANYA

Acknowledgements

First and foremost, I would like to sincerely thank my family and friends. Your constant support, encouragement, and belief in me have been my foundation throughout this academic journey. Without your patience and understanding, completing this thesis would not have been possible.

I am deeply grateful to my supervisors, Mr. Renane and Mr. Allouche, for their expert guidance, patience, and insightful advice throughout this research. Your mentorship has been invaluable in shaping this work and helping me grow as a researcher.

I also wish to thank the Chairman and members of the Jury for taking the time to evaluate my thesis and provide constructive feedback, which will be essential for the further development of this study.

My thanks extend to the faculty and staff of the Institute for their dedication and support. The knowledge and skills I acquired here have been crucial for carrying out this project. Special appreciation goes to the professors whose encouragement and help have been motivating throughout.

To my classmates and friends, thank you for your friendship, teamwork, and the countless memorable moments shared during this journey. Your support made even the toughest days manageable and enjoyable.

Finally, I am grateful to everyone who contributed their time and insights for this research. Your input has enriched this thesis and added valuable perspectives.

This work is a reflection of all the support and inspiration I have received, and I thank each of you from the bottom of my heart.

Abstract

This thesis presents a numerical investigation of supersonic combustion within a scramjet combustor featuring a double parallel cavity geometry, analyzed across varying inlet Mach numbers. Using ANSYS Fluent, the study solves the Reynolds-averaged Navier-Stokes (RANS) equations with the standard k -epsilon turbulence model to capture turbulent flow behavior. A finite-rate/eddy dissipation model is employed to simulate the chemical kinetics of combustion.

The research focuses on how the double parallel cavity configuration affects flame stabilization, fuel-air mixing, and combustion efficiency at different supersonic flow conditions. Comparative analysis of results at various Mach numbers provides insights into optimizing combustor design and operating parameters for enhanced scramjet performance.

Model validation is achieved by comparing simulation outcomes with experimental data to ensure accuracy and reliability. This work contributes to the advancement of supersonic combustion understanding and supports the development of more efficient propulsion systems for high-speed aerospace applications.

Keywords: supersonic combustion, scramjet, double parallel cavity, Mach number, RANS, numerical simulation, propulsion

Résumé

Ce mémoire présente une étude numérique de la combustion supersonique dans une chambre de combustion de statoréacteur (scramjet) dotée d'une géométrie à double cavité parallèle, analysée pour différentes valeurs du nombre de Mach à l'entrée. L'étude, réalisée avec ANSYS Fluent, résout les équations de Navier-Stokes moyennées (RANS) en utilisant le modèle de turbulence standard $k-\varepsilon$ pour capturer le comportement turbulent de l'écoulement. Un modèle de dissipation/échange-fini est utilisé pour simuler la cinétique chimique de la combustion.

L'étude se concentre sur l'influence de la configuration à double cavité parallèle sur la stabilisation de la flamme, le mélange carburant-air et le rendement de combustion dans des conditions d'écoulement supersonique variées. L'analyse comparative des résultats à différents nombres de Mach fournit des indications sur l'optimisation de la conception et des paramètres de fonctionnement de la chambre de combustion pour améliorer la performance du statoréacteur.

La validation du modèle est effectuée par comparaison avec des données expérimentales afin de garantir la précision et la fiabilité des résultats. Ce travail contribue à l'avancement de la compréhension de la combustion supersonique et au développement de systèmes de propulsion plus performants pour les applications aérospatiales à grande vitesse. **Mots-clés** : combustion supersonique, super-statoréacteur, double cavité parallèle, nombre de Mach, RANS, simulation numérique, propulsion

الملخص

يقدم هذا البحث دراسة عددية لاحتراق فوق صوتي داخل غرفة احتراق لمحرك نفاث فائق السرعة (Scramjet) تتميز بهندسة ذات تجويفين متوازيين. وقد تم تحليلها لعدة قيم لعدد ماخ عند المدخل. تم تنفيذ الدراسة باستخدام برنامج ANSYS Fluent، حيث تم حل معادلات Navier-Stokes المتوسطة (RANS) باستخدام نموذج الاضطراب القياسي $k-\epsilon$ لتمثيل السلوك الاضطرابي للجريان. كما تم استخدام نموذج للتبدد/التفاعل الكيميائي المحدود لمحاكاة الحركية الكيميائية للاحتراق.

تركز الدراسة على تأثير تكوين التجويفين المتوازيين على استقرار اللهب، وامتزاج الوقود بالهواء، وكفاءة الاحتراق تحت ظروف مختلفة من الجريان فوق الصوتي. توفر التحاليل المقارنة للنتائج عبر قيم مختلفة لعدد ماخ مؤشرات مهمة لتحسين تصميم غرفة الاحتراق ومعلومات تشغيلها بهدف رفع أداء المحرك النفاث.

تم التحقق من صحة النموذج من خلال مقارنته مع بيانات تجريبية لضمان دقة وموثوقية النتائج. وتساهم هذه الدراسة في تطوير *الفهم العلمي لعملية الاحتراق فوق الصوتي، وفي تطوير أنظمة الدفع ذات الأداء العالي المخصصة للتطبيقات الجوية والفضائية عالية السرعة.

الكلمات المفتاحية: الاحتراق فوق الصوتي، محرك نفاث فائق السرعة، تجويف مزدوج متوازي، عدد ماخ، RANS، المحاكاة العددية، الدفع.

Contents

Dedication	i
Abstract	iii
Résumé	iv
ص غ ل م ل ا	v
Nomenclature	vi
General Introduction	xi
1 Overview of Supersonic Combustion	1
1.1 Scramjet	1
1.1.1 What is Supersonic Combustion	1
1.1.2 Why Supersonic Combustion	2
1.1.3 Prospective applications	2
1.1.4 Challenges and technological advancements in Supersonic Combustion	3
1.1.5 History of Ramjet and Scramjet Development	6
1.2 State of the Art	7
1.2.1 Plasma-Assisted Combustion	7
1.2.2 Endothermic Fuels and Reduced Chemical Mechanisms	7
1.2.3 Reduced-Order Models and Surrogate Fuels	8
1.2.4 Summary of Key Studies	8
1.3 Project Presentation	8
1.3.1 Geometry Description and Configuration	8
1.3.2 Boundary Conditions	9
1.3.3 Rationale for Geometry Choice	9
1.4 Conclusion	10
2 Mathematical Modelling	11
2.1 Introduction	11
2.2 Mathematical Modelling of Reacting Flows	11
2.3 Computational Fluid Dynamics	13
2.3.1 Governing Equations	13
2.3.2 Finite Volume Method	14
2.4 Turbulence Modelling	14
2.4.1 Turbulence Modelling with the Standard $k-\epsilon$ Model	14
2.4.2 Near-Wall Modelling and the Log-Law of the Wall	16
2.4.3 Sources of Error and Uncertainty in CFD	16
2.4.4 Practical Application in Scramjet Combustor	16
2.5 Combustion Modelling	17
2.5.1 Finite-Rate Chemistry	17
2.5.2 Reaction Mechanism	18

2.5.3	Probability Density Function (PDF) Model	18
2.5.4	Finite-Rate/Eddy Dissipation Model	19
2.5.5	ARCHIMEDES Model	19
2.6	Reference pressure	20
2.7	Solver Description	20
2.8	Stoichiometric Fuel-to-Air Ratio and Equivalence Ratio Calculation	21
2.8.1	Link Between Static Pressure and Equivalence Ratio	21
2.9	Conclusion	22
3	Numerical Modelling and ANSYS Procedure	23
3.1	Scope and Software Tools	23
3.2	Modeling the Flow in ANSYS CFX	24
3.3	Geometry	24
3.3.1	Formulation of the Geometry	24
3.4	Different combustion chamber geometries used in the study of scramjet	25
3.5	Mesh and mesh Sensibility studies	25
3.5.1	High-quality computational meshes for each combustor geometry	25
3.6	Evaluation of mesh quality metrics	27
3.6.1	Skewness	27
3.6.2	Orthogornal quality	28
3.7	2D simulation Boundary Conditions	30
3.8	Fluent Setup	31
3.8.1	Lauch Fluent	31
3.8.2	General	32
3.8.3	Model ,turbulence,Energy Activation in Fluent	33
3.8.4	Species Model Configuration:	34
3.8.5	combustion mechanism	34
3.8.6	Materials Definition	34
3.8.7	Setup of Boundary Conditions:	35
3.8.8	Reference Values	37
3.8.9	Solution Methods:	38
3.8.10	Solution Controls	39
3.9	Initialization:	39
3.10	Run Simulation:	40
3.11	Conclusion	41
4	Results and Discussion: Cold Flow	42
4.1	Introduction	42
4.1.1	Inlet Conditions Used	42
4.2	Description and Discussion of Cold Supersonic Flow Key Contours and Flow Structures	43
4.3	Visualisation of Cold Supersonic Flow Key Contours and Flow Structures	44
4.3.1	Temperature Contours	44
4.3.2	Pressure Contours at different mach inlet values.	45
4.3.3	Velocity Contours at different mach inlet values.	46
4.3.4	Density Contours for different inlet mach number values.	47
4.3.5	Enthalpy Contours for the double cavity combustor at different inlet mach number values	48

4.3.6	Hydrogen mass fraction contour for double cavity combustor at different inlet mach number values.	49
4.4	Validation of the results	51
4.5	Conclusion – Cold Flow Simulation	52
5	Results and Discussion: Global and detailed hydrogen Combustion Analysis	53
5.1	Introduction	53
5.2	Global reaction	53
5.2.1	Discussion of the global combustion key contours and flow structure	53
5.2.2	Visualisation of key contours and flow structure on global hydrogen combustion	55
5.3	Detailed Mechanism Reaction	76
5.3.1	Role of the CHEMKIN-Imported Mechanism:	76
5.3.2	Discussion of the Detailed hydrogen combustion key contours and flow structure	77
5.3.3	Visualisation of key contours and flow structure in detailed hydrogen mechanism combustion	79
5.4	Combustion Efficiency and Flammability Limits	100
5.4.1	Combustion Efficiency Trends	100
5.5	Static Temperature and Pressure Distribution at Mach 2. (Detailed Mechanism)	103
5.5.1	At Mach 2.0 (Detailed Mechanism)	103
5.5.2	Static Temperature and Pressure Distribution at Mach 2.75 (Detailed Mechanism)	104
5.5.3	Comment	104
5.5.4	Flammability Limit Analysis	105
5.6	Implications for Thrust Application and Engine Safety	106
5.6.1	Operational Envelope Awareness	107
5.6.2	Combustion Efficiency and Chamber Design	107
5.6.3	Implications for Thrust Control	107
5.6.4	Contributions to Engine Design and Control Systems	107
5.7	Conclusion	108
	Appendix	109
.1	Mathematical Developments	109
.2	NASA Hydrogen–Air Reaction Mechanism	109
.3	Thermodynamic Parameters	111
.4	Flowcharts or Procedures for Importing Detailed Mechanisms	111
.4.1	Flammability Limit Analysis	112
.4.2	Summary of Estimated Thrust Values	113

Nomenclature

σ	Viscous stress tensor ,
$\dot{\omega}_i$	Reaction rate of species i ,
\dot{m}_f	Mass flow rate of fuel
\dot{m}_{H_2}	Mass flow rate of unburned hydrogen,
\dot{Q}_c	Heat release rate from combustion,
η	Combustion efficiency,
γ	Heat capacity ratio (c_p/c_v)
κ	Von Kármán constant,
∇	Gradient or divergence operator,
\mathbf{f}	Body force per unit mass,
\mathbf{J}	Heat flux vector,
\mathbf{n}	Outward unit normal vector,
\mathbf{u}	Velocity vector,
μ	Dynamic viscosity,
μ_t	Turbulent viscosity,
Φ	Scalar dissipation rate,
ϕ	Mixture fraction or transported scalar,
ρ	Density,
τ_{ij}	Stress tensor components,
τ_{res}	Residence time,
ε	Turbulent dissipation rate,
A	Area,
C_1, C_2	Empirical model constants,

c_p	Specific heat at constant pressure,
c_v	Specific heat at constant volume,
D_i	Diffusion coefficient of species i ,
E	Total energy per unit mass,
e	Specific internal energy,
$f(\phi, t)$	PDF of scalar ϕ at time t ,
F_1	Blending function (e.g., in SST),
G_k	Production of turbulent kinetic energy,
H	Total enthalpy,
h	Specific enthalpy,
k	Turbulent kinetic energy,
p	Pressure,
Pr_t	Turbulent Prandtl number,
R	Universal gas constant,
S_i	Source term in transport equation,
T	Temperature,
u, v, w	Velocity components in x , y , and z directions,
U^+	Dimensionless velocity,
u_τ	Friction velocity,
V	Control volume ,
y	Wall distance,
y^+	Dimensionless wall coordinate,
Y_i	Mass fraction of species i ,
Y_{H_2}	Hydrogen mass fraction,

General Introduction

Combustion is a complex series of chemical reactions between a fuel and an oxidizer, characterized by heat release and transformation of species. In recent years, the study of supersonic combustion—combustion occurring at speeds exceeding the speed of sound—has gained critical importance in the advancement of high-speed propulsion systems. This phenomenon, which presents unique challenges distinct from subsonic combustion, is particularly relevant in the development of scramjet engines, promising significant improvements in the performance and efficiency of future aerial and space vehicles [1]

Supersonic combustion is distinguished by the intricate interaction between shock waves and flame dynamics, phenomena that markedly differ from those in traditional subsonic combustors. Understanding these complex flow and combustion behaviors is essential for optimizing combustor designs and improving propulsion efficiency [1]. Moreover, advanced thermodynamic modeling techniques and numerical simulation methods—such as the Equilibrium Viscosity Model (EVM), Large Eddy Simulation (LES), and Reynolds-Averaged Navier-Stokes (RANS) approaches—have been extensively utilized to analyze fuel-air mixtures under varying supersonic flow conditions [2].

Hydrogen fuel is emerging as a promising alternative due to its clean combustion properties, aligning with global efforts to reduce greenhouse gas emissions and achieve net-zero targets by 2050. Its high energy density and rapid reaction rates make it particularly suited for supersonic combustion applications, enabling more sustainable and efficient propulsion systems.

Despite significant progress, supersonic combustion research faces challenges, especially in developing simplified but accurate chemical reaction mechanisms that capture the complex behavior of high-temperature and high-pressure environments. Addressing these challenges is vital for advancing propulsion technologies that are not only more efficient but also environmentally sustainable.

This thesis focuses on the numerical simulation and analysis of supersonic combustion within a double parallel cavity geometry, exploring the effects of varying inlet Mach numbers on combustion performance. Using ANSYS Fluent with turbulence modeling based on the Reynolds-Averaged Navier-Stokes (RANS) equations and the $k-\epsilon$ turbulence model turbulence model, the study aims to provide insights into combustion dynamics and efficiency improvements for scramjet applications [3].

The thesis is organized as follows:

- **Chapter 1** provides an overview of supersonic combustion, including fundamental principles, chemical reaction mechanisms, and the physical challenges inherent in supersonic flows.
- **Chapter 2** presents the numerical methods and turbulence models employed in this study, including the formulation of the governing equations and the computational setup.

- **Chapter 3** details the combustor geometry design, boundary conditions, and mesh generation.
- **Chapter 4** discusses the simulation results, analyzing the influence of Mach number variations on combustion characteristics, shock-wave interactions, and flame stability.
- **Chapter 5** reviews the key findings, highlights the research contributions, and suggests directions for future work.

By systematically investigating these aspects, this work contributes to the understanding and optimization of supersonic combustion systems, supporting advancements in aerospace propulsion technology that prioritize both performance and sustainability.

Chapter 1

Overview of Supersonic Combustion

1.1 Scramjet

1.1.1 What is Supersonic Combustion

Supersonic combustion refers to the process of burning fuel in an airflow that remains supersonic—i.e., faster than the speed of sound—throughout the combustion process. This concept forms the foundation of scramjet (Supersonic Combustion Ramjet) propulsion systems, which are designed to operate efficiently at hypersonic flight speeds (typically Mach 5 and above).

Supersonic combustion differs fundamentally from subsonic combustion in several critical aspects:

- **Flow Characteristics:** In subsonic combustion, the airflow is slowed down (often to near-stagnation conditions) to allow efficient mixing and flame stabilization. In contrast, supersonic combustion allows the airflow to remain at supersonic speeds inside the combustor, which dramatically shortens the available residence time for fuel-air mixing and chemical reactions.
- **Thermodynamic Behavior:** Subsonic combustion can rely on pressure increases through flame propagation and thermal expansion, while in supersonic combustion, expansion occurs predominantly through shock waves and rapid gas acceleration. The pressure drop across the combustor is also more pronounced in supersonic regimes.
- **Flame Stabilization and Ignition:** Supersonic combustion faces significant challenges in flameholding due to the high-speed nature of the flow, requiring advanced methods such as cavity flameholders, pilot injections, or pulsed detonators. Subsonic combustors typically achieve stabilization using bluff bodies or recirculation zones.
- **Combustor Design:** Supersonic combustors are compact, with geometries optimized to manage shock waves, prevent total pressure losses, and support fast chemical reactions under high-speed flow conditions. Subsonic combustors can afford larger designs with more flexibility in fuel injection and mixing strategies.

These distinctions are critical when designing propulsion systems for high-speed aircraft, as they directly impact engine efficiency, fuel consumption, and structural requirements. Understanding these differences sets the foundation for exploring the challenges and mechanisms of combustion in the supersonic regime.

1.1.2 Why Supersonic Combustion

Scramjets are designed to operate efficiently at hypersonic speeds (mach 5 and above). Scramjets technology is not a new concept, The ramjets came around and took the world by a storm, the speeds were phenomenal, the SR71 black bird being an example and the ArcAngel 12 (unfortunately never flew and was replaced by the earlier mentioned SR7 black bird)

This project investigates the numerical simulation and analytical study of supersonic combustion in scramjet engines, using ANSYS at different Mach numbers and cavity configurations. Scramjets (Supersonic Combustion Ramjets) are a promising propulsion technology for high-speed aerospace applications, including reusable space launch systems and hypersonic vehicles. Their operation relies on compressing incoming high-speed air without rotating machinery, mixing it with fuel, and enabling combustion at supersonic speeds—all within milliseconds.

Figure 1.2 illustrates a typical scramjet engine layout, including the inlet, isolator, combustor, and nozzle. Efficient and stable combustion within this system is critical to overall performance, and it is strongly influenced by complex shock–flame interactions that differ drastically from those found in subsonic combustion.

Recent research underscores the importance of advanced thermodynamic and fluid dynamic modeling in analyzing supersonic combustion [1]. Techniques such as the Equilibrium Viscosity Model (EVM) [2], Reynolds-Averaged Navier-Stokes (RANS), and Large Eddy Simulations (LES) [3] provide critical insights into turbulent mixing, ignition delays, and flame stability in high-speed flows.

Hydrogen is increasingly favored as a fuel in scramjet systems due to its high reactivity and low carbon footprint. Its use aligns with global goals to reduce greenhouse gas emissions, contributing to the development of cleaner and more sustainable propulsion systems [3].

Furthermore, the development of accurate yet computationally tractable chemical reaction mechanisms remains an ongoing challenge. While detailed kinetic models are essential for capturing real combustion physics, simplified models are often required for practical simulation of high-temperature, high-pressure conditions in engineering-scale applications [4].

In summary, the investigation of supersonic combustion is a key step toward advancing high-speed propulsion technology, with broad implications for vehicle efficiency, emissions reduction, and aerospace innovation.

1.1.3 Prospective applications

The high costs associated with full-scale experiments involving flying scramjet engines have long hindered development. However, an increasing number of stakeholders are recognizing the potential, and currently, extensive research is being conducted on scramjet technology by various companies and organizations around the world. Since a scramjet is limited to a specific velocity range, it is often envisioned in combination with other propulsion systems, such as rockets and/or turbojet engines. Tested prototypes have initially been accelerated by a booster rocket. One of the most attention-grabbing potential applications of scramjet engines is their use in the proposed Single Stage to Orbit (SSTO) vehicle. An SSTO vehicle is designed to reach lower Earth orbit without jettisoning any parts of its structure, such as fuel tanks or burnt-out rockets. The term is almost exclusively applied to reusable vehicles. Many envision an SSTO vehicle that can take off and land horizontally like a conventional aircraft while being capable of carrying personnel and payloads to lower Earth orbits. The goal of SSTO technology is to provide cheaper, faster, and more secure access to space. This would be achieved by developing systems that, once operational, require less ground effort than current space transportation systems.

Various SSTO vehicle concepts have been proposed, several of which incorporate scramjet engines. Two of the more promising concepts are discussed here. The first is the Turbo Rocket Combined Cycle (TRCC), a propulsion concept that includes one or more conventional turbofan engines, a ramjet/scramjet engine, and multiple rocket engines. According to the conceptual design, the vehicle would take off horizontally and accelerate to Mach 2.5 using the turbofan engines. Once enough speed is achieved for ramjet propulsion, the combined ramjet/scramjet engine is activated. At Mach 2.5, the turbojets are shut off, and the vehicle is powered solely by the ramjet/scramjet engine. As the vehicle reaches Mach 5, the engine switches to full scramjet operation, continuing to accelerate up to Mach 14-18, at which point the rocket engines are ignited for the final thrust to put the vehicle into orbit.

Another variation, which may gain greater confidence, is the Rocket-Based Combined Cycle (RBCC). This system operates similarly to the TRCC, but without the turbojet engines. Instead, it utilizes rocket engines not only for the final acceleration to orbit but also for startup, until ramjet operation can take over. In both of these concepts, the vehicle would return to Earth and land like a conventional aircraft.

1.1.4 Challenges and technological advancements in Supersonic Combustion

This section discusses some of the key advantages and disadvantages of scramjet technology. One of the greatest benefits is its simple design. A scramjet typically has few or no moving parts, and its main structure consists of continuous surfaces. This results in relatively low manufacturing costs for the engine itself. A key distinction between hypersonic air-breathing engines and rocket engines is that scramjets do not require the transportation of an oxidizer for combustion. To illustrate this, consider NASA's Space Shuttle. At launch, the external tank of the shuttle holds approximately 616,432 kg of liquid oxygen and around 103,000 kg of liquid hydrogen, while the shuttle's total weight is around 104,000 kg. This means that roughly 75% of the shuttle's starting weight consists of liquid oxygen, whose sole purpose is to react with the fuel in the rocket engines' combustion chambers. If the need to carry this oxidizer could be eliminated, the vehicle would be lighter and potentially able to carry more payload, offering a significant advantage.

Flameholding and Mixing Techniques

One of the critical challenges in scramjet engines is achieving efficient flameholding and mixing in the combustor [5, 6]. Supersonic flows result in extremely short residence times for fuel and air, making it difficult to sustain combustion. To address this, researchers have explored various flameholding mechanisms, such as cavity-based flameholders and strut-based designs. Cavity-based scramjets utilize the recirculation of combustion gases to continuously ignite the fuel-air mixture, while strut-based designs use bluff bodies to create regions of low-speed flow for flame stabilization.

Advanced injection methods, such as oblique wall fuel injection, have been developed to enhance mixing and combustion efficiency [7]. These techniques create coherent vortices that improve the interaction between fuel and air streams, leading to better mixing and faster combustion rates.

Cooling Systems and Thermal Management

Hypersonic flight generates significant heat due to friction and combustion, necessitating advanced cooling systems [8, 9]. Regenerative cooling, where fuel is used as a coolant before combustion, is a common approach. This method not only protects the engine structure but also converts thermal energy into chemical energy, improving combustion performance.

Turbulence and Chemistry Interactions

Supersonic combustion involves complex interactions between turbulent flows and chemical reactions [10, 11]. The short residence times and high-speed flows make it challenging to model and predict combustion behavior accurately. Turbulence-chemistry interactions are particularly critical, as they influence the efficiency and stability of combustion.

Reaction Mechanism Models for Supersonic Combustion

In modeling supersonic combustion, selecting an appropriate chemical reaction mechanism is crucial for balancing computational efficiency with physical accuracy. The high-speed, short-residence-time environment in scramjet combustors requires models that can capture essential combustion behavior without becoming prohibitively expensive to simulate. Three primary types of chemical kinetic models are typically used: global, reduced, and detailed mechanisms.

Global reaction mechanisms simplify combustion chemistry into a single or few lumped reactions. For instance, hydrogen combustion may be represented by the global reaction:

This approach is computationally inexpensive and widely used in early design studies or large parametric sweeps. However, global mechanisms do not resolve intermediate species or reaction steps, making them unsuitable for predicting flame structure, ignition delay, or pollutant formation—particularly critical in supersonic flows with complex shock-flame interactions.

Detailed reaction mechanisms include all known elementary reactions and species relevant to a fuel's oxidation process. These are highly accurate and suitable for fundamental studies. For hydrogen, detailed mechanisms such as the one provided by the Lawrence Livermore National Laboratory (LLNL)[12] capture fine-scale kinetics and ignition phenomena. However, their complexity results in extremely high computational costs, making them impractical for most CFD simulations involving three-dimensional or even complex two-dimensional compressible turbulent flows.

Reduced reaction mechanisms strike a balance by retaining key species and reactions that govern flame propagation and ignition, while discarding less influential pathways. A common reduced hydrogen mechanism might include 7 species and around 10–15 reactions, sufficient to model supersonic combustion behavior with good fidelity and significantly reduced computational cost. These are widely adopted in CFD simulations of scramjet engines where reaction time scales must be resolved but computing resources are limited.

In this study, two distinct chemical kinetic approaches were employed. First, a **global mechanism**, available by default in Ansys Fluent, was utilized to maintain manageable computational load while allowing for broad assessment of combustion behavior under varying inlet Mach numbers. Second, a **detailed hydrogen mechanism from LLNL** was incorporated in later stages of the study to improve accuracy in capturing ignition and flame propagation characteristics in 2D geometries. This dual approach allowed us to evaluate the performance trade-offs between simplified and comprehensive chemical modeling strategies.

The aerothermodynamics of a scramjet combustor involves the analysis of high-speed air-flow and combustion processes within the engine. In a scramjet (supersonic combustion ramjet),

combustion occurs at supersonic speeds, which distinguishes it from traditional jet engines that operate in subsonic conditions. As shown by the figure below

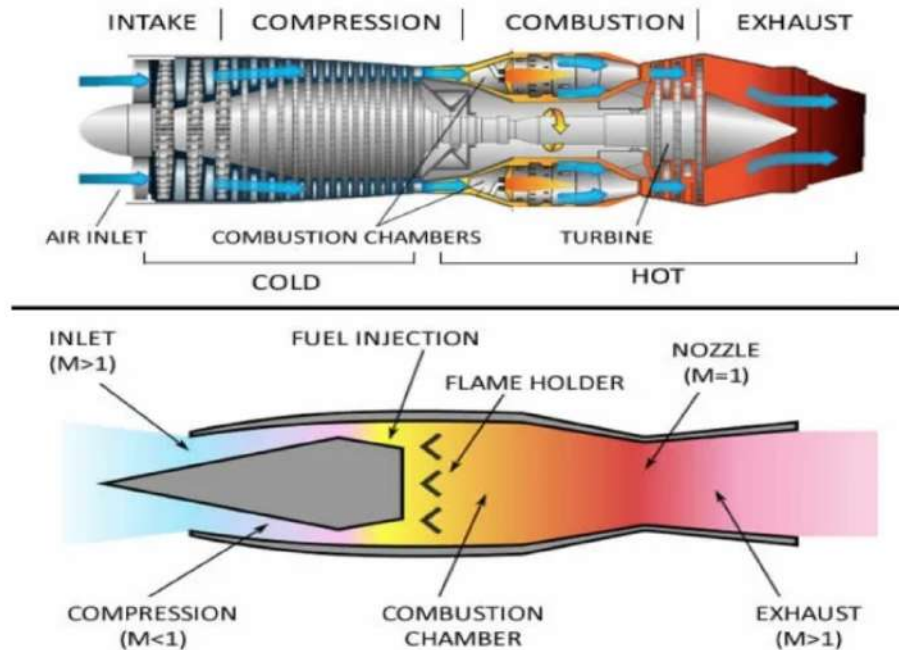


Figure 1.1: ramjet engine structure vs traditional jet engine structure[13]

The scramjet maintains a cooler flow inside the combustor walls therefore maintaining the integrity of the the wall structure. The normal and oblique shock waves are there to slow down the flow of the hypersonic object to supersonic inside at the inlet moving toward the combustion chamber, fuel is injected and ignited in the supersonic airflow.

The analysis typically employs one-dimensional and three-dimensional models to understand the flow dynamics, pressure, temperature, and Mach number at various engine stations.

The key components include the intake, which compresses incoming air. as shown here below.

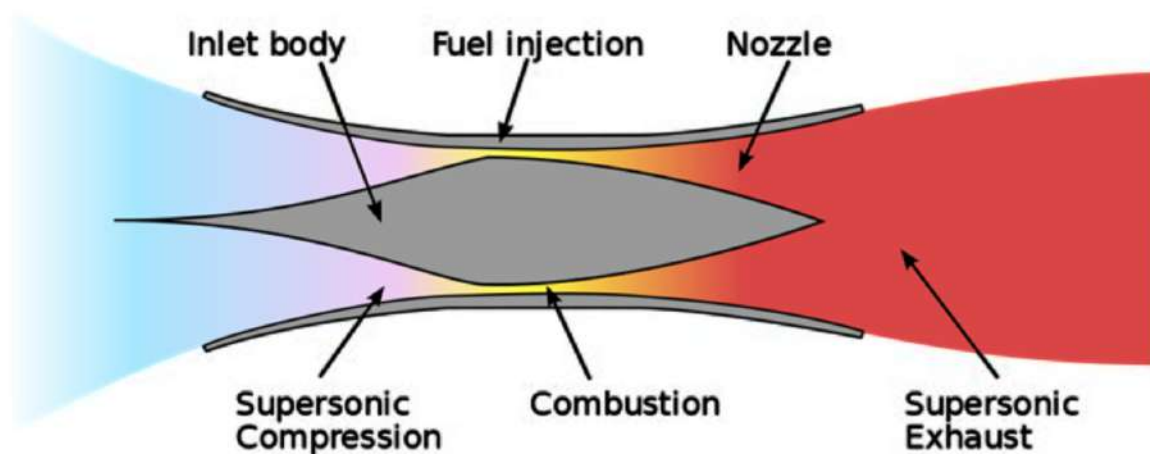


Figure 1.2: scramjet engine stations[13]

One-dimensional models focus on mass, momentum, and energy conservation equations to evaluate flow rates and thermal properties. Three-dimensional models provide a more detailed

view of the compressive flow dynamics, using computational fluid dynamics (CFD) to simulate the behavior of the airflow, including turbulence and shock wave interactions. In the scramjet combustor, the design aims to maintain efficient mixing of fuel and air while controlling shock waves that can form due to flow overexpansion. The combustor operates under conditions where the flow is intentionally overexpanded to generate shock waves, facilitating the mixing and combustion processes. The thermal management within the combustor is critical, as high static temperatures can arise, necessitating effective cooling strategies for engine components. [14]

The issue with hydrocarbon fuels is that they release of lower net thrust due to inefficient of the combustion. Since the scramjet are suitable say for vehicles moving at hypersonic speeds of say mach, the total enthalpy of incoming flow is comparable to that of combustion. One of the proposed methods that has been proven to be working theoretically is is the double combustion scramjet that burns the products of combustion i.e carbon dioxide, these react with metals hence obtaining extra thrust. [15]

Overall, the aerothermodynamics of a scramjet combustor is a complex interplay of fluid dynamics, thermodynamics, and combustion science, aimed at optimizing performance across various flight regimes, from subsonic to hypersonic speeds.[14]

1.1.5 History of Ramjet and Scramjet Development

The origins of air-breathing supersonic propulsion can be traced back to the early 20th century. Around 1900, René Lorin conceived the idea of the ramjet engine—a propulsion system that relies on high-speed forward motion to compress incoming air, thereby eliminating the need for rotating compressor components. Ramjets operate efficiently at supersonic speeds by slowing the incoming air to subsonic velocities within the combustion chamber, where fuel is mixed and burned to produce thrust.

Scramjets (Supersonic Combustion Ramjets), while based on the same principle of ram compression, differ significantly in operation. In scramjet engines, the airflow remains supersonic throughout the combustion chamber. This key distinction allows scramjets to operate comfortably at speeds above Mach 5, whereas ramjets are typically limited to the range of Mach 3 to 6. The elimination of moving parts in both designs makes them mechanically simpler than traditional jet engines.

Initial investigations into scramjet technology focused on understanding shock-induced combustion and the inherent challenges of flameholding at high Mach numbers (2–6). These efforts laid the groundwork for modern hypersonic propulsion research. The 1960s and 1970s saw increased interest in ramjet technology. However, in recent years, the resurgence of research has been driven more by the promise of efficiency and practicality in scramjets rather than mere speed.

Scramjets generate thrust by utilizing pressure differences and shock waves formed by incoming high-speed air, without the need to decelerate the airflow to subsonic speeds. At Mach numbers exceeding 6, there is insufficient residence time to slow down the airflow before combustion, making supersonic combustion essential. In scramjet operation, mixing and combustion of fuel occur downstream of the diffuser in a rapid and efficient manner. Hence, understanding the behavior of high-speed flows—especially under varying thermodynamic conditions—is crucial for advancing hypersonic flight technologies.

Significant early contributions to the field include Smith et al. [16], who investigated shock-induced combustion in supersonic flows. While their work provided valuable insights into flame stabilization, it lacked comprehensive turbulence modeling, which is now considered essential

for accurate prediction of combustion behavior.

In the 2000s, advancements in Computational Fluid Dynamics (CFD) significantly improved the modeling of supersonic combustion. From 2015 onwards, the introduction of Large Eddy Simulation (LES) techniques has provided more accurate insight into mixing and flameholding in scramjet combustors.

Supersonic combustion remains a cornerstone technology for hypersonic flight. Traditional ramjets face performance limitations at high Mach numbers due to increased drag and thermal loads. Scramjets overcome these limitations by sustaining combustion in a supersonic flow, resulting in better thrust efficiency and enabling sustained flight at hypersonic speeds.

1.2 State of the Art

Over the past few decades, scramjet technology has advanced significantly, culminating in successful flight tests that have demonstrated full supersonic combustion under real-world conditions.

One of the earliest milestones was the CIAM/NASA Mach 6.5 Scramjet Flight Program, a Russian-American collaboration conducted in the late 1990s. This program achieved one of the first verified scramjet combustor flight tests, laying the groundwork for subsequent international efforts [17].

Shortly thereafter, the University of Queensland initiated the HyShot project, conducting a series of scramjet flight experiments in Australia [18]. These tests were essential for validating supersonic combustion outside the United States and for expanding global hypersonic research capabilities.

A key turning point occurred in 2004 with NASA's Hyper-X program and the X-43A vehicle. The X-43A reached a record-breaking speed of Mach 9.6, becoming the fastest air-breathing aircraft ever flown. It was launched atop a modified Pegasus rocket from a B-52 at 13,000 meters, then accelerated to 29,000 meters where the scramjet engine was ignited. The engine operated successfully for ten seconds before the vehicle glided to a controlled impact in the Pacific Ocean [19]. Figure 1.3 shows the X-43A scramjet vehicle during pre-launch preparations.

As scramjet development transitions from testing to practical implementation, several critical challenges remain. These include turbulence-chemistry interactions, efficient fuel-air mixing, flameholding stability, and thermal management. To overcome these issues, researchers are increasingly integrating high-fidelity numerical simulations with experimental data.

1.2.1 Plasma-Assisted Combustion

Plasma-based actuators are gaining traction as tools to promote mixing, ignition, and flame stability in supersonic flows. These actuators help overcome ignition delays and flame blowout under extreme flight conditions [21].

1.2.2 Endothermic Fuels and Reduced Chemical Mechanisms

Next-generation fuels like endothermic hydrocarbons are being explored to both enhance thrust and manage heat. During decomposition, these fuels absorb heat, helping to cool engine walls while releasing energy-rich radicals [8, 9]. Parallel to this, simplified chemical models are being used to reduce simulation costs while preserving fidelity [11].



Figure 1.3: Fig. 1.1: NASA X-43A scramjet research vehicle setup before flight [20]

1.2.3 Reduced-Order Models and Surrogate Fuels

Reduced-order modeling and surrogate fuels enable the simulation of complex combustion processes with manageable computational resources. They aim to retain key physics while being deployable in large-scale engine simulations [9].

1.2.4 Summary of Key Studies

In summary, the evolution of scramjet technology has been driven by a combination of experimental flight tests, advanced fuels, and computational modeling. Landmark efforts such as the X-43A and HyShot have validated the feasibility of sustained supersonic combustion. Plasma-assisted techniques and endothermic fuels have shown promise in addressing ignition and thermal constraints. Meanwhile, reduced-order models and simplified chemistry are enabling faster simulations with reasonable accuracy. Despite this progress, key challenges remain—especially in achieving stable, efficient combustion across diverse flight conditions.

1.3 Project Presentation

1.3.1 Geometry Description and Configuration

The present study focuses on a double cavity-based scramjet combustor, selected due to its demonstrated ability to promote flameholding and enhance fuel-air mixing in supersonic flows. This geometry consists of two rectangular cavities embedded into the bottom wall of a constant-area duct, followed by a short expansion and straight section.

Table 1.1: Summary of Selected Key Studies in Scramjet Research

Study	Author(s)	Methodology	Findings	Limitations
CIAM/NASA Mach 6.5	Roudakov et al. (1996)	Flight Test	Demonstrated early in-flight supersonic combustion	Limited run duration
HyShot Project	Smart, Bowersox, Stalker (2006)	Flight Experiments	Validated non-U.S. supersonic combustion	Low combustion duration
X-43A Hyper-X	McClinton et al. (NASA, 2004)	Rocket-launched Flight Test	Achieved Mach 9.6, validated scramjet ignition	Only 10-second burn
Plasma-Assisted Combustion	Leonov & Frolov (2018)	Experimental Actuators	Enhanced ignition and flameholding	Requires complex power systems
Endothermic Fuels	Gong & Wang (2013)	Thermochemical Modeling	Enabled thrust and heat management	Requires advanced fuel logistics
Reduced Chemistry Models	Huang & Liu (2022)	Numerical Reduction	Lower computational cost in simulations	Accuracy vs. complexity trade-off

1.3.2 Boundary Conditions

The CFD model applies the following boundary conditions:

- **Inlet:** Supersonic flow at specified Mach numbers (2.0 to 3.0), with prescribed total pressure and total temperature. For reacting cases, hydrogen is injected as a premixed fuel at a fixed mass fraction.
- **Outlet:** Supersonic pressure outlet (zero-gradient), allowing the flow to exit freely.
- **Walls:** No-slip, adiabatic wall condition to represent insulated channel surfaces.
- **Symmetry Plane:** Used for half-domain simulations to reduce computational cost while preserving physical fidelity.

1.3.3 Rationale for Geometry Choice

The double cavity combustor is chosen for its favorable aerodynamic properties in flame stabilization. The first cavity helps initiate recirculation and enhance mixing, while the second sustains ignition and prevents flame blowout. Compared to single-cavity designs, the double cavity layout provides better robustness under varying Mach numbers and equivalence ratios.

This configuration has also been validated in several prior experimental and numerical studies, making it a suitable candidate for both cold and reacting flow simulations in scramjet applications.

Aim of the Thesis

The aim of this thesis is to investigate the aerodynamic and combustion behavior of a supersonic scramjet combustor using high-fidelity CFD simulations. The study is divided into two main stages: cold flow analysis and reacting flow simulations.

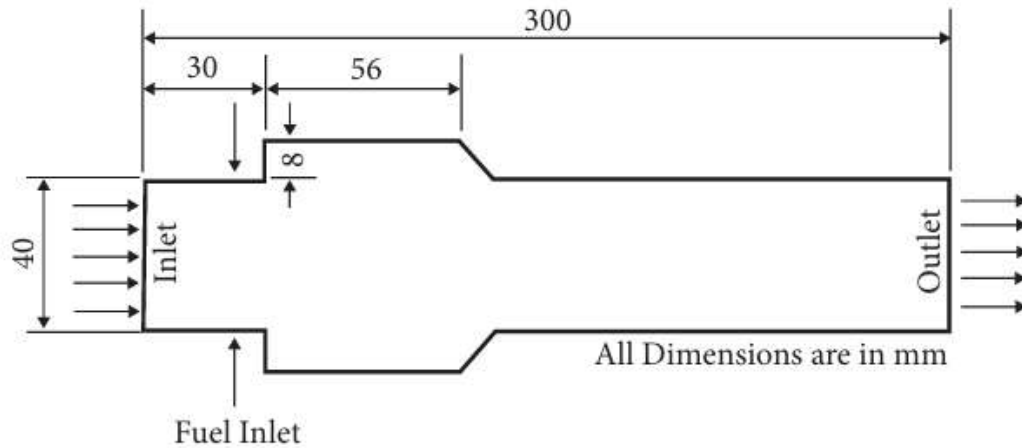


Figure 1.4: Annotated schematic of the double cavity scramjet combustor geometry[22]

The first stage focuses on non-reacting (cold flow) simulations at two inlet Mach numbers (2.0 and 2.75), assessing the development of shock waves, recirculation zones, and shear layers. These simulations establish a baseline for understanding the flow structure before ignition.

The second stage involves reacting flow simulations using both global and detailed chemical mechanisms. Supersonic hydrogen-air combustion is studied across a range of equivalence ratios ($\phi = 0.6, 1.0, 2.3$, and) to evaluate combustion efficiency, flameholding behavior, and ignition limits under lean, stoichiometric, and rich conditions.

A double cavity combustor geometry is chosen for its ability to enhance flameholding through strong shear layers and vortex generation. This configuration is widely used in experimental and numerical studies due to its relevance to practical scramjet applications.

Ultimately, the thesis aims to provide detailed insight into the coupling between flow dynamics and combustion chemistry in high-speed propulsion systems and to identify optimal operating regimes for efficient and stable scramjet performance.

1.4 Conclusion

Understanding supersonic combustion is critical for the development of advanced aerospace propulsion systems. This chapter established the foundational knowledge necessary to approach the challenges and innovations surrounding scramjet technology.

While supersonic combustion continues to face stability issues, rapid advancements in research and engineering are gradually overcoming these obstacles. The chapter aimed to clarify the scope of this study, highlight recent breakthroughs, and outline the major challenges—particularly those related to flameholding, ignition, and fuel-air mixing.

Ongoing research focuses on unraveling the complex, three-dimensional, unsteady behavior of primary jets and plasma discharge (PD) plumes in reactive environments. In particular, studies aim to better understand the physical mechanisms that enhance combustion efficiency and stability [3, 23].

Chapter 2

Mathematical Modelling

This chapter provides a concise description of the theoretical foundations behind computational fluid dynamics (CFD) and combustion modeling. It presents the governing equations and the numerical methods used to solve them.

2.1 Introduction

This chapter outlines the mathematical models used to simulate supersonic combustion. It includes the fundamental equations of fluid dynamics, turbulence modeling, and combustion modeling, as well as the numerical solver employed for computation.

A summary of the main equations and modeling approaches is provided, along with justification for the selected solver. Their importance in accurately capturing the physical phenomena of supersonic combustion is also emphasized.

2.2 Mathematical Modelling of Reacting Flows

The combustion of gaseous fuels occurs when a fuel and an oxidant—typically air—are brought into contact, mixed at the molecular level, and heated to the ignition temperature. Upon reaching this threshold, chemically bound energy is released, and combustion products are formed. This release of energy results in a rise in temperature and the expansion of combustion gases, which in turn influence the surrounding flow field.

Combustion processes are generally categorized into two main types: **pre-mixed combustion**, in which the fuel and oxidizer are thoroughly mixed prior to ignition, and **diffusion combustion**, where the two components are introduced separately and must mix before combustion can proceed.

Accurate mathematical modeling of combustion—particularly in the context of aerospace applications—necessitates the consideration of multiple interacting phenomena, including fluid dynamic behavior, gas-phase chemical reactions, and detailed chemical kinetics.

The theoretical basis of fluid mechanics has been established for over a century, with the fundamental governing equations derived from Newton’s second law of motion. These are collectively known as the **Navier–Stokes equations**, named after Claude-Louis Navier and George Gabriel Stokes. Due to their nonlinear nature, these equations do not generally admit closed-form analytical solutions, except in a limited number of simplified cases.

As a result, the formulation of fluid-mechanical models typically involves systems of partial differential equations that require the application of **numerical methods** for their resolution.

Numerical approaches involve discretizing both space and time into finite computational grids and time steps, enabling the iterative approximation of solutions across the defined computational domain.

In most practical scenarios, fluid flow is predominantly **turbulent**, characterized by its highly irregular and seemingly random nature. In such flows, the velocity at a specific point in space cannot be deterministically predicted at a given time. The onset and behavior of turbulence are governed by the **Reynolds number**, a dimensionless parameter representing the ratio of inertial to viscous forces within the fluid.

At high Reynolds numbers, a significant scale separation emerges between the large-scale structures—where energy is introduced into the flow—and the smallest scales, known as **Kolmogorov scales**, where viscous dissipation of energy occurs. To resolve turbulent flows “exactly” through numerical simulations, the computational mesh must be sufficiently fine to capture the smallest turbulent eddies, and the solution must be advanced in time to capture the unsteady nature of the flow.

However, this requirement imposes a severe demand on computational resources. The number of computational cells and the time-step resolution are directly constrained by the available computing capacity. Consequently, **Direct Numerical Simulation (DNS)** is currently feasible only for low Reynolds number flows in simple geometries.

For flows of practical interest—typically involving high Reynolds numbers and complex geometries, as encountered in engineering and scientific applications—some form of model simplification is necessary. The most widely adopted approach is the use of **Reynolds-Averaged Navier–Stokes (RANS)** models, which statistically average the effects of turbulence. These models are founded on the assumption that the flow is either statistically steady or varies slowly over time, allowing the turbulent fluctuations to be treated through additional closure models.

Turbulence models, like those described above, thus provide a way of making very complex equation systems more manageable. Another method of technological interest is **Large Eddy Simulation (LES)**. In LES, the large energy-containing eddies are directly simulated, while only the small-scale turbulence is modeled. This method has, on several occasions, proven to be more accurate in resolving various observed phenomena.

However, the computational cost of LES remains very high, primarily due to its requirement for a very fine computational mesh. Despite its expense, the method is rapidly becoming feasible with the advent of massive computer clusters.

In order to simulate combustion, the Navier–Stokes equations must be complemented with a **chemical reaction mechanism** and a **thermodynamic model**. The chemical reaction mechanism defines how the fuel and oxidant react, what products are formed, and in what proportions. The thermodynamic model describes, among other things, how much energy is released or dissipated.

A typical flame, such as in a gas turbine, is between 0.01 and 0.1 mm thick, while the smallest (Kolmogorov) eddies are on the order of 0.05 mm. Large eddies wrinkle the flame and might tear holes in it, while small eddies align along the flame without significantly affecting it. Because of limited computing capacity, a typical computational mesh in a combustion simulation has a cell size on the order of 1 mm. Thus, the combustion process occurs at a sub-grid level, i.e., it cannot be resolved but must be modeled.

Models for the chemical combustion process exist in varying degrees of complexity and accuracy. The most complex models use many different reaction steps and species to describe the reaction mechanism, while simpler models treat the combustion as an instantaneous transition from reactants to products.

Turbulence affects combustion by wrinkling the flame, thereby increasing its surface area,

which in turn enhances mixing and accelerates the reaction. In that sense, turbulence is advantageous, although it should not be too strong, as the reactants would then not have enough time to mix on a molecular level and the flame could extinguish [24].

2.3 Computational Fluid Dynamics

CFD is a computational tool for analyzing and simulating fluid mechanical processes, such as mass, heat, and momentum transfer. The numerical method most commonly used is the finite volume method (FVM). This method is implemented in both software tools utilized in this thesis work.

2.3.1 Governing Equations

The compressible, turbulent, chemically reacting flow investigated in this study is governed by the Navier–Stokes equations, which express the conservation of mass, momentum, energy, and chemical species. These equations are formulated in conservative form to ensure proper handling of shock waves and discontinuities typical in supersonic combustion. The main governing equations are summarized in governing equations Table 2.1.

Table 2.1: Conservation equations for compressible, reactive flow [25]

Law	Equation (Conservative Form)
Mass (Continuity)	$\frac{\partial \rho}{\partial t} + \nabla \cdot (\rho \mathbf{u}) = 0$
Momentum	$\frac{\partial(\rho \mathbf{u})}{\partial t} + \nabla \cdot (\rho \mathbf{u} \otimes \mathbf{u}) = -\nabla p + \nabla \cdot \boldsymbol{\tau} + \rho \mathbf{f}$
Energy	$\frac{\partial(\rho E)}{\partial t} + \nabla \cdot [(\rho E + p)\mathbf{u}] = \nabla \cdot (k \nabla T) + \Phi + \dot{Q}_c$
Species	$\frac{\partial(\rho Y_m)}{\partial t} + \nabla \cdot (\rho Y_m \mathbf{u}) = -\nabla \cdot \mathbf{J}_m + \dot{\omega}_m$

Here, ρ is the fluid density, \mathbf{u} is the velocity vector, p is the pressure, E is the total energy per unit mass, T is the temperature, and Y_m is the mass fraction of species m . The tensor $\boldsymbol{\tau}$ represents the viscous stress, k is the thermal conductivity, Φ is the viscous dissipation term, \dot{Q}_c is the chemical heat release, and $\dot{\omega}_m$ is the species production or consumption rate. The diffusive flux of species m is denoted by \mathbf{J}_m , and \mathbf{f} accounts for body forces such as gravity.

The system is closed using the equation of state for a calorically perfect gas:

$$p = \rho R T, \quad E = i + \frac{|\mathbf{u}|^2}{2}, \quad i = C_v T$$

where R is the specific gas constant and C_v is the specific heat at constant volume.

2.3.2 Finite Volume Method

The finite volume method (FVM) is used in this work to solve the governing equations of mass, momentum, energy, and species transport. This method is widely employed in computational fluid dynamics (CFD) due to its ability to conserve fluxes across control volumes, making it especially suitable for compressible and reactive flows such as those encountered in scramjets.

In FVM, the computational domain is divided into discrete control volumes. The integral form of the governing equations is applied over each volume, ensuring local and global conservation. Numerical fluxes across cell faces are approximated using schemes such as upwind differencing, which provides stability but may introduce numerical diffusion.

This approach is implemented through ANSYS Fluent, which uses a cell-centered FVM framework to discretize and solve the transport equations over a structured or unstructured mesh.

2.4 Turbulence Modelling

Turbulence refers to fluctuations in the flow field across both space and time. It is a highly complex and not yet fully understood phenomenon, primarily due to its three-dimensional, unsteady nature and its manifestation across a wide range of length and time scales. Turbulence arises when inertial forces in the fluid become dominant relative to viscous forces, typically characterized by a high Reynolds number.

As discussed in Section of Mathematical Modeling of reacting flows, a direct numerical simulation (DNS) of turbulent flow in a scramjet engine would demand an extremely fine computational grid, far beyond current computational capabilities. Therefore, a modeling approach is required to approximate the effects of turbulence.

The most common method for modeling turbulence, and the approach adopted in this thesis, is the Reynolds-Averaged Navier-Stokes (RANS) model. RANS formulations use a statistical treatment of turbulence by decomposing instantaneous flow variables into mean and fluctuating components. This leads to the time-averaged RANS equations, which include Reynolds stress terms to represent turbulent effects [26].

2.4.1 Turbulence Modelling with the Standard k - ε Model

The standard k - ε model is one of the most widely used turbulence models in engineering applications, particularly for high Reynolds number and wall-bounded flows. It belongs to the class of two-equation models, where two additional partial differential equations are solved to account for turbulence effects.

The model solves transport equations for:

- the turbulent kinetic energy k , which represents the energy contained in turbulent eddies, and
- the dissipation rate ε , which quantifies the rate at which this energy is dissipated into heat by viscosity.

The transport equations are as follows:

Turbulent Kinetic Energy Equation

$$\rho \frac{\partial k}{\partial t} + \rho \vec{u} \cdot \nabla k = \nabla \cdot \left[\left(\mu + \frac{\mu_t}{\sigma_k} \right) \nabla k \right] + P_k - \rho \varepsilon \quad (2.1)$$

Dissipation Rate Equation

$$\rho \frac{\partial \varepsilon}{\partial t} + \rho \vec{u} \cdot \nabla \varepsilon = \nabla \cdot \left[\left(\mu + \frac{\mu_t}{\sigma_\varepsilon} \right) \nabla \varepsilon \right] + C_{\varepsilon 1} \frac{\varepsilon}{k} P_k - C_{\varepsilon 2} \rho \frac{\varepsilon^2}{k} \quad (2.2)$$

Turbulent (Eddy) Viscosity The turbulent viscosity is modeled as:

$$\mu_t = \rho C_\mu \frac{k^2}{\varepsilon} \quad (2.3)$$

Turbulent Kinetic Energy Production Term

$$P_k = \mu_t (\nabla \vec{u} + \nabla \vec{u}^T) : \nabla \vec{u} \quad (2.4)$$

The constants used in the standard k - ε model are:

$$C_\mu = 0.09, \quad \sigma_k = 1.0, \quad \sigma_\varepsilon = 1.3, \quad C_{\varepsilon 1} = 1.44, \quad C_{\varepsilon 2} = 1.92$$

Variable Definitions:

- ρ : Fluid density
- \vec{u} : Mean velocity vector
- μ : Dynamic viscosity
- μ_t : Turbulent (eddy) viscosity
- $\sigma_k, \sigma_\varepsilon$: Turbulent Prandtl numbers for k and ε
- P_k : Production of turbulent kinetic energy

Model Characteristics and Suitability: The standard k - ε model is known for its:

- Good performance in fully developed turbulent flows, boundary layers, and moderate separation.
- Low computational cost and robust convergence behavior.
- Limitations in predicting strong streamline curvature, large flow separation, and anisotropic turbulence.

It was selected in this work due to its balance of accuracy and efficiency for supersonic and compressible flows where wall-bounded turbulence and shock interactions are dominant, particularly in cavity-based scramjet geometries.

2.4.2 Near-Wall Modelling and the Log-Law of the Wall

Accurately capturing near-wall behavior is critical in turbulence modeling. The standard wall function approach uses the logarithmic law of the wall:

$$U^+ = \frac{1}{\kappa} \ln(y^+) + C, \quad (2.5)$$

where $U^+ = \frac{U_t}{u_\tau}$, $y^+ = \frac{\rho u_\tau y}{\mu}$, and $u_\tau = \sqrt{\frac{\tau_w}{\rho}}$ is the friction velocity. Constants κ and C depend on the surface roughness and are empirically determined.

This approach simplifies the near-wall treatment while preserving reasonable accuracy in boundary layer regions.

2.4.3 Sources of Error and Uncertainty in CFD

CFD simulations are subject to several potential sources of uncertainty and error. These include:

Model Uncertainty: Arises from the simplifications and assumptions made in physical modeling (e.g., turbulence, combustion, multiphase flows). Once a model is selected, the solution accuracy is inherently limited by the model's capability.

Numerical Errors: These are the differences between the exact mathematical solution of the governing equations and their numerical approximations. Using higher-order discretization schemes can reduce these errors significantly.

Application Uncertainty: Inaccuracies in boundary conditions, initial conditions, or geometry details introduce significant variability in the solution.

Software Errors: These are bugs or issues in the CFD code itself, which may arise from incorrect implementations or limitations in the graphical user interface.

User Errors: Mistakes made during problem setup, such as poor mesh quality, inappropriate boundary conditions, or oversimplified physics, can lead to incorrect results.

Understanding and managing these sources of error is critical to ensure the reliability and accuracy of CFD simulations.

2.4.4 Practical Application in Scramjet Combustor

In the context of a scramjet combustor, the Boussinesq approximation can be useful for modeling localized regions where buoyancy effects are significant due to temperature gradients, but where density variations remain moderate. This is particularly relevant near solid boundaries or flame-holding devices, where heat release and wall heating can generate buoyancy-driven flows without large changes in fluid compressibility.

Although scramjet flows are generally characterized by high-speed, compressible behavior that requires solving the full Navier–Stokes equations with a compressible equation of state, the Boussinesq model can still offer simplifications in specific regions. It allows buoyancy effects to be included without requiring the full coupling of pressure and temperature in the density field.

Additionally, the Boussinesq approximation aids turbulence modeling by linking Reynolds stresses to mean velocity gradients, providing a simplified yet effective means to approximate turbulence-induced mixing in non-isothermal flows.

2.5 Combustion Modelling

Similar to turbulence, combustion processes occur on extremely small spatial and temporal scales, which makes direct numerical simulation infeasible with current computational resources. Therefore, combustion must also be modeled rather than directly simulated.

Chemical reactions do not occur instantaneously; rather, they proceed through a sequence of elementary reaction steps. A *reaction mechanism* represents this sequence, detailing which chemical bonds are broken and formed, the order of these transformations, and the rate at which each reaction occurs. Detailed mechanisms may include hundreds of individual reaction steps, offering high fidelity at the expense of significant computational cost.

To reduce computational demand, simplified or global mechanisms are often employed. These consist of only one or two reactions that effectively represent the overall combustion process. While computationally efficient, these models sacrifice accuracy for speed.

2.5.1 Finite-Rate Chemistry

The *finite-rate chemistry* model accounts for the finite speed at which chemical reactions proceed. In this framework, each elementary reaction n is treated as potentially reversible, provided that a backward reaction is explicitly defined.

The net rate of progress $\dot{\omega}_n$ of the reaction n is given by:

$$\dot{\omega}_n = k_{fn} \prod_m [I_m]^{a_{mn}} - k_{bn} \prod_m [I_m]^{b_{mn}}, \quad (2.6)$$

where:

- $[I_m]$ is the molar concentration of species m ,
- a_{mn} and b_{mn} are the reaction orders for the forward and backward reactions, respectively (determined experimentally),
- k_{fn} and k_{bn} are the forward and backward reaction rate coefficients.

These reaction rate coefficients are typically expressed in Arrhenius form:

$$k = AT^B e^{-E/(RT)}, \quad (2.7)$$

where:

- A is the pre-exponential factor,
- B is the temperature exponent,
- E is the activation energy,
- R is the universal gas constant,
- T is the absolute temperature.

The finite-rate chemistry model is especially important for simulations where chemical kinetics play a dominant role, such as ignition, extinction, and pollutant formation in combustion systems.

Use of this model is particularly suitable when reaction rates are limited by turbulent mixing in some regions of the computational domain and by chemical kinetics in others. This dual limitation is common in practical combustion systems, especially those involving complex geometries or varying flow regimes.

In the simulations performed using ANSYS CFX, the combined finite-rate chemistry/eddy dissipation model was employed. To reduce computational complexity, a simplified single-step reaction mechanism was used. While this approach introduces some approximation, it provides a balance between computational efficiency and the ability to capture essential combustion behavior across different flow regions.

2.5.2 Reaction Mechanism

In combustion modeling, the choice of a reaction mechanism directly affects the balance between computational efficiency and chemical fidelity. For general engineering use, global or simplified mechanisms are often adequate. However, in high-speed reactive flows such as those encountered in scramjets, detailed chemical kinetics are necessary to capture ignition behavior, intermediate species, and heat release rates accurately.

For the hydrogen–air combustion simulations carried out in ANSYS CFX, a detailed reaction mechanism developed by NASA was selected. This mechanism includes 33 elementary reactions and 13 species and is widely adopted in aerospace applications for modeling hydrogen–air combustion at high temperatures and pressures.

The kinetic parameters for each reaction are based on the Arrhenius law:

$$k_f = AT^B \exp\left(-\frac{E}{RT}\right), \quad (2.8)$$

where A is the pre-exponential factor, B is the temperature exponent, and E is the activation energy. These coefficients are species- and reaction-specific and allow calculation of forward reaction rates at each time step.

The complete list of elementary reactions and corresponding kinetic parameters is provided in Appendix .2 for reference.

2.5.3 Probability Density Function (PDF) Model

The Probability Density Function (PDF) approach is a statistical method used in turbulent combustion modeling to account for the stochastic nature of turbulent mixing and chemical reactions. Instead of solving transport equations for the mean values of scalars (such as temperature, species mass fractions, or mixture fraction), the PDF model solves a transport equation for the joint probability density function of these scalars.

This method is particularly effective in simulating turbulent diffusion flames, where strong nonlinear coupling exists between turbulence and chemical reactions—conditions that are common in supersonic combustion.

The general form of the joint scalar PDF transport equation is:

$$\frac{\partial f(\phi, \vec{x}, t)}{\partial t} + \vec{u} \cdot \nabla f = -\nabla_\phi \cdot (\langle \vec{\omega} | \phi \rangle f) + D_\phi + S_f, \quad (2.9)$$

where:

- $f(\phi, \vec{x}, t)$ is the joint PDF of the scalar vector ϕ (e.g., temperature, species mass fractions),
- $\langle \dot{\omega} | \phi \rangle$ is the conditional mean of the chemical source term,
- D_ϕ represents molecular and turbulent diffusion in scalar space,
- S_f is a source term due to scalar mixing or turbulence.

The advantage of the PDF approach lies in its ability to exactly represent the chemical source term without requiring closure assumptions for mean reaction rates, which is a major limitation in conventional models. In this work, the PDF model is particularly suitable due to the highly turbulent and compressible nature of the scramjet combustor environment, where flame structures are strongly affected by turbulent mixing and scalar fluctuations.[27]

2.5.4 Finite-Rate/Eddy Dissipation Model

In the current study, the combustion process is modeled using the finite-rate/eddy dissipation approach, which accounts for both chemical kinetics and turbulent mixing limitations.

This hybrid model evaluates two reaction rates:

- The **finite-rate (Arrhenius)** rate, based on detailed chemical kinetics.
- The **eddy dissipation rate**, based on turbulent mixing time scales.

The net reaction rate $\dot{\omega}_i$ for species i is determined as the *minimum* of the two:

$$\dot{\omega}_i = \min(\dot{\omega}_{\text{Arrhenius}}, \dot{\omega}_{\text{eddy}}), \quad (2.10)$$

where: - $\dot{\omega}_{\text{Arrhenius}}$ is the rate from the chemical kinetic mechanism (typically multi-step, temperature-dependent), - $\dot{\omega}_{\text{eddy}} = C \frac{\rho \varepsilon}{k} Y_i$, where C is a model constant, ε is the turbulence dissipation rate, k the turbulent kinetic energy, and Y_i the mass fraction of the limiting reactant.

This formulation ensures that: - When chemical kinetics are fast (high Damköhler number), turbulence controls the reaction rate. - When turbulence is weak or reaction rates are slow, chemical kinetics dominate.

This model is well-suited for high-speed combustion where both mixing and kinetics influence flame behavior.[28]

2.5.5 ARCHIMEDES Model

The ARCHIMEDES (Advanced Reduced Chemistry in Microstructure-Dependent Eddy Structures) model is a flamelet-based model that assumes a steady-state solution for combustion chemistry over small-scale flamelets embedded in turbulent eddies. It uses precomputed flamelet libraries and integrates them with turbulence information.

Although ARCHIMEDES is less commonly implemented in standard CFD tools, it is valuable for efficient combustion simulation in highly turbulent reacting flows, such as gas turbines. It combines flamelet concepts with advanced turbulence-resolving models like LES or RANS.

Selecting an appropriate turbulence model is crucial for accurate predictions in fluid dynamics. Common turbulence models include the k-epsilon model, k-omega SST model, and Large

Eddy Simulation (LES) . Each model has its advantages and limitations, depending on the specific flow characteristics and computational resources available. For instance, the k-epsilon model is often favored for its simplicity, while LES provides more detailed insights into turbulent structures. Additionally, Probability Density Function (PDF) methods and combustion models such as ARCHIMEN and EDC are employed to capture the complexities of turbulent combustion processes, allowing for a more comprehensive understanding of interactions between turbulence and chemical reaction.

2.6 Reference pressure

In CFX, it is essential to define a Reference Pressure for the simulation, which is set in the Basic Settings tab of the Domains form. This reference value applies across all domains in the simulation, ensuring consistency. Whenever a new domain is created or an existing domain is modified, the Reference Pressure is updated throughout the simulation.

All pressure values within the simulation are relative to this Reference Pressure. This reference avoids round-off errors in the situation of flows for which dynamic pressure changes are small compared to the absolute pressure. For instance, dynamic pressure changes in low-speed atmospheric flows may be only a few Pascals, but compared to atmospheric pressure (100,000 Pa), such tiny changes would be lost due to round-off errors. To avoid this, a reasonable Reference Pressure should be defined, e.g., the ambient atmospheric pressure of 100,000 Pa, so that small changes in pressure are made more noticeable (e.g., a change of 1 Pa would now affect the first significant figure).

That being said, one can use a Reference Pressure of 0 Pa without issues when the dynamic pressure changes are large compared to the absolute pressure, e.g., for certain liquid flow simulations where the pressure level is irrelevant. Where boundary or initial conditions are provided, they always relate to this Reference Pressure. For example, to apply a boundary pressure of 100,000 Pa, you would specify the boundary relative pressure as 0 Pa if the reference pressure is 100,000 Pa, or 100,000 Pa if the reference pressure is 0 Pa. Reference Pressure can also be defined using a CEL expression, but time-varying Reference Pressure values are not permitted.

This is crucial for correct modeling in scramjet combustion simulations where the pressure fluctuations can drive combustion dynamics. Correct reference pressure avoids computational inconsistencies, especially where small changes in pressure are accounted for in high-speed flows.[29]

2.7 Solver Description

The CFD simulations were carried out using **ANSYS Fluent 24.0**. The solver setup is summarized in Table 2.2, listing key numerical models and assumptions applied throughout the study.

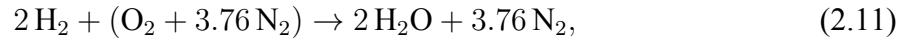
This configuration is suitable for simulating high-speed, chemically reacting flows with shock structures and compressibility effects typical of scramjet combustors.

Table 2.2: Summary of simulation setup in ANSYS Fluent

Feature	Choice / Setting
Solver Type	Density-based, steady-state
Flow Type	Compressible, 2D
Turbulence Model	Standard $k-\varepsilon$ (RANS)
Combustion Model	Finite-rate / Eddy Dissipation
Species Transport	Enabled (multi-species reactions)
Chemistry Model	Arrhenius kinetics
Gas Model	Ideal gas
Energy Equation	Enabled
Discretization Schemes	Second-order upwind (for convective terms)

2.8 Stoichiometric Fuel-to-Air Ratio and Equivalence Ratio Calculation

Hydrogen combustion in air proceeds according to the balanced reaction:



where nitrogen is included to represent atmospheric air composition.

Using molar masses of hydrogen, oxygen, and nitrogen, the stoichiometric fuel-to-air mass ratio was determined to be approximately 0.0294. This value serves as a reference for defining the equivalence ratio ϕ , which quantifies the richness or leanness of the fuel-air mixture:

$$\phi = \frac{(F/A)_{\text{actual}}}{0.0294}. \quad (2.12)$$

The equivalence ratio provides insight into whether the mixture is stoichiometric ($\phi = 1$), lean ($\phi < 1$), or rich ($\phi > 1$). In the simulations, the hydrogen inlet pressure is varied to adjust richness, while air conditions remain constant. The resulting mass flow rates from Fluent allow calculation of actual fuel-to-air ratios, enabling detailed analysis of combustion dynamics under varying mixture compositions.

The following sections present the temperature fields, reaction progress, and flow characteristics across different Mach numbers and equivalence ratios, highlighting trends and performance implications for supersonic combustion propulsion systems.

2.8.1 Link Between Static Pressure and Equivalence Ratio

The equivalence ratio (ϕ) is a key parameter in combustion analysis, defined as the ratio of the actual fuel-to-air ratio to the stoichiometric fuel-to-air ratio:

$$\phi = \frac{(F/A)_{\text{actual}}}{(F/A)_{\text{stoich}}} = \frac{\dot{m}_{\text{fuel}}/\dot{m}_{\text{air}}}{(F/A)_{\text{stoich}}} \quad (2.13)$$

where \dot{m}_{fuel} and \dot{m}_{air} are the mass flow rates of fuel and air, respectively.

In this study, the fuel mass flow rate \dot{m}_{fuel} is directly related to the static pressure at the hydrogen fuel inlet, P_{fuel} . Using the ideal gas law and fluid dynamic relations, the mass flow rate of hydrogen can be approximated by:

$$\dot{m}_{\text{fuel}} = \rho_{\text{fuel}} A_{\text{fuel}} V_{\text{fuel}} = \frac{P_{\text{fuel}}}{R_{\text{fuel}} T_{\text{fuel}}} A_{\text{fuel}} V_{\text{fuel}}$$

where ρ_{fuel} is the hydrogen density, A_{fuel} is the inlet cross-sectional area, V_{fuel} is the inlet velocity, R_{fuel} is the specific gas constant for hydrogen, and T_{fuel} is the static temperature at the fuel inlet.

Assuming that the air mass flow rate \dot{m}_{air} , temperature, and velocity remain constant, the equivalence ratio ϕ can be expressed as a linear function of the hydrogen inlet static pressure:

$$\phi = \frac{1}{(F/A)_{\text{stoich}}} \times \frac{P_{\text{fuel}}}{R_{\text{fuel}} T_{\text{fuel}}} \times A_{\text{fuel}} \times \frac{V_{\text{fuel}}}{\dot{m}_{\text{air}}} \quad (2.14)$$

This demonstrates that controlling the static pressure at the fuel inlet is critical for setting and maintaining the desired equivalence ratio in the combustion chamber, which directly affects flame characteristics and combustion performance.

2.9 Conclusion

In conclusion, the mathematical modeling of fluid dynamics through the Navier-Stokes equations, RANS equations, and turbulence models is vital for understanding and predicting fluid behavior in various applications. The choice of turbulence model significantly impacts the accuracy of simulations, particularly in complex flows involving transitions to turbulence and combustion. We will also see at the end the different values of equivalence ratios that correspond to the values of the minimum and the maximum and the minimum flammability.

Continued advancements in computational techniques and modeling approaches will enhance our ability to analyze and design fluid systems effectively, paving the way for innovations in engineering and technology[29]

Chapter 3

Numerical Modelling and ANSYS Procedure

Introduction

This chapter presents a comprehensive overview of the **numerical modeling process** and the complete **simulation procedure implemented in ANSYS Fluent**. It outlines the modeling strategy used to investigate supersonic combustion within cavity-based scramjet combustors. The chapter begins with a detailed description of the geometric configurations of the combustion chambers, followed by the methodology employed for mesh generation and refinement.

Subsequent sections describe the setup of physical boundary conditions, the selection of appropriate turbulence and combustion models, and the configuration of the **density-based solver** for compressible flow simulations. Both non-reacting (cold flow) and reacting (combustion) cases are simulated to understand the mixing behavior, flameholding characteristics, and combustion efficiency under varying inlet Mach numbers.

To enhance clarity and reproducibility, relevant ANSYS Fluent interface windows, including setup panels, solver configuration, and result visualization tools, are captured and included throughout the chapter. These visual-aids not only support the explanation of procedures but also serve as a reference for future users seeking to replicate similar simulations.

Overall, this chapter establishes the computational framework that underpins the analysis and validation presented in subsequent sections.

3.1 Scope and Software Tools

The work presented in this thesis has been structured as follows. First, a three-dimensional model of a scramjet combustor was developed.

The physical domain was then discretized into a computational mesh suitable for numerical simulation. Subsequently, computational fluid dynamics (CFD) and combustion simulations were performed using ANSYS CFX.

The simulation results were compared with available experimental data to assess accuracy and physical fidelity. The following software tools were used throughout the project:

- **ANSYS DesignModeler** — for CAD modeling and geometry preparation.
- **ANSYS CFX 24.0** — for performing steady and transient CFD and combustion simulations.

- **ANSYS CFX-Post, Tecplot 10.0, and MATLAB 7.0** — for visualization, data extraction, and post-processing of the simulation results.

3.2 Modeling the Flow in ANSYS CFX

The general workflow for solving a fluid dynamics problem in ANSYS CFX follows a structured and modular procedure. This approach ensures clarity, consistency, and effective handling of both geometry and physics. The main steps are:

1. **Geometry Definition:** The physical domain of the problem is created using a CAD tool such as ANSYS DesignModeler, where all relevant dimensions, boundaries, and internal features are specified.
2. **Mesh Generation:** The computational domain is discretized into a finite volume mesh. This mesh consists of a large number of cells (control volumes) over which the governing equations are numerically solved. Mesh quality is critical for accuracy and convergence.
3. **Setup in CFX-Pre:** In ANSYS CFX-Pre, the physical models are defined. This includes assigning material properties, selecting turbulence and combustion models, specifying boundary and initial conditions, and configuring solver settings.
4. **Solution with CFX Solver:** The configured case is passed to the ANSYS CFX Solver, where the governing equations (continuity, momentum, energy, species transport, etc.) are solved iteratively until convergence is reached.
5. **Post-Processing:** The results of the simulation are analyzed using ANSYS CFX-Post. This includes visualization of flow fields, temperature distributions, species concentrations, and other relevant quantities. Further data processing may be performed in Tecplot or MATLAB.

3.3 Geometry

3.3.1 Formulation of the Geometry

The fuel-air mixing efficiency within a scramjet combustor is highly dependent on the development of shear layers. This has been mentioned and introduced at the end of chapter one refer to figure 1.4 geometry-schematic. To enhance this process, the use of cavity flame holders has been recognized as an effective strategy for generating shear-driven mixing zones. In this study, the computational model incorporates **parallel cavities**, intentionally designed to promote shear layer formation and improve combustion performance.

The geometry was constructed and simulated using **ANSYS Fluent 24.0**, with dimensions adopted from experimental research conducted by **Yang et al.** at the **National University of Defence, China**. In the experimental setup, a **Mach 2.0 nozzle** connects the isolator section to the combustor. The combustor itself features parallel cavities spaced **40 mm apart**, with each cavity having a depth of **8 mm** and an **aft wall angled at 45°**. Hydrogen fuel is injected at **sonic velocity** through injectors with a **2 mm diameter**.

A **two-dimensional model** was chosen to minimize computational cost and maintain low uncertainty. The computational domain measures **300 mm in length and 40 mm in width**.

Given the symmetry of the geometry, only the upper half was modeled. and to observe fully in another case the whole geometry was modelled

- **Geometry:**
 - **Case :** Parallel cavity-based combustor (based on a Chinese experimental configuration)^{1.4}
- **Grid Type:** Structured or unstructured; high-quality mesh refinement applied near cavity regions and fuel injection zones
- **Grid Size:** Adequate resolution ensured; y^+ maintained below 30 for turbulence model compatibility, especially near walls
- **Mesh Sensitivity Study:** A mesh sensitivity analysis was conducted to assess the impact of grid refinement on simulation accuracy. Results showed good agreement across different grid resolutions, confirming mesh independence at higher refinement levels.

3.4 Different combustion chamber geometries used in the study of scramjet .

Due to time constraints, in this work, we decided to focus on the double cavity combustor, however the **2D schematic of a scramjet combustor with an integrated strut injector** inside a **linearly diverging duct** has been used by several other researchers in the field.

3.5 Mesh and mesh Sensibility studies

3.5.1 High-quality computational meshes for each combustor geometry

A comprehensive mesh refinement analysis was performed to ensure mesh independence of the key output parameters. The mesh was refined across four grid levels (G4 to G0) with element sizes ranging from 8.0 mm down to 0.1 mm, and total mesh elements increasing from 600 to nearly 1.8 million (Table for mesh grid independancy 3.1

Table 3.1: Mesh independence analysis based on outlet velocity.

Grid Level	Element Size [mm]	Total Cells	Outlet Velocity [m/s]
G5 (Coarse++)	12.0	350	950.00
G4 (Coarse)	8.0	600	1,000.00
G3	4.0	1,211	1,063.55
G2	1.0	18,154	1,098.64
G0 (Fine)	0.1	1,232,860	1,110.08
G-1 (Ultra-Fine)	0.05	~4,200,000	1,114.76

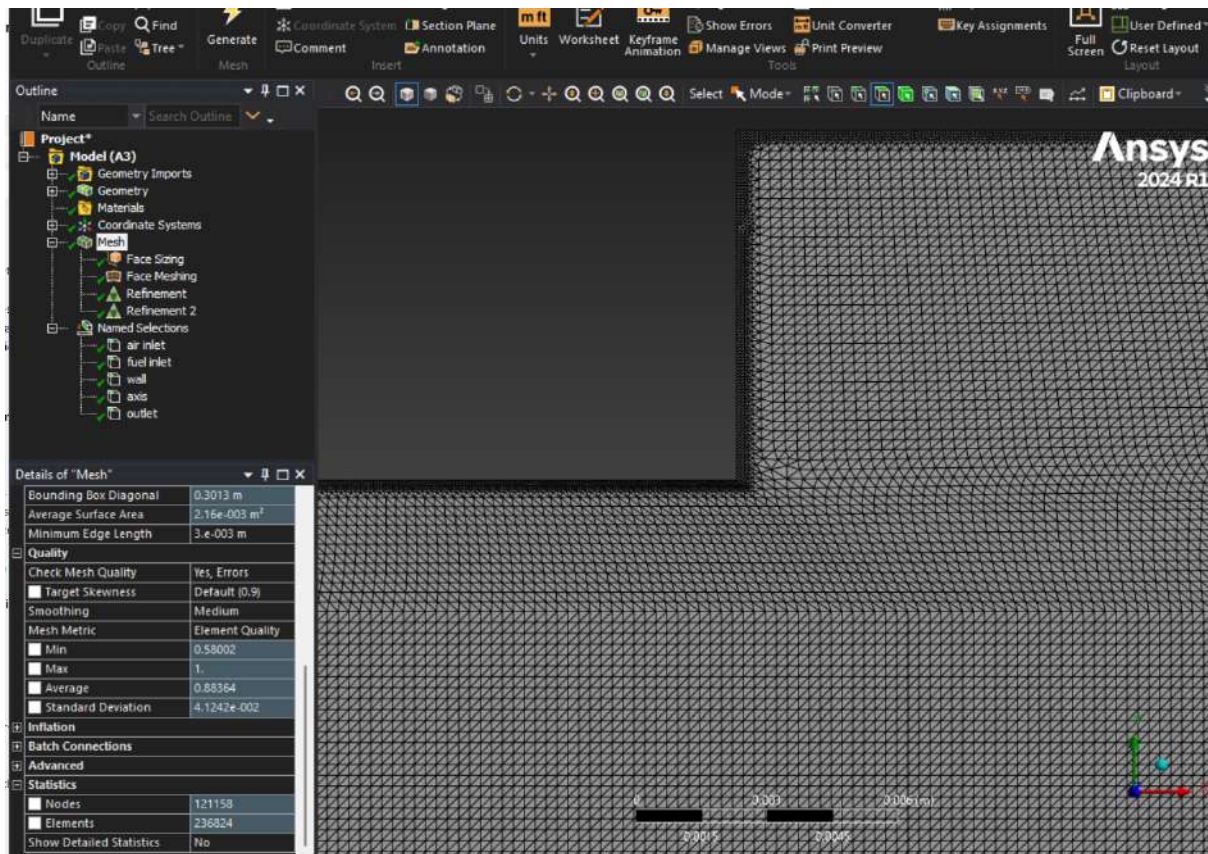


Figure 3.1: double cavity combustor mesh, refined at the edges with 5 layer refinement, number of elements used is 1232860

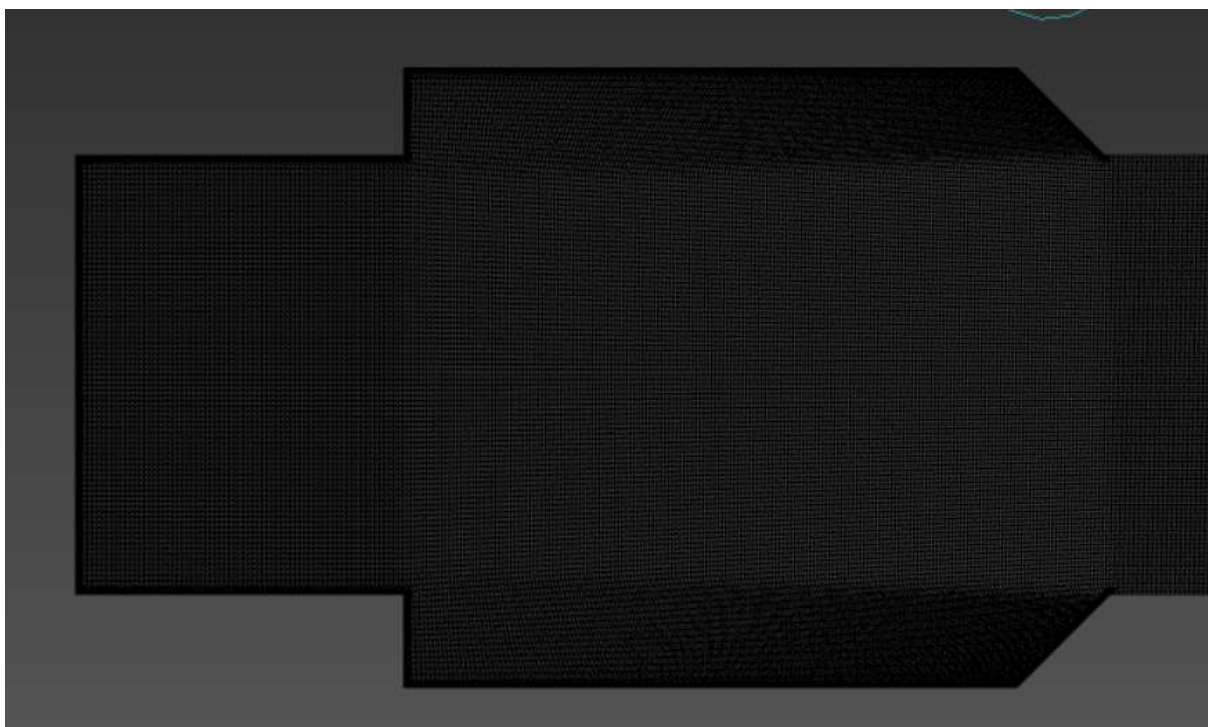


Figure 3.2: mesh high resolution zones, number of elements used is 1232860 elements

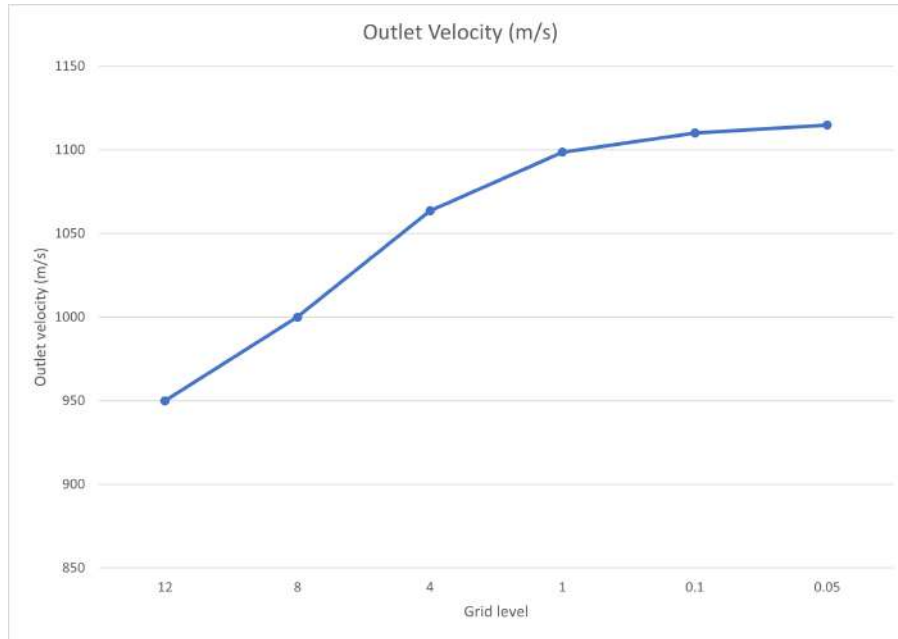


Figure 3.3: Mesh independence analysis: outlet velocity stabilizes as the mesh is refined, confirming solution convergence. The graph is based on results for grid levels G5 to G-1.

As seen in Table 3.1, the outlet velocity stabilizes between grid G2 and G0, suggesting mesh independence is achieved at grid G0. Therefore, G0 was selected for all subsequent simulations.

3.6 Evaluation of mesh quality metrics

3.6.1 Skewness

Skewness determines how close to ideal (i.e. equilateral or equiangular) a face cell is [34].

The following table lists the range of skewness values and the corresponding cell quality.

Value of Skewness	Cell Quality
1	degenerate
0.9 – <1	bad (sliver)
0.75 – 0.9	poor
0.5 – 0.75	fair
0.25 – 0.5	good
>0 – 0.25	excellent
0	equilateral

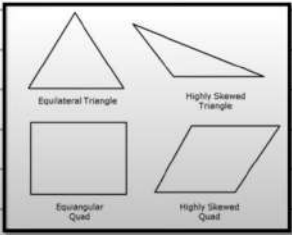


Figure 3.4: skewness table

The mesh exhibits a high-quality distribution with an average skewness of 0.0375 and a maximum of 0.66935, well within the acceptable threshold for CFD simulations. These values suggest the mesh is both numerically stable and suitable for resolving critical flow features, particularly in regions involving shock-boundary layer interactions and fuel-air mixing.

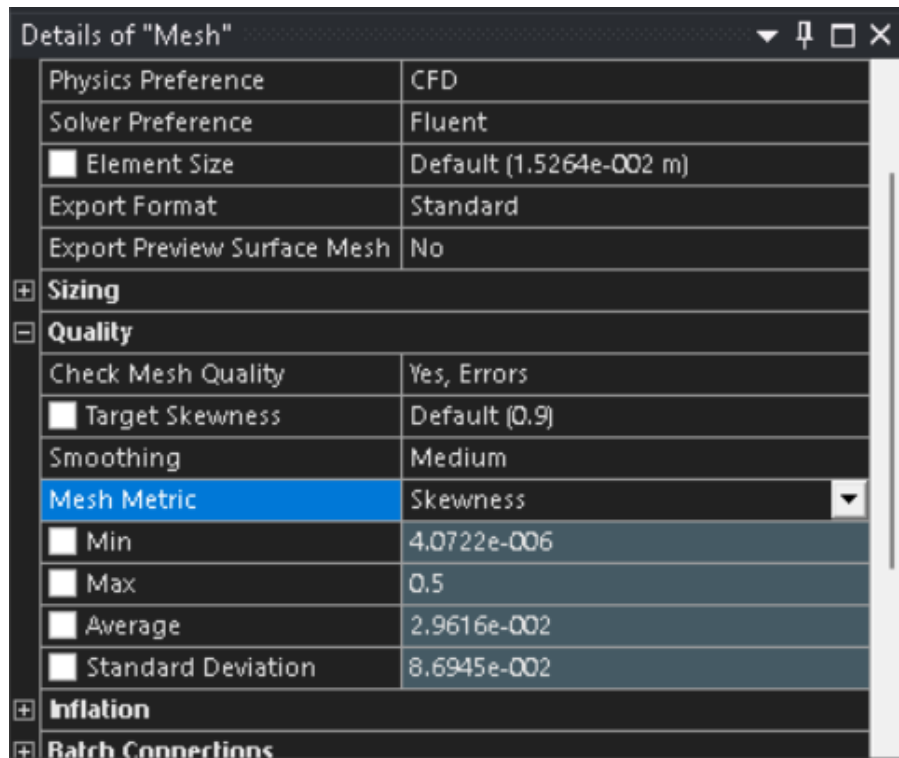


Figure 3.5: skewness of the current study, mesh number of elements of 232860 elements

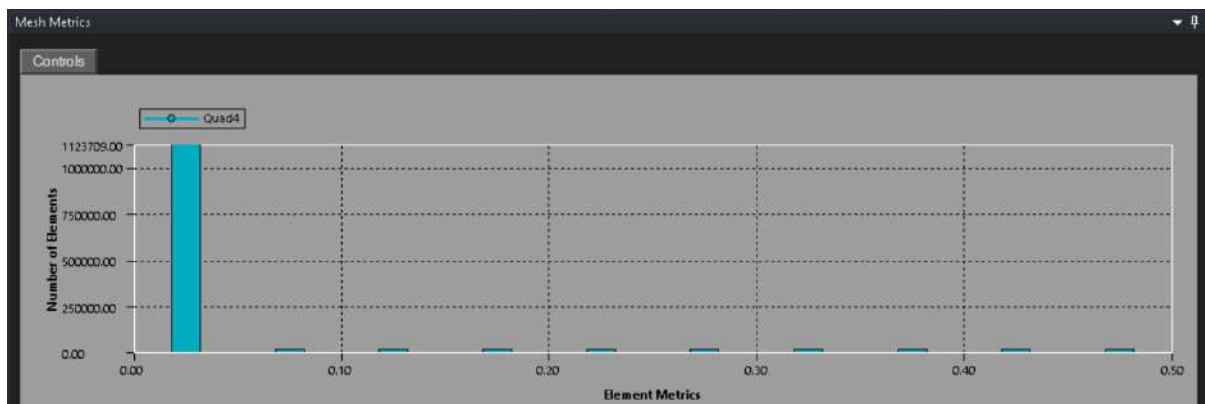


Figure 3.6: skewness graphical presentation, mesh study of the current and used case for proceeding studies , number of elements of 1232860 elements

3.6.2 Orthogonal quality

Orthogonal quality assesses how well element faces align with the vector normal to the element volume. It ranges between

Orthogonal quality analysis of the mesh reveals that the majority of elements exhibit values greater than 0.95, indicative of highly orthogonal cells. This ensures low numerical diffusion and strong alignment with flow vectors, particularly important in resolving shock structures and boundary layers in compressible flow simulations. The absence of low-quality elements (< 0.5) confirms that the mesh is well-suited for high-fidelity CFD analysis.

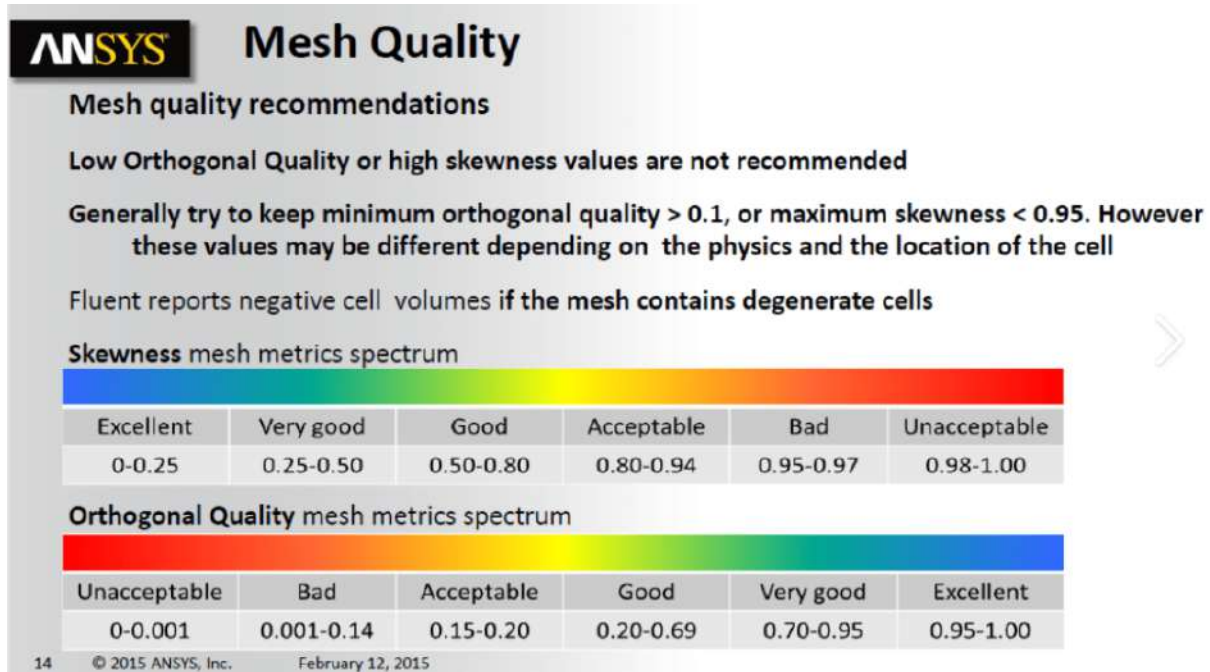


Figure 3.7: orthogonal quality scale

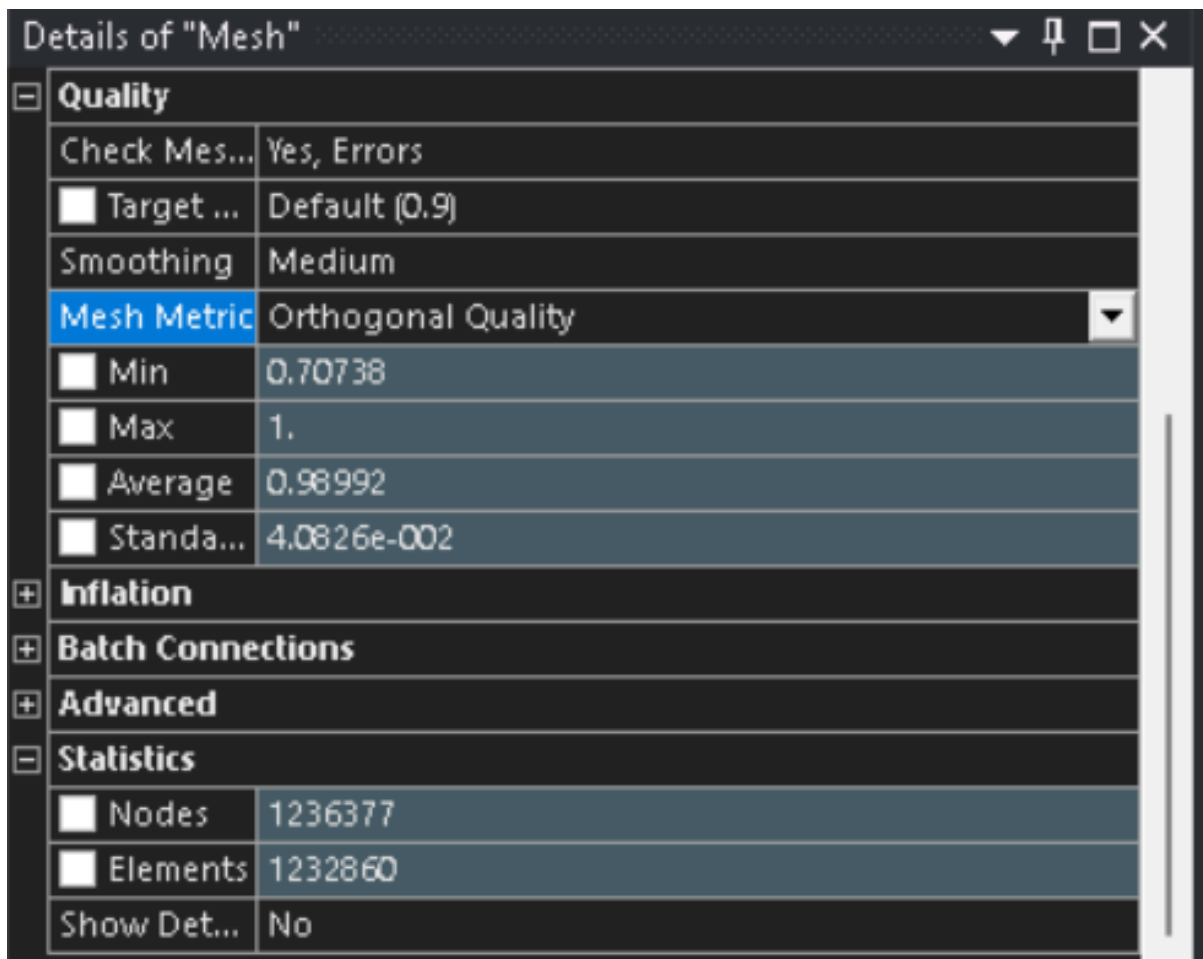


Figure 3.8: mesh Orthogonal qualityfor the double cavity combustor

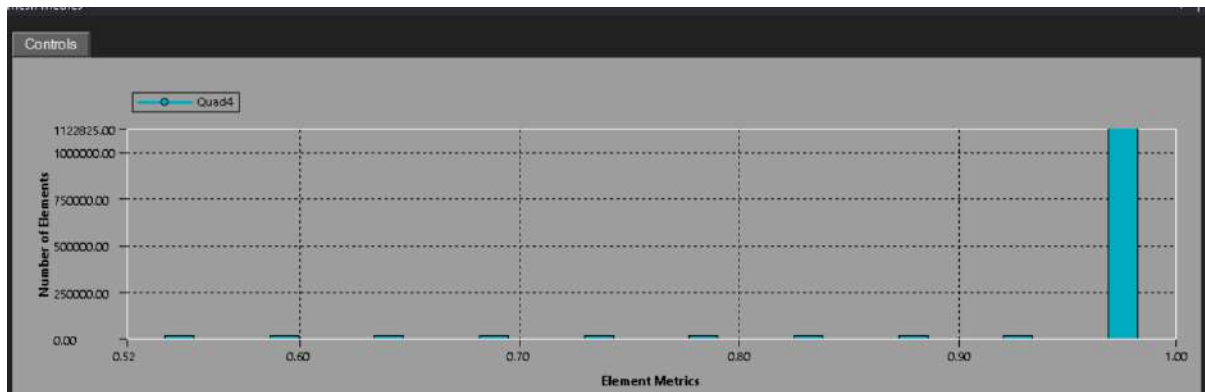


Figure 3.9: The orthogonal quality of about 0.99 overly,excellent as shown by the scale above.

3.7 2D simulation Boundary Conditions

Case: Minimum Inflow Mach Number ($M = 2.0$ as an example)

Simulation Environment:

- **Software:** ANSYS Fluent 24
- **Turbulence Model:** Standard $k-\epsilon$ (k-epsilon)
- **Combustion Model:** Finite-rate / Eddy Dissipation
- **Solver:** Density-based, steady-state
- **Equation Set:** Reynolds Averaged Navier-Stokes (RANS)
- **Chemical Species:** Hydrogen-air combustion

Air Inlet:

- **Mach Number:** 2.0
- **Static Pressure:** 95,000 Pa
- **Temperature:** 900 K
- **Species Composition:** Air ($O_2 + N_2$ and water)

Fuel Injection:

- **Fuel Type:** Hydrogen (H_2)
- **Injection Location:** From bottom and top wall slot into cavity
- **Total Pressure:** 630 KPa
- **Temperature:** 300k

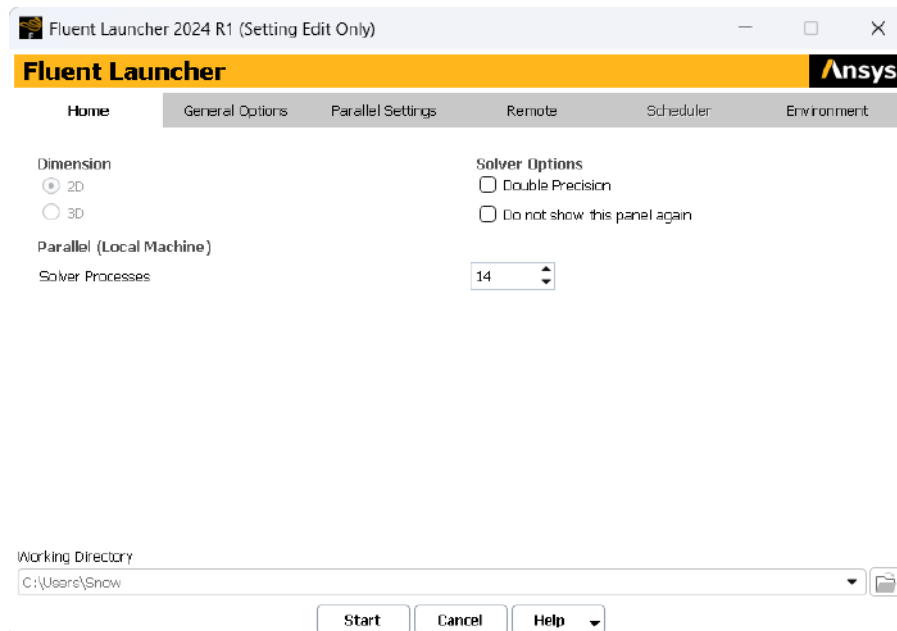


Figure 3.10: Launch fluent

Outlet:

- **Pressure Outlet**
- **Static Pressure:** Atmospheric or slightly sub-atmospheric using $1 \text{ atm} = 101325 \text{ Pa}$

3.8 Fluent Setup

3.8.1 Launch Fluent

In this setup, we use 14 processes because we have 16 processes in the computer to leave two processes for background. Then I enabled my graphics card Nvidia A1000 to speed up the computation.

3.8.2 General

General ?

Mesh

Scale... Check Report Quality

Display... Units...

Solver

Type

☐ Pressure-Based

☒ Density-Based

Velocity Formulation

☒ Absolute

☐ Relative

Time

☒ Steady

☐ Transient

2D Space

☒ Planar

☐ Axisymmetric

☐ Axisymmetric Swirl

☐ Gravity

Figure 3.11: General settings, density based solver, planar 2D space and stationary with respect to time.

Here, this is where I select steady state for the stationary computation to reduce the computational cost. Then I use the Density-based solver. This solver is the best for compressible supersonic flows, particularly with shock wave interactions within the combustor.

3.8.3 Model ,turbulence,Energy Activation in Fluent

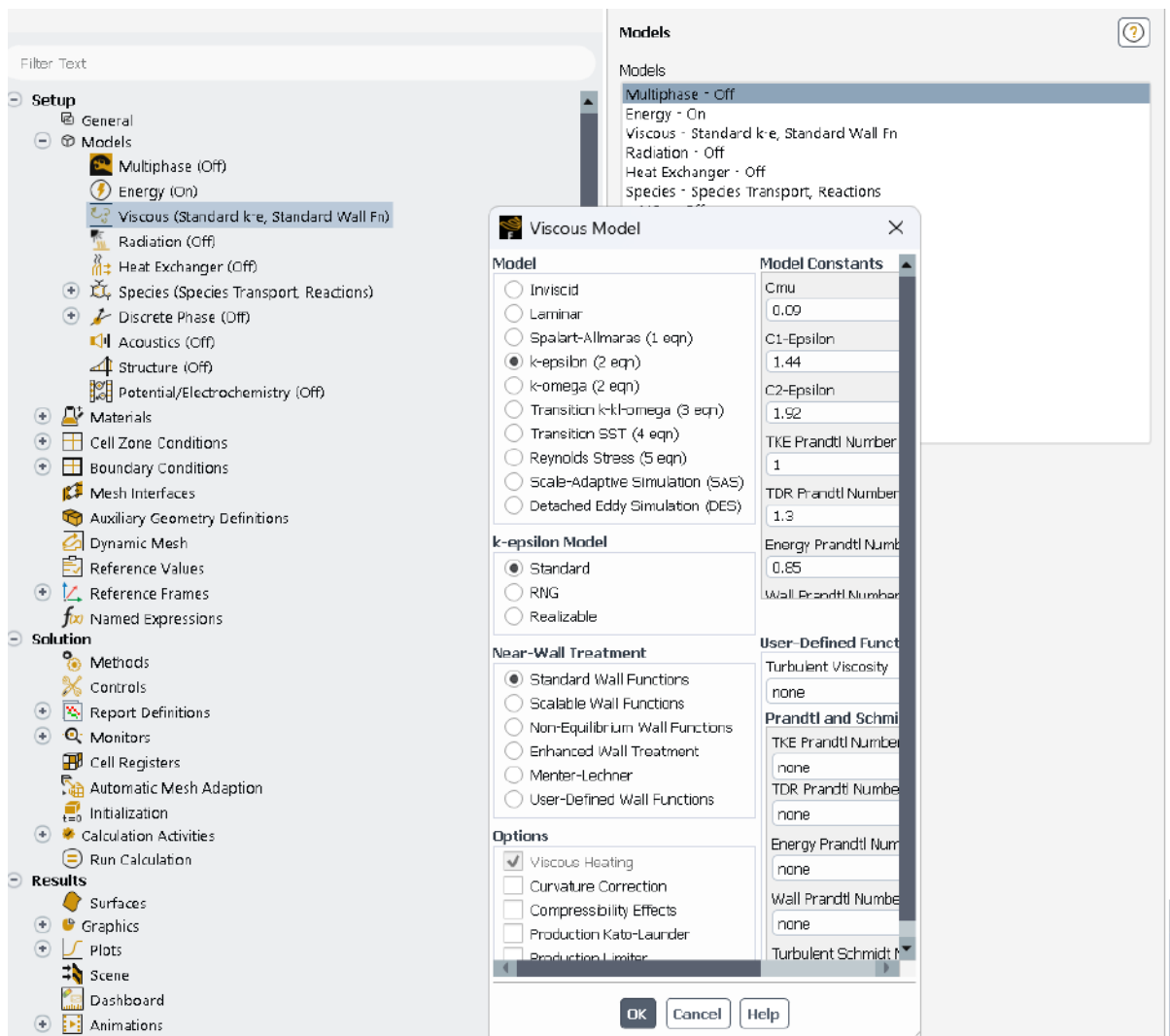


Figure 3.12: model standard k-ε, standard wall function, Energy equation turned on

Enable the energy equation for thermal analysis. Choose and configure the appropriate turbulence model in this case, standard k-ε

3.8.4 Species Model Configuration:

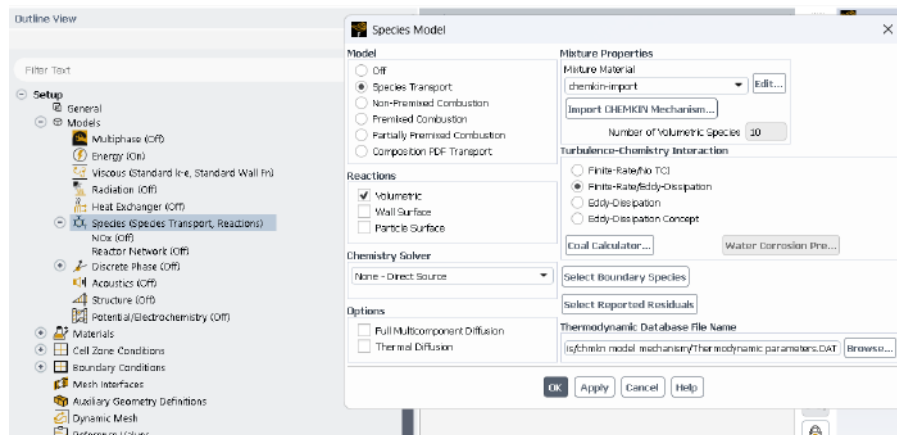


Figure 3.13: species transport activation

3.8.5 combustion mechanism

: Specify the combustion mechanism as global, detailed, or reduced mechanisms depending on the simulation requirements. In this study, at first, I did global mechanism followed by detailed mechanism of 13 equations as earlier alluded to. for the global, just select the Hydrogen-air mixture and then in reduced mechanism as shown above 3.13, then import the reaction mechanism file. Select Volumetric for the volumetric reactions and finally The combustion model is Finite rate/Eddy dissipation

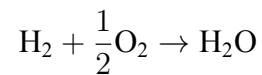
3.8.6 Materials Definition

In this simulation, appropriate materials were selected and defined in ANSYS Fluent to accurately capture the thermodynamic and transport properties of the working fluids. The primary materials used include:

- **Air:** Treated as a mixture of oxygen and nitrogen with standard thermophysical properties. Air was defined as an ideal gas to account for compressibility effects at high speeds.
- **Hydrogen (H₂):** Selected from the Fluent materials database. Hydrogen was also treated as an ideal gas. Its high diffusivity and low molecular weight make it suitable for high-speed combustion applications.
- **Water Vapor (H₂O):** Included as a product species in combustion simulations. It was defined to enable accurate modeling of combustion products and heat release.

All gases were assigned thermodynamic properties based on the ideal gas law. For reacting flow simulations, species transport and chemical reactions were enabled using the built-in Fluent species database. The materials were assigned to the appropriate fluid zones in the geometry to ensure physical accuracy of the domain. Change the viscosity to sutherland and density to ideal gas, and with this I can use pressure farfield later. In this work, I worked first with the cold flow, then hot flow with global mechanism reaction, then with a detailed mechanism reaction

case. For hydrogen-air combustion, Fluent's built-in database typically utilizes a single-step global reaction mechanism [22]:



This simplified approach, while computationally efficient, does not resolve the full chemical kinetics involved in hydrogen oxidation. Intermediate radicals such as OH, O, H, and HO₂ are not tracked, limiting the model's ability to capture key combustion phenomena, including ignition delay, flame stabilization via radical recombination, and detailed flame structure.

While such simplifications may be acceptable for basic engineering analyses or for capturing global combustion trends, they become inadequate for high-fidelity studies. Specifically, investigations involving flame propagation, shock–flame interactions, or thermochemical sensitivity—particularly in hypersonic and supersonic flow regimes—require more accurate kinetic representations. Therefore, to ensure a realistic simulation of flame behavior and reaction zone structures, detailed chemical mechanisms such as the LLNL mechanisms are employed in the later stages of this study.

The following sections present simulation results obtained using the global combustion model in *ANSYS Fluent*. These will subsequently be compared to results generated with a detailed reaction mechanism to evaluate the impact of chemical fidelity on combustion prediction and flow characteristics.

3.8.7 Setup of Boundary Conditions:

pressure farfield

o Apply the correct boundary conditions for **pressure farfield**,

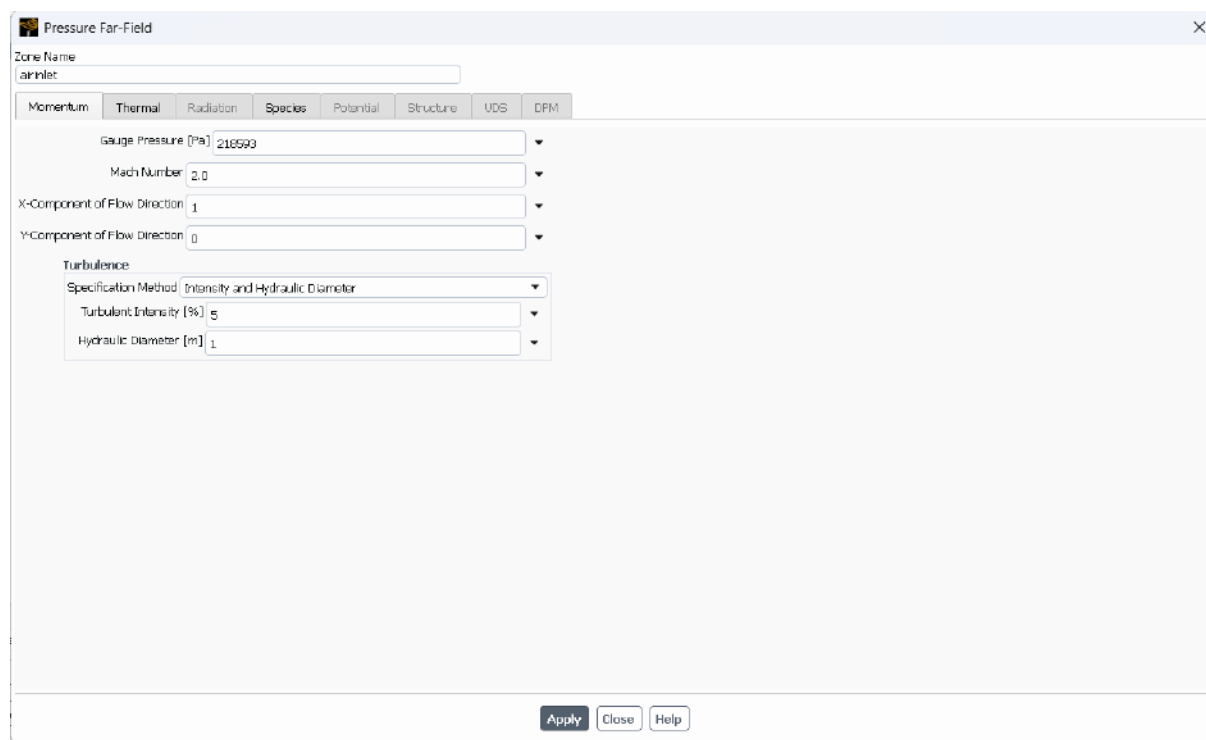


Figure 3.14: boundary conditions

temperature

- o Apply the correct boundary conditions for **temperature**,

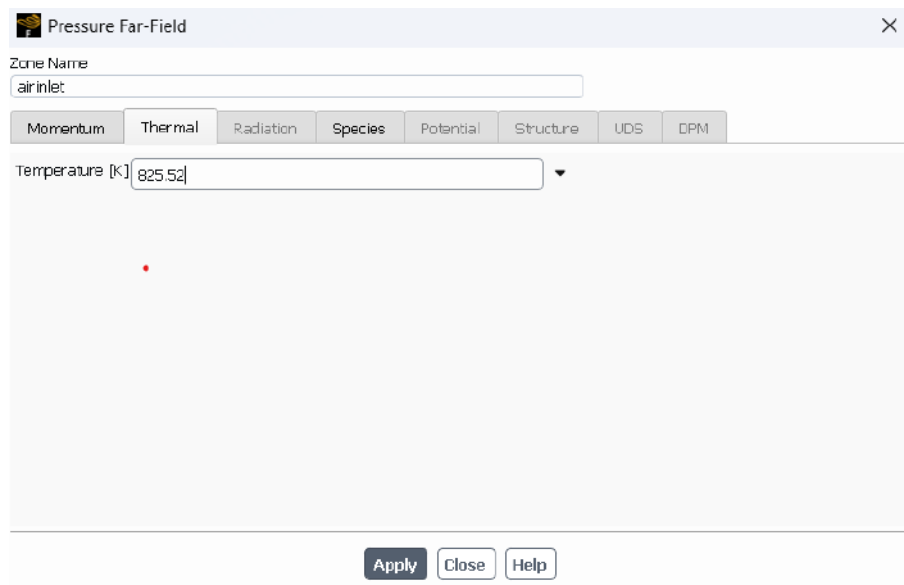


Figure 3.15: temperature for initial conditions at inlet

species concentration

- o Apply the correct boundary conditions for **species concentration**.

Pressure Far-Field

Zone Name
airinlet

Momentum Thermal Radiation **Species** Potential Structure UDS DPM

☐ Specify Species in Mole Fractions

Species Mass Fractions

h	0
h2	0
o	0
o2	0.2338
oh	0
h2o	0.0622

Apply Close Help

Figure 3.16: species concentration stage for input

3.8.8 Reference Values

Select the reference zone is surface-body and compute from air inlet.

Reference Values

Compute from
airinlet

Reference Values

Area [m²]	1
Density [kg/m³]	1.512845
Depth [m]	1
Enthalpy [J/kg]	1199423
Length [m]	1
Pressure [Pa]	110000
Temperature [K]	825
Velocity [m/s]	1251.537
Viscosity [kg/(m s)]	3.428542e-18
Ratio of Specific Heats	1.4
Yplus for Heat Tran. Coef.	300

Reference Zone
surface_body

Figure 3.17: reference values input zone

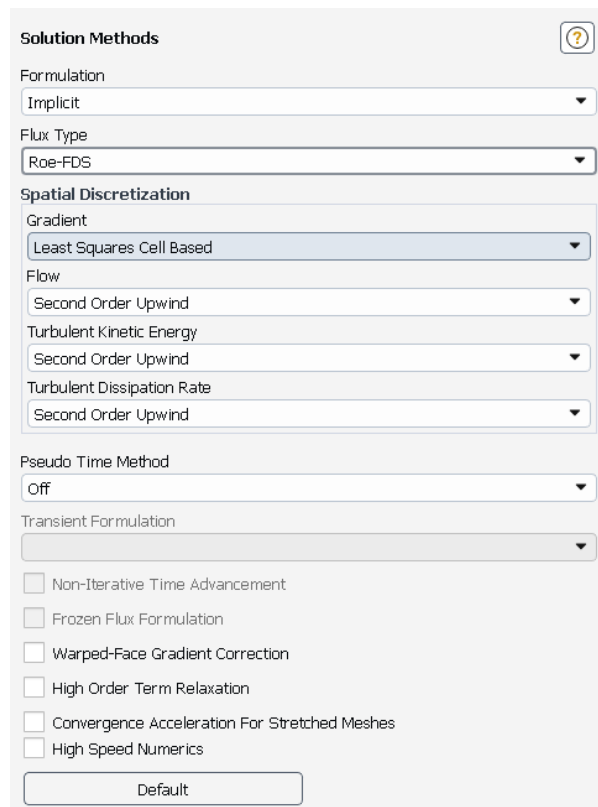
3.8.9 Solution Methods:

To ensure accurate and stable convergence of the governing equations, appropriate numerical schemes and solvers were selected in ANSYS Fluent. The following solution methods were applied:

- **Solver Type:** The pressure-based coupled solver was used due to its robustness in handling compressible flows, particularly at supersonic and hypersonic regimes. It allows for strong coupling between pressure and velocity fields.
- **Pressure-Velocity Coupling:** The *Coupled* scheme was employed to tightly couple the pressure and momentum equations, enhancing convergence in high-speed flow simulations.
- **Spatial Discretization:**
 - Formulation Implicit
 - Flux Type: Roe-FDS
 - Momentum: Second Order Upwind
 - Energy: Second Order Upwind
 - Turbulent kinetic Energy: Second Order Upwind (for reacting flows)
 - Turbulence Dissipation rate: Second Order Upwind
- **Turbulence Modeling:** The $k-\epsilon$ model was used for its accuracy in predicting boundary layer behavior and flow separation.
- **Temporal Discretization :** Second Order Implicit time-stepping method was used for higher accuracy with reasonable computational cost.

These settings were chosen to balance computational efficiency and accuracy, especially for complex flow structures such as shock waves, shear layers, and combustion-induced expansion regions.

3.8.10 Solution Controls



The image shows a software panel titled "Solution Methods" with a help icon (question mark in a circle) in the top right corner. The panel contains several configuration options:

- Formulation:** A dropdown menu with "Implicit" selected.
- Flux Type:** A dropdown menu with "Roe-FDS" selected.
- Spatial Discretization:**
 - Gradient:** A dropdown menu with "Least Squares Cell Based" selected.
 - Flow:** A dropdown menu with "Second Order Upwind" selected.
 - Turbulent Kinetic Energy:** A dropdown menu with "Second Order Upwind" selected.
 - Turbulent Dissipation Rate:** A dropdown menu with "Second Order Upwind" selected.
- Pseudo Time Method:** A dropdown menu with "Off" selected.
- Transient Formulation:** A dropdown menu with a downward arrow.
- Checkboxes:**
 - ☐ Non-Iterative Time Advancement
 - ☐ Frozen Flux Formulation
 - ☐ Warped-Face Gradient Correction
 - ☐ High Order Term Relaxation
 - ☐ Convergence Acceleration For Stretched Meshes
 - ☐ High Speed Numerics
- Default:** A button at the bottom of the panel.

Figure 3.18: solution methods

Select the appropriate **solver settings**, including pressure-velocity coupling and spatial discretization schemes.

3.9 Initialization:

Configure **solution controls** for numerical stability and accuracy. **Initialization of the solution** with appropriate flow parameters to ensure proper convergence.

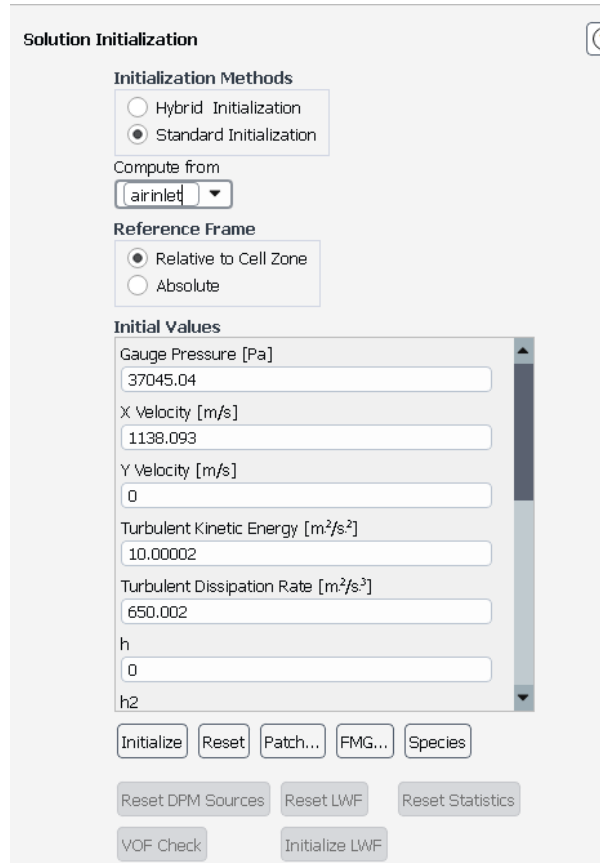


Figure 3.19: Initialisation stage

3.10 Run Simulation:

Here, we select the number of iterations to run and chose solution steering under supersonic flow conditions, and click calculate.

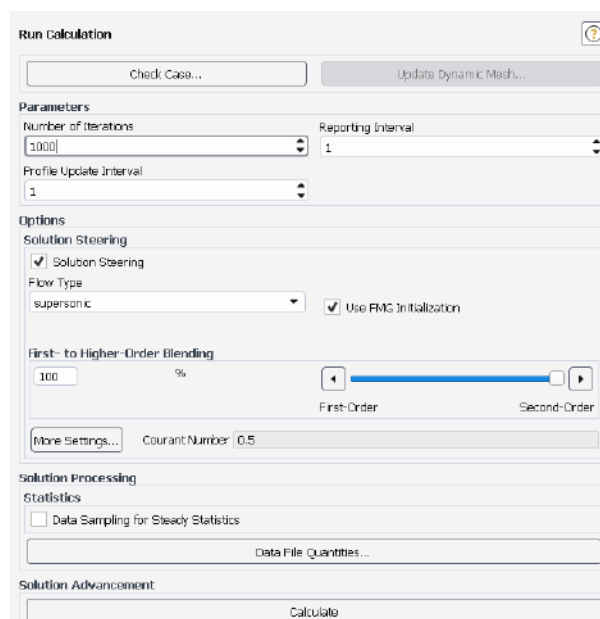


Figure 3.20: calculation stage of the ansys simlaton software in the simulation of combustion

3.11 Conclusion

The numerical modeling of the scramjet combustor using ANSYS tools has demonstrated good agreement with experimental benchmarks, confirming the validity of the computational setup and modeling strategy. The use of parallel cavity flame holders effectively enhanced fuel-air mixing and combustion efficiency. Structured mesh refinement and appropriate turbulence and combustion models enabled accurate prediction of key flow phenomena, including recirculation zones and shock wave interactions. Despite minor discrepancies in pressure prediction, the overall results confirm that the simulation approach is robust and capable of capturing the essential physics of supersonic combustion.

Chapter 4

Results and Discussion: Cold Flow

4.1 Introduction

This chapter presents cold flow (non-reacting) simulation results for a double-cavity scram-jet combustor at inlet Mach numbers **2.0** and **2.75**. The aim is to examine the aerodynamic field—specifically shock structures, shear layers, and recirculation zones—that drive fuel–air mixing ahead of combustion.

The selected Mach numbers span a relevant supersonic range, highlighting how cavity-driven flow features evolve with velocity. The cavity geometry is optimized to promote shear-layer roll-up and recirculation, both essential for mixing and flameholding.

Simulations were run with hydrogen injection but without combustion. Analysis focuses on static temperature, pressure, Mach number, density, and species mass fractions to assess mixing and identify ignition-favorable regions.

These results provide a baseline for the reacting flow analysis in the next chapter, where the same conditions are examined with global and detailed hydrogen-air reaction mechanisms.

4.1.1 Inlet Conditions Used

Table 4.1: Static temperature, static pressure, and gauge pressure for selected inlet Mach numbers ($M = 2.00$ and $M = 2.75$), assuming total pressure $P_0 = 1,600,000$ Pa and total temperature $T_0 = 1486$ K. Atmospheric pressure $P_{\text{atm}} = 101,325$ Pa.[22]

Mach Number	Static Temp. (K)	Static Press. (Pa)	Gauge Press. (Pa)
2.00	825.56	319,918	218,593
2.75	591.14	146,375	45,050

Simulation Setup and Notes on Convergence:

Cold flow simulations were conducted using ANSYS Fluent with hydrogen injection enabled but without combustion. The full numerical convergence was achieved, the solver ran for 1000 iterations over approximately 2 hours on a workstation with an Intel i5-12600HX CPU (16 processes) and an NVIDIA A1000 GPU.

4.2 Description and Discussion of Cold Supersonic Flow Key Contours and Flow Structures

Temperature Contours

The temperature contours, figure 4.1 ,and figure 4.2, for the cold flow cases at Mach 2.0 and Mach 2.75, respectively, exhibit modest rises near wall regions and in compression zones. These increases are attributed to viscous heating and shock-induced compression, particularly more evident at Mach 2.75. Despite the absence of combustion, these localized temperature elevations help highlight key aerodynamic features such as boundary layer effects and shock interactions.

Pressure Contours

The pressure contours, figure 4.3 ,and figure 4.4, reveal that the core region of the combustor experiences lower static pressure compared to the near-wall regions. This is due to wall-bounded shock reflections and boundary layer development. At both Mach 2.0 and Mach 2.75, shock structures are clearly visible, with increasing intensity at the higher Mach number. These shock formations help build pressure near the nozzle exit, contributing to thrust production. As inlet Mach number increases, the high-speed near-wall region expands, indicating stronger compression effects.

Mach Number Contours

At Mach 2.0, figure 4.5, the supersonic flow progresses smoothly through the combustor with limited compression effects and minimal shock activity. In contrast, at Mach 2.75, figure 4.6, shock waves and compression regions are more pronounced, particularly near the cavity walls. Both cases maintain supersonic conditions throughout the domain, validating the combustor geometry's ability to support stable supersonic flow prior to combustion. Mach number variations are governed by the inlet speed, area changes, and boundary layer interactions.

Density Contours

Density fields, figure 4.7 and figure 4.8, show pronounced gradients near the combustor walls and around shock zones. At Mach 2.75, figure 4.8, the core flow exhibits lower density due to increased expansion, while the wall-adjacent regions show localized density buildup. These patterns align with compressible flow behavior in supersonic regimes.

Enthalpy Contours

Total enthalpy remains nearly conserved throughout the combustor in both Mach 2.0 and 2.75 cases, figure 4.9 and figure 4.10, consistent with adiabatic flow conditions in non-reacting simulations. Slight reductions in enthalpy occur near the walls due to thermal and viscous effects, but the core flow maintains energy content, as expected.

Hydrogen Mass Fraction Contours

Since chemical reactions are disabled in cold flow simulations, the hydrogen mass fractions, figure 4.11 and figure 4.12, remains largely unchanged throughout the domain. Slight diffusion

near cavity shear layers is visible, indicating preliminary mixing behavior. This helps identify potential regions for ignition in subsequent reacting flow simulations.

Water Vapor Mass Fraction Contours

As expected in a non-reacting case, water vapor mass fraction, figure 4.13 and figure 4.14, remains effectively zero across the flow field, except for the minimal amounts introduced with the air stream. This confirms that no combustion occurred and serves as a baseline validation for cold flow setup integrity.

4.3 Visualisation of Cold Supersonic Flow Key Contours and Flow Structures

Preliminary cold flow results were obtained for inlet Mach numbers of 2.0 and 2.75. These cases were used to evaluate aerodynamic features earlier mentioned preparing to introduce species transport and combustion models.

The $k-\epsilon$ turbulence model was employed for its demonstrated ability to capture shock-boundary layer interactions and wall temperature distributions effectively. Inlet conditions were defined using a total pressure of 1,600,000 Pa and total temperature of 1486 K as shown in table 4.1.

4.3.1 Temperature Contours

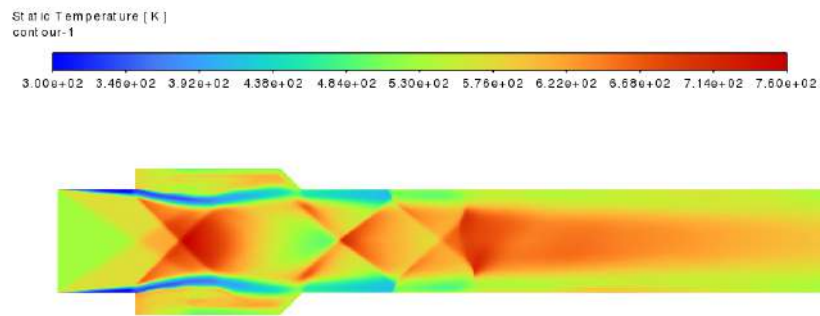


Figure 4.1: Temperature contour for a cold flow simulation with air at $M_{\text{air}} = 2.0$. Inlet conditions: air stream — $T_{\text{air}} = 825.56$ K, $P_{\text{air}} = 218,538$ Pa; hydrogen stream — $T_{\text{H}_2} = 300$ K, $P_{\text{H}_2} = 228,000$ Pa. This case is used as a baseline to analyze mixing characteristics in the absence of combustion.

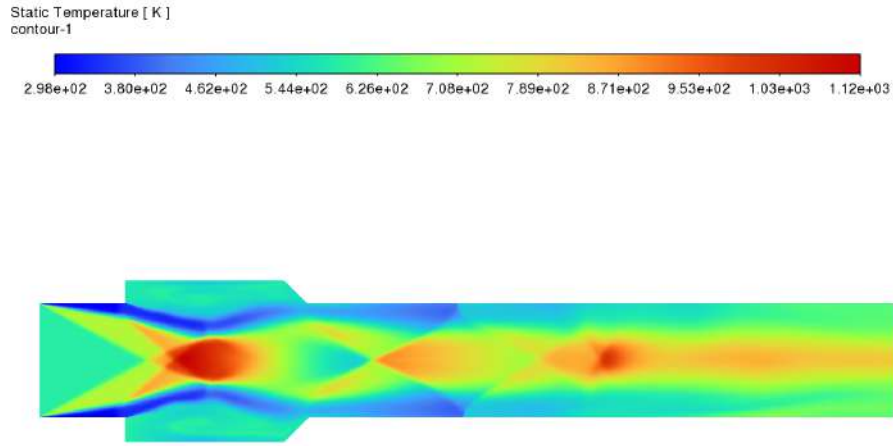


Figure 4.2: Temperature contour for a cold flow simulation with air at $M_{\text{air}} = 2.75$. Inlet conditions: air stream — $T_{\text{air}} = 591.14$ K, $P_{\text{air}} = 45,050$ Pa; hydrogen stream — $T_{\text{H}_2} = 300$ K, $P_{\text{H}_2} = 228,000$ Pa. This case is used as a baseline to analyze mixing characteristics in the absence of combustion.

4.3.2 Pressure Contours at different mach inlet values.

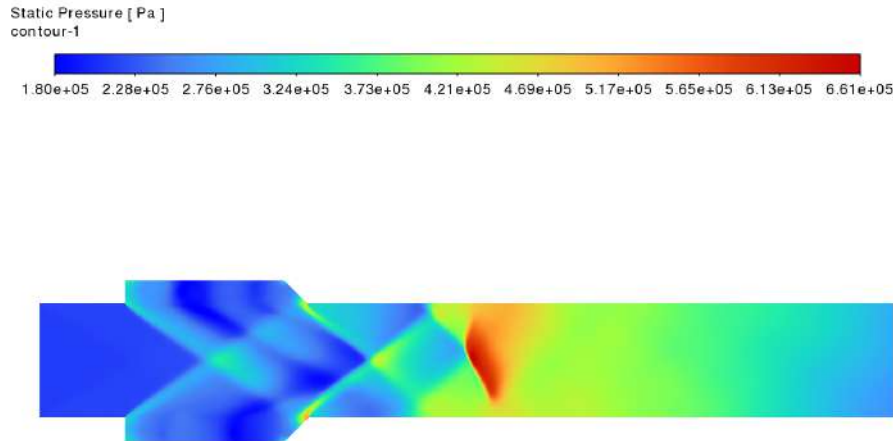


Figure 4.3: Pressure contour for a stoichiometric hydrogen-air mixture under cold flow at Mach 2.0. Inlet conditions are: air at $M_{\text{air}} = 2.0$, $T_{\text{air}} = 825.56$ K, $P_{\text{air}} = 218,593$ Pa; hydrogen at $M_{\text{H}_2} = 1.0$, $T_{\text{H}_2} = 300$ K, $P_{\text{H}_2} = 228,000$ Pa.

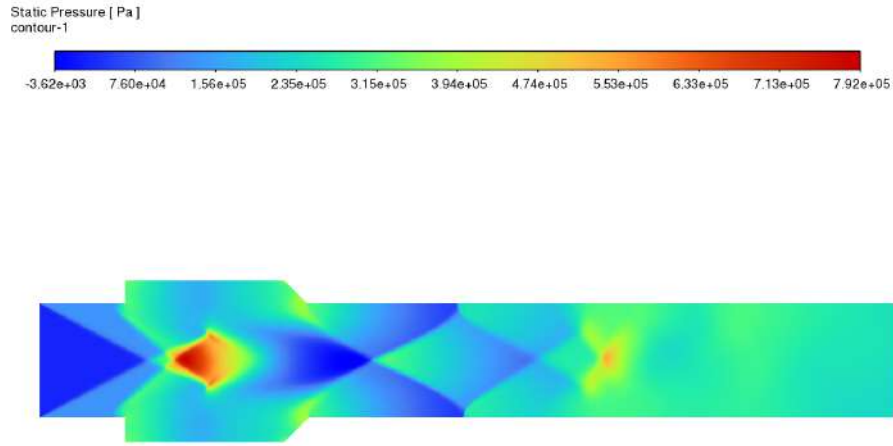


Figure 4.4: Pressure contour for a stoichiometric hydrogen-air mixture under cold flow at Mach 2.75. Inlet conditions are: air at $M_{\text{air}} = 2.75$, $T_{\text{air}} = 591.14$ K, $P_{\text{air}} = 45,050$ Pa; hydrogen at $M_{\text{H}_2} = 1.0$, $T_{\text{H}_2} = 300$ K, $P_{\text{H}_2} = 228,000$ Pa.

4.3.3 Velocity Contours at different mach inlet values.

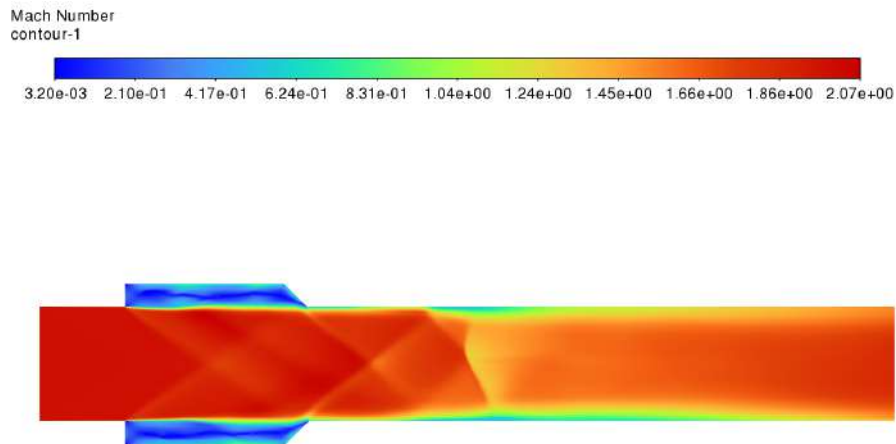


Figure 4.5: Mach-number contour for a stoichiometric hydrogen-air mixture under cold flow at Mach 2.0. Inlet conditions are: air at $M_{\text{air}} = 2.0$, $T_{\text{air}} = 825.56$ K, $P_{\text{air}} = 218,593$ Pa; hydrogen at $M_{\text{H}_2} = 1.0$, $T_{\text{H}_2} = 300$ K, $P_{\text{H}_2} = 228,000$ Pa.

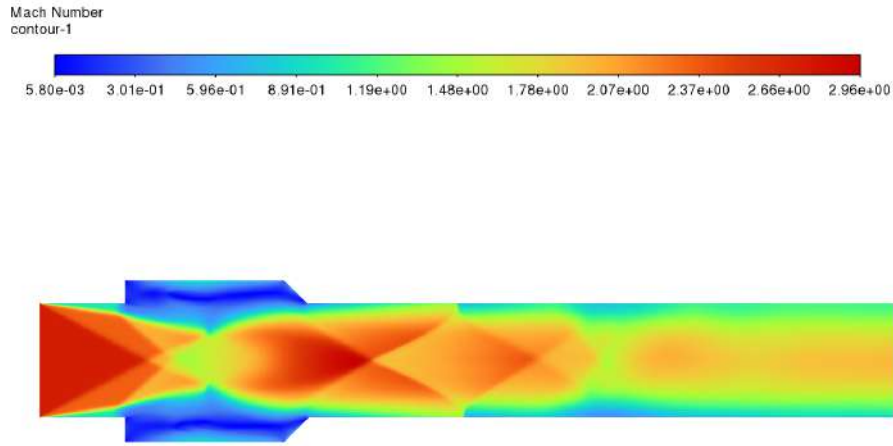


Figure 4.6: Temperature contour for a stoichiometric hydrogen-air mixture under cold flow at Mach 2.75. Inlet conditions are: air at $M_{\text{air}} = 2.75$, $T_{\text{air}} = 591.14$ K, $P_{\text{air}} = 45,050$ Pa; hydrogen at $M_{\text{H}_2} = 1.0$, $T_{\text{H}_2} = 300$ K, $P_{\text{H}_2} = 228,000$ Pa.

4.3.4 Density Contours for different inlet mach number values.

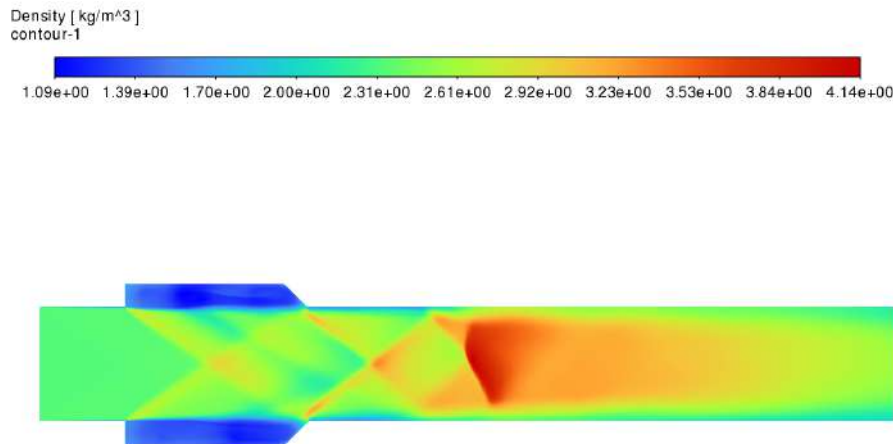


Figure 4.7: Density contour for a stoichiometric hydrogen-air mixture with cold flow. Inlet conditions are: air at $M_{\text{air}} = 2.0$, $T_{\text{air}} = 825.56$ K, $P_{\text{air}} = 218,538$ Pa; hydrogen at $M_{\text{H}_2} = 1.0$, $T_{\text{H}_2} = 300$ K, $P_{\text{H}_2} = 228,000$ Pa.

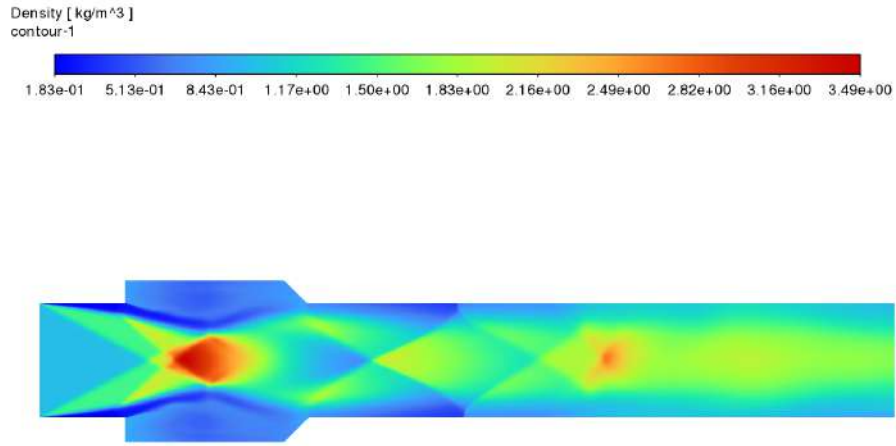


Figure 4.8: Density contour for a stoichiometric hydrogen-air mixture with cold flow. Inlet conditions are: air at $M_{\text{air}} = 2.75$, $T_{\text{air}} = 591.14$ K, $P_{\text{air}} = 45,050$ Pa; hydrogen at $M_{\text{H}_2} = 1.0$, $T_{\text{H}_2} = 300$ K, $P_{\text{H}_2} = 228,000$ Pa.

4.3.5 Enthalpy Contours for the double cavity combustor at different inlet mach number values

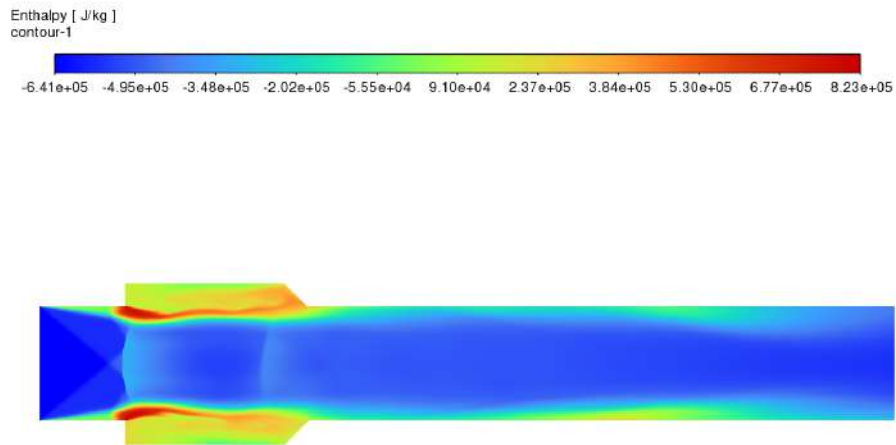


Figure 4.9: Enthalpy contour for a stoichiometric hydrogen-air mixture with cold flow. Inlet conditions are: air at $M_{\text{air}} = 2.0$, $T_{\text{air}} = 825.56$ K, $P_{\text{air}} = 218,538$ Pa; hydrogen at $M_{\text{H}_2} = 1.0$, $T_{\text{H}_2} = 300$ K, $P_{\text{H}_2} = 228,000$ Pa.

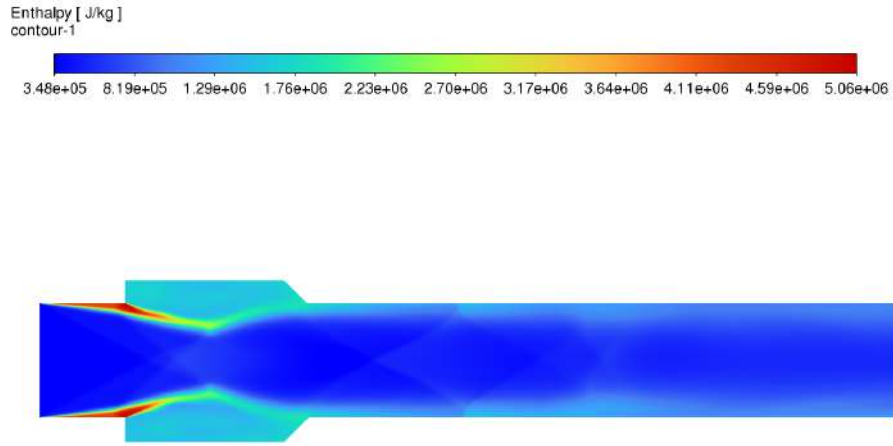


Figure 4.10: Enthalpy contour for a stoichiometric hydrogen-air mixture with cold flow. Inlet conditions are: air at $M_{\text{air}} = 2.75$, $T_{\text{air}} = 591.14$ K, $P_{\text{air}} = 45,050$ Pa; hydrogen at $M_{\text{H}_2} = 1.0$, $T_{\text{H}_2} = 300$ K, $P_{\text{H}_2} = 228,000$ Pa.

4.3.6 Hydrogen mass fraction contour for double cavity combustor at different inlet mach number values.

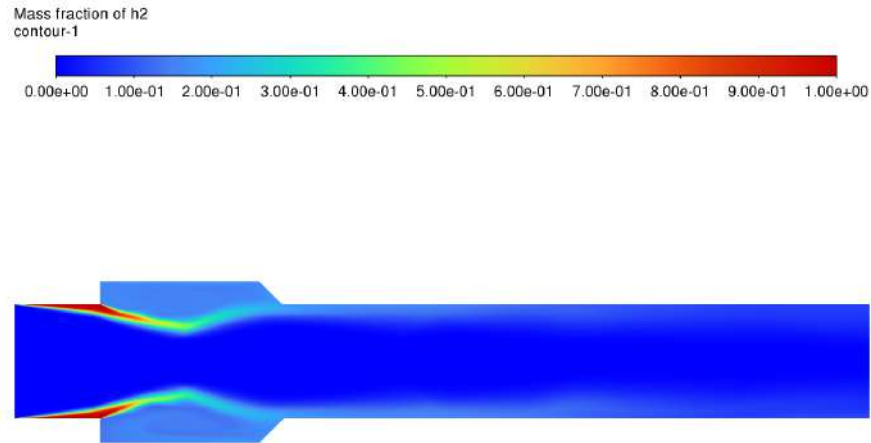


Figure 4.11: Contour of hydrogen mass fraction, Y_{H_2} , for a supersonic **cold flow** case. The inlet conditions are: hydrogen stream at $M_{\text{H}_2} = 1.0$, $P_{\text{H}_2} = 228,000$ Pa, $T_{\text{H}_2} = 300$ K, with $Y_{\text{H}_2} = 1.0$; and air stream at $M_{\text{air}} = 2.0$, $P_{\text{air}} = 218,538$ Pa, $T_{\text{air}} = 825.56$ K.

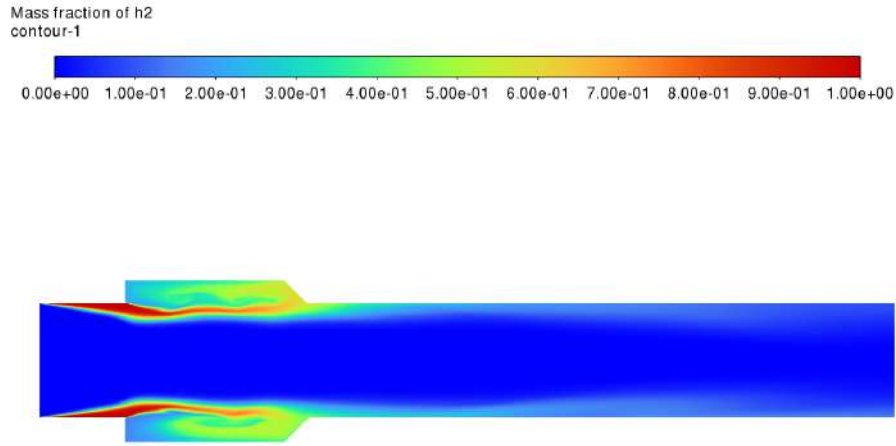


Figure 4.12: Contour of hydrogen mass fraction, Y_{H_2} , for a supersonic cold flow case. The inlet conditions are: hydrogen stream at $M_{H_2} = 1.0$, $P_{H_2} = 228,000$ Pa, $T_{H_2} = 300$ K, with $Y_{H_2} = 1.0$; and air stream at $M_{air} = 2.75$, $P_{air} = 45,050$ Pa, $T_{air} = 591.14$ K.

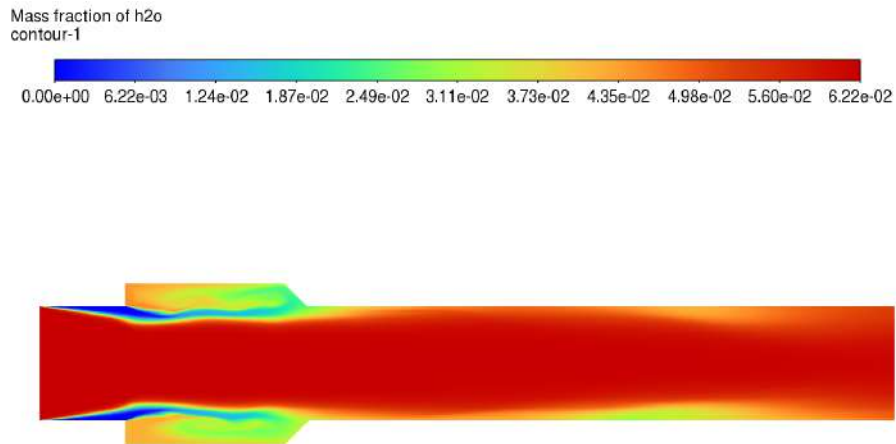


Figure 4.13: Contour of hydrogen mass fraction, Y_{H_2} , for a supersonic cold flow case. The inlet conditions are: hydrogen stream at $M_{H_2} = 1.0$, $P_{H_2} = 228,000$ Pa, $T_{H_2} = 300$ K, with $Y_{H_2} = 1.0$; and air stream at $M_{air} = 2.75$, $P_{air} = 45,050$ Pa, $T_{air} = 591.14$ K.

Mass fraction of h2o
contour-1

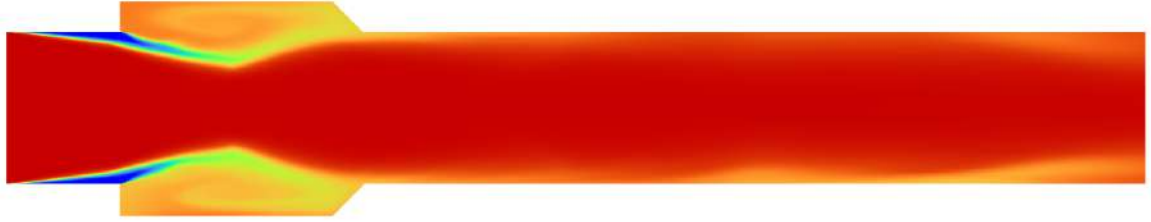
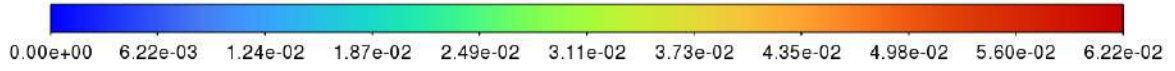
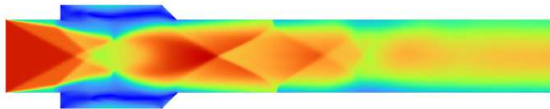


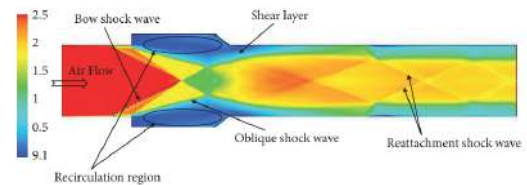
Figure 4.14: Contour of water vapor mass fraction, Y_{H_2O} , for a supersonic cold flow case. The inlet conditions are: hydrogen stream at $M_{H_2} = 1.0$, $P_{H_2} = 228,000$ Pa, $T_{H_2} = 300$ K, with $Y_{H_2} = 1.0$; and air stream at $M_{air} = 2.75$, $P_{air} = 45,050$ Pa, $T_{air} = 591.14$ K. As no chemical reaction occurs in this cold flow case, Y_{H_2O} should remain close to zero.

4.4 Vaidation of the results

Mach Number
contour-1



(a) Mach number contour from the present simulation



(b) Reference Mach contour

Figure 4.15: Validation of the numerical model using Mach number contours. The simulation result (left) is compared with reference data (right) from [22]. Key flow features such as shock locations, boundary interactions, and supersonic core patterns show close agreement, supporting the credibility of the model.

4.5 Conclusion – Cold Flow Simulation

Cold flow simulations at Mach 2.0 and Mach 2.75 provide valuable insight into the aerodynamic structures present in the scramjet combustor prior to ignition. Supersonic flow is maintained in both cases, with stronger shock and compression features at higher Mach numbers. Temperature and density contours align with compressible flow theory, and hydrogen mass fraction remains conserved except for slight shear-induced mixing. Enthalpy is well conserved, and water vapor content is negligible, validating the non-reactive flow assumption. These findings establish a baseline for evaluating combustion behavior in the next chapter.

Chapter 5

Results and Discussion: Global and detailed hydrogen Combustion Analysis

5.1 Introduction

This chapter presents the results and analysis of supersonic reacting flow simulations within a double-cavity scramjet combustor, focusing on two inlet Mach numbers: 2.0 and 2.75. Global and detailed hydrogen-air reaction mechanisms were employed to assess their influence on flame behavior, ignition, and overall combustion characteristics under different operating regimes, with global starting then later the .

Simulations were conducted across a range of equivalence ratios ($\phi = 0.6, 1.0, 2.3, \text{ and } 2.5$) to investigate the effects of lean, stoichiometric, and rich mixtures. These values were chosen to capture typical operating conditions and evaluate combustion efficiency, flame propagation, and heat release under varying fuel-air mixing scenarios.

The analysis includes key flow and thermochemical variables such as static temperature, pressure, Mach number, density, enthalpy, and species mass fractions (Y_{H_2}, Y_{H_2O}). Contour plots provide qualitative insight into flow structure, flame zones, and energy distribution. Special attention is given to differences between the global and detailed reaction models, particularly their sensitivity to inflow Mach number and fuel-air ratio.

These results help define the performance boundaries of the combustor in supersonic regimes and form the basis for evaluating flammability limits and combustion stability in subsequent sections.

5.2 Global reaction

5.2.1 Discussion of the global combustion key contours and flow structure

Comment on temperature Contours at Equivalence Ratios and air inlet Mach Numbers

The global reaction mechanism results in significant temperature increases, from figure 5.1 to figure 5.6, within the combustor, particularly near the cavity flameholding zones and core reaction regions. At $\phi = 0.6$, lower temperatures are observed due to lean combustion, while stoichiometric ($\phi = 1.0$) and rich mixtures ($\phi = 2.3$) yield higher peak temperatures due to greater heat release.

An increase in Mach number from 2.0 to 2.75 shifts the shock structures downstream and intensifies shear layers, promoting stronger mixing and more efficient combustion. Consequently,

peak temperatures rise and become more spatially distributed in the combustor at higher Mach numbers.

These findings illustrate the influence of both equivalence ratio and inlet velocity on heat release, combustion intensity, and flame stabilization when using the global reaction mechanism.

Comment on Pressure Contours at Different Equivalence Ratios and air inlet Mach Numbers

The pressure contours, from figure 5.7 to figure 5.12, under reacting conditions show complex shock interactions and compression waves forming within and around the cavities. With increasing equivalence ratio, pressure rises in the combustion zones due to heat addition. Higher Mach numbers shift these pressure peaks downstream and sharpen the gradients, reflecting stronger compressibility and momentum transfer.

Regions behind the strut and inside the cavities exhibit high-pressure zones—key areas for anchoring the flame. These variations in pressure support efficient combustion propagation and contribute to the overall thrust.

Comment on Mach Number Contours at Different Equivalence Ratios and air inlet Mach Numbers

The Mach number contours, figure 5.13 to figure 5.18, show distributions reveal the evolution of acceleration and deceleration regions due to combustion and shock structures. In reacting flows, combustion-induced expansion reduces local Mach numbers within flame zones, especially at higher ϕ values.

At higher inlet Mach numbers (e.g., $M = 2.75$), stronger shocks and flow expansions occur, with deceleration clearly observed in combustion zones, while the supersonic core maintains higher Mach levels in downstream sections.

Comment on Density Contours at Different Equivalence Ratios and air inlet Mach Numbers

Combustion leads to a sharp drop in local density in regions of heat release. With increasing ϕ , and higher density in regions of shocks and compression, figure 5.19 to figure 5.24, the density decrease becomes more pronounced, corresponding to stronger expansion from exothermic reactions.

At $M = 2.75$, the density gradients become steeper, especially downstream of the strut and cavities, due to intensified combustion and stronger flow expansion. This behavior is critical for thrust generation and flame stabilization.

Comment on Enthalpy Contours at Different Equivalence Ratios and air inlet Mach Numbers

Enthalpy contours, figure 5.31 to figure 5.36, show the distribution of thermal energy across the flow domain. In reacting cases, enthalpy increases significantly in the combustion zones and remains high downstream, following the flame front.

Higher equivalence ratios contribute to greater heat release and higher enthalpy values. As Mach number increases, the overall enthalpy distribution shifts further downstream due to delayed but more vigorous combustion from enhanced mixing and shock-induced ignition zones.

Comment on Hydrogen Mass Fraction Contours at Different Equivalence Ratios and air inlet Mach Numbers

The hydrogen mass fraction, figure 5.31 to figure 5.36, decreases progressively in the reaction zones, with the rate of reduction depending on ϕ and inlet Mach number. Lean cases retain more unburned fuel downstream, while stoichiometric and rich mixtures show more complete fuel consumption.

At higher Mach numbers, enhanced mixing and cavity-induced recirculation improve combustion completeness, leading to steeper declines in hydrogen concentration along the combustor length.

Comment Water Vapor Mass Fraction Contours at different equivalence ratios and air inlet mach numbers

Contours of Y_{H_2O} , figure 5.37 to figure 5.42, show increased product formation with rising equivalence ratio, especially near recirculation zones. Higher Mach numbers enhance mixing, but peak water formation remains lower than in detailed mechanism cases.

5.2.2 Visualisation of key contours and flow structure on global hydrogen combustion

This section compares the effect of equivalence ratio (ϕ) on the combustion field for two inlet Mach numbers: $M = 2.0$ and $M = 2.75$. For each Mach number, results from global chemical reaction mechanisms are shown and discussed.

Temperature Contours at Different Equivalence Ratios and Mach Numbers

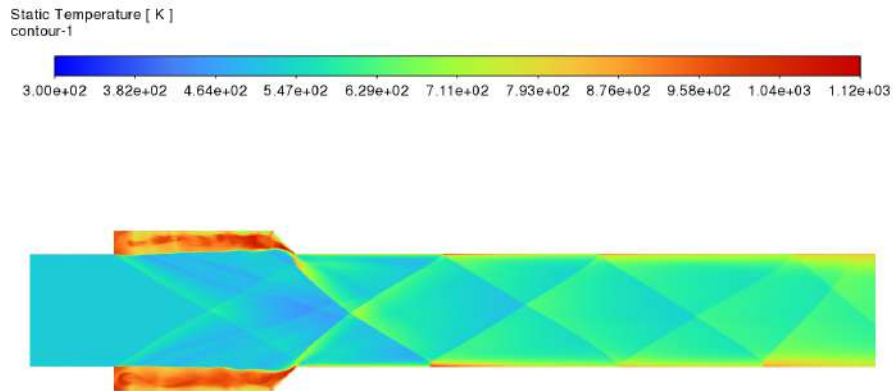


Figure 5.1: Temperature contour for reacting flow using the **global reaction mechanism** at $\phi = 0.6$. Inlet conditions: hydrogen stream at $M_{H_2} = 0.6$, $P_{H_2} = 228,000$ Pa, $T_{H_2} = 300$ K; air stream at $M_{air} = 2.0$, $P_{air} = 218,593$ Pa, $T_{air} = 825.56$ K.

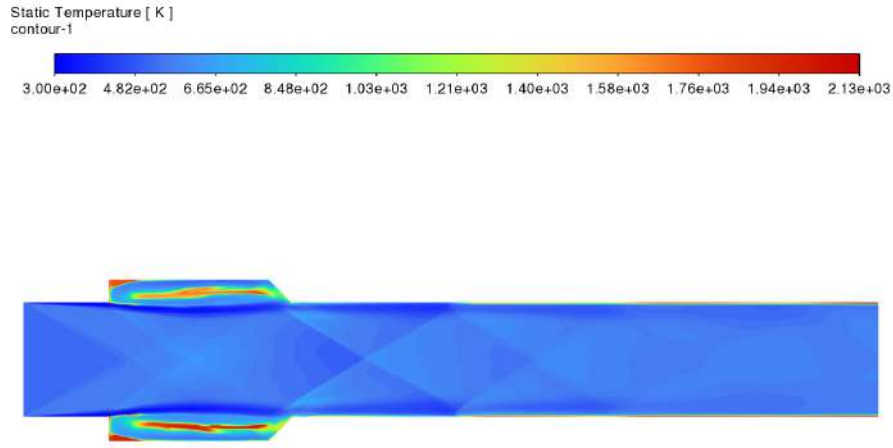


Figure 5.2: Temperature contour for reacting flow using the **global reaction mechanism** at $\phi = 1.0$. Inlet conditions: hydrogen stream at $M_{H_2} = 1.0$, $P_{H_2} = 228,000$ Pa, $T_{H_2} = 300$ K; air stream at $M_{air} = 2.0$, $P_{air} = 218,593$ Pa, $T_{air} = 825.56$ K.

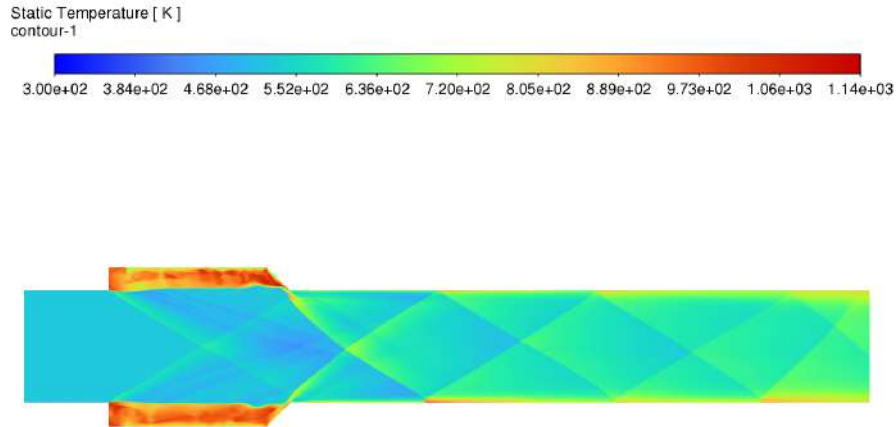


Figure 5.3: Temperature contour for reacting flow using the **global reaction mechanism** at $\phi = 2.3$. Inlet conditions: hydrogen stream at $M_{H_2} = 1.0$, $P_{H_2} = 110,000$ Pa, $T_{H_2} = 300$ K; air stream at $M_{air} = 2.0$, $P_{air} = 218,593$ Pa, $T_{air} = 825.56$ K.

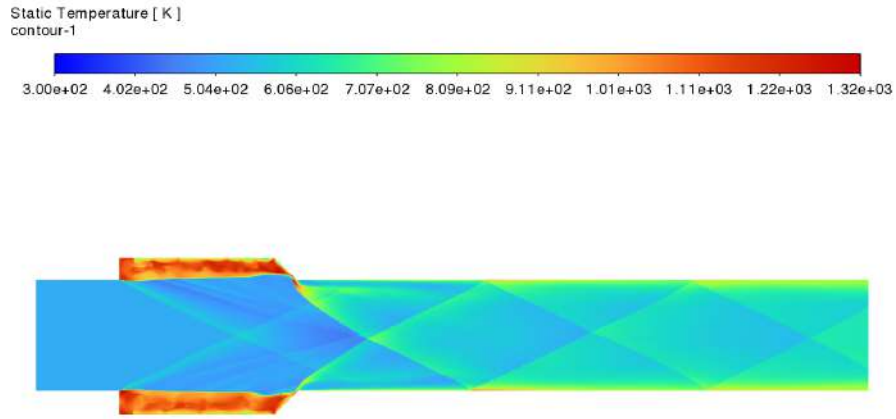


Figure 5.4: Temperature contour for reacting flow using the **global reaction mechanism** at $\phi = 0.6$. Inlet conditions: hydrogen stream at $M_{H_2} = 0.6$, $P_{H_2} = 228,000$ Pa, $T_{H_2} = 300$ K; air stream at $M_{air} = 2.75$, $P_{air} = 45,050$ Pa, $T_{air} = 591.14$ K.

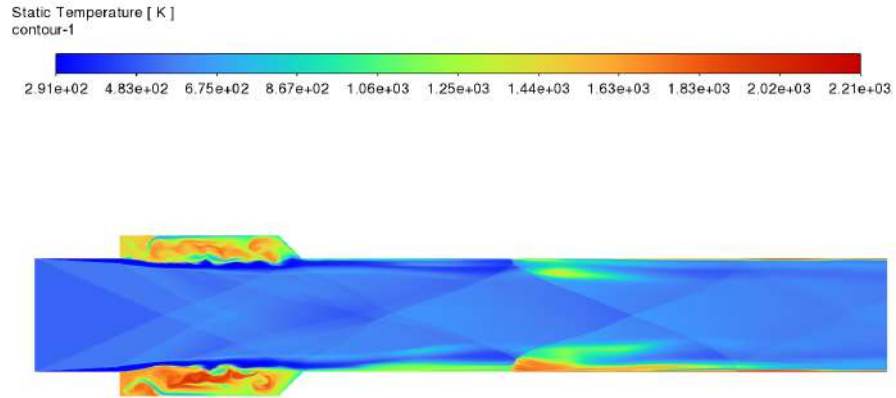


Figure 5.5: Temperature contour for reacting flow using the **global reaction mechanism** at $\phi = 1.0$. Inlet conditions: hydrogen stream at $M_{H_2} = 1.0$, $P_{H_2} = 228,000$ Pa, $T_{H_2} = 300$ K; air stream at $M_{air} = 2.75$, $P_{air} = 45,050$ Pa, $T_{air} = 591.14$ K.

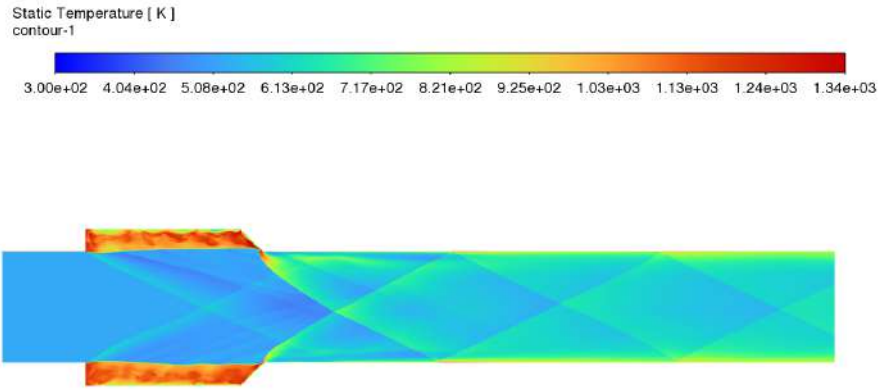


Figure 5.6: Temperature contour for reacting flow using the **global reaction mechanism** at $\phi = 2.5$. Inlet conditions: hydrogen stream at $M_{H_2} = 1.0$, $P_{H_2} = 570,000$ Pa, $T_{H_2} = 300$ K; air stream at $M_{air} = 2.75$, $P_{air} = 45,050$ Pa, $T_{air} = 591.14$ K.

Pressure Contours at Different Equivalence Ratios and Mach Numbers

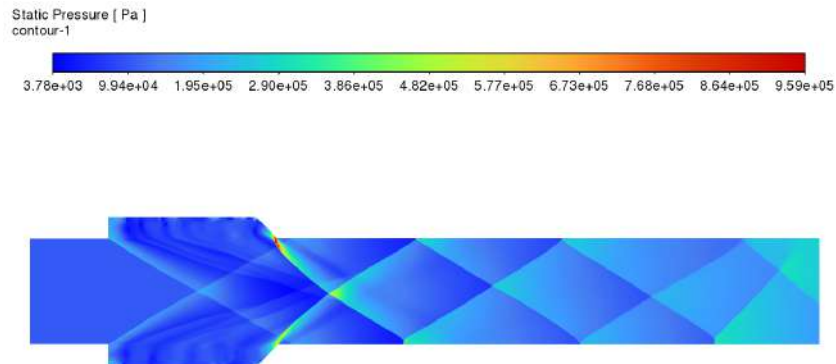


Figure 5.7: Pressure contour for reacting flow using the global reaction mechanism at $\phi = 0.6$. Inlet conditions: hydrogen stream at $M_{H_2} = 1.0$, $P_{H_2} = 228,000$ Pa, $T_{H_2} = 300$ K; air stream at $M_{air} = 2.0$, $P_{air} = 218,538$ Pa, $T_{air} = 825.56$ K.

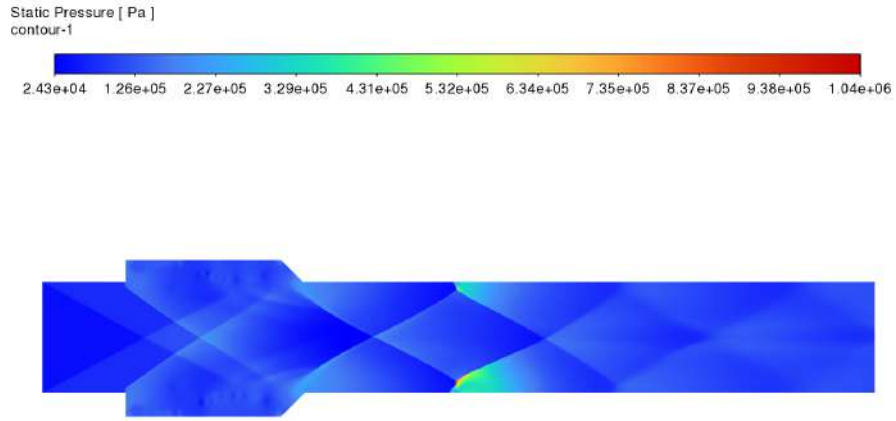


Figure 5.8: Pressure contour for reacting flow using the global reaction mechanism at $\phi = 1.0$. Inlet conditions: H_2 stream at $M_{H_2} = 1.0$, $P_{H_2} = 228,000$ Pa, $T_{H_2} = 300$ K; air stream at $M_{air} = 2.0$, $P_{air} = 218,538$ Pa, $T_{air} = 825.56$ K.

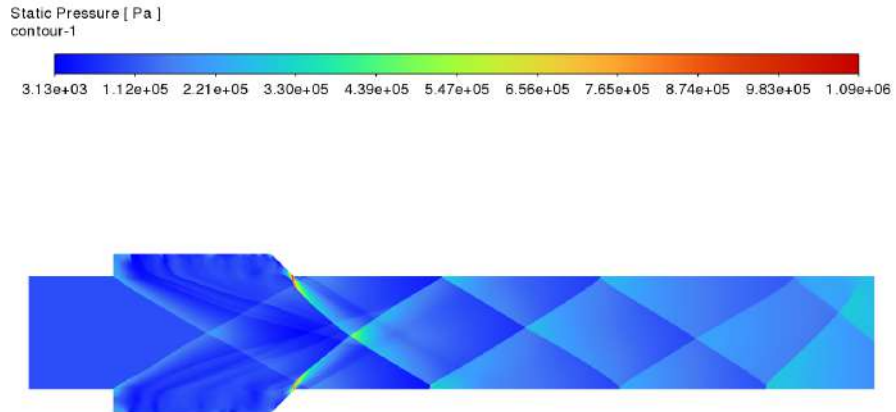


Figure 5.9: Pressure contour for reacting flow using the global reaction mechanism at $\phi = 2.3$. Inlet conditions: H_2 stream at $M_{H_2} = 1.0$, $P_{H_2} = 228,000$ Pa, $T_{H_2} = 300$ K; air stream at $M_{air} = 2.0$, $P_{air} = 218,538$ Pa, $T_{air} = 825.56$ K.

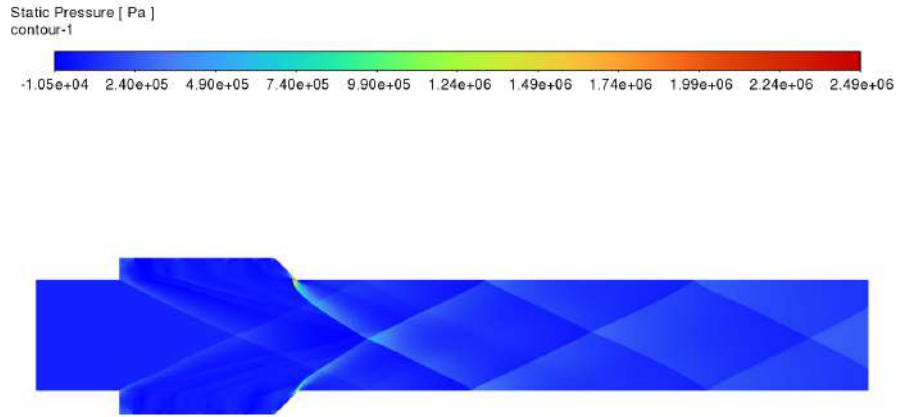


Figure 5.10: Pressure contour for reacting flow using the global reaction mechanism at $\phi = 0.6$. Inlet conditions: H_2 stream at $M_{H_2} = 1.0$, $P_{H_2} = 228,000$ Pa, $T_{H_2} = 300$ K; air stream at $M_{air} = 2.75$, $P_{air} = 45,050$ Pa, $T_{air} = 591.14$ K.

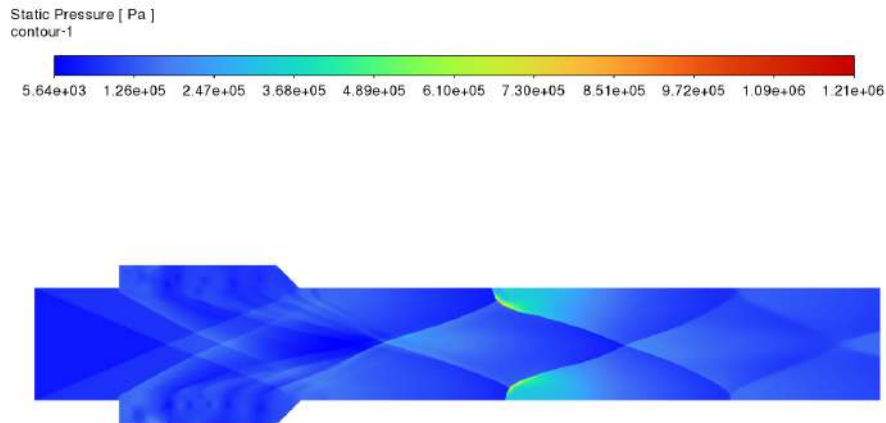


Figure 5.11: Pressure contour for reacting flow using the global reaction mechanism at $\phi = 1.0$. Inlet conditions: H_2 stream at $M_{H_2} = 1.0$, $P_{H_2} = 228,000$ Pa, $T_{H_2} = 300$ K; air stream at $M_{air} = 2.75$, $P_{air} = 45,050$ Pa, $T_{air} = 591.14$ K.

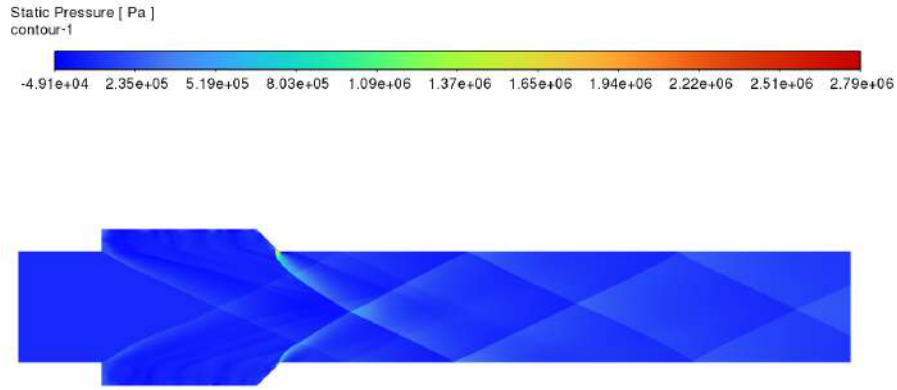


Figure 5.12: Pressure contour for reacting flow using the global reaction mechanism at $\phi = 2.3$. Inlet conditions: H_2 stream at $M_{H_2} = 1.0$, $P_{H_2} = 228,000$ Pa, $T_{H_2} = 300$ K; air stream at $M_{air} = 2.75$, $P_{air} = 45,050$ Pa, $T_{air} = 591.14$ K.

Mach Number Contours at Different Equivalence Ratios and Mach Numbers

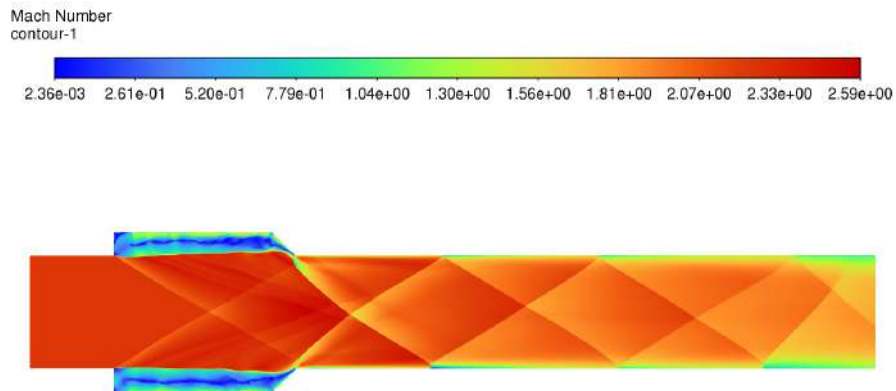


Figure 5.13: Mach number contour for reacting flow using the global reaction mechanism at $\phi = 0.6$. Inlet conditions: H_2 stream at $M_{H_2} = 1.0$, $P_{H_2} = 228,000$ Pa, $T_{H_2} = 300$ K; air stream at $M_{air} = 2.0$, $P_{air} = 218,538$ Pa, $T_{air} = 825.56$ K.

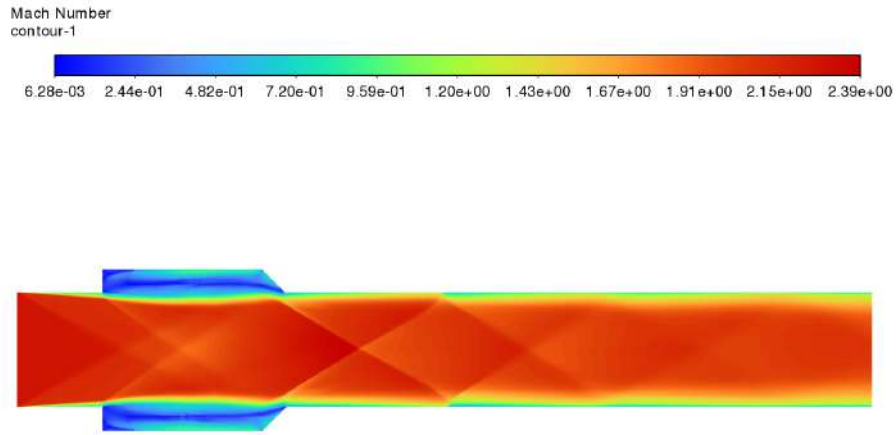


Figure 5.14: Mach number contour for reacting flow using the global reaction mechanism at $\phi = 1.0$. Inlet conditions: H_2 stream at $M_{H_2} = 1.0$, $P_{H_2} = 228,000$ Pa, $T_{H_2} = 300$ K; air stream at $M_{air} = 2.0$, $P_{air} = 218,538$ Pa, $T_{air} = 825.56$ K.

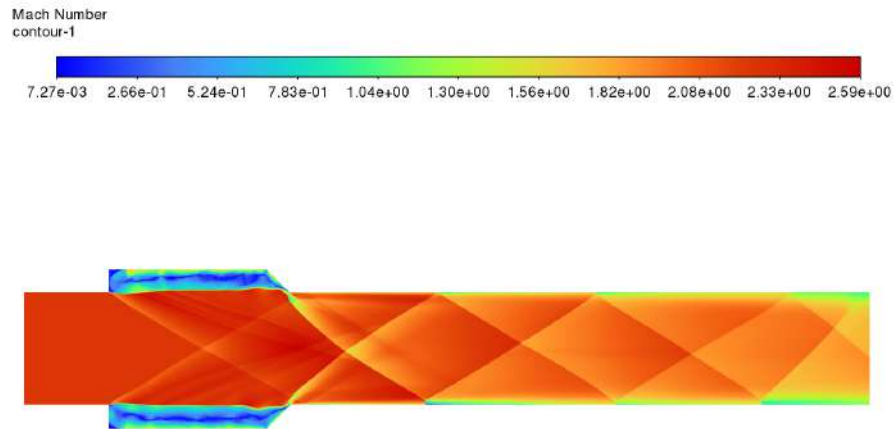


Figure 5.15: Mach number contour for reacting flow using the global reaction mechanism at $\phi = 2.3$. Inlet conditions: H_2 stream at $M_{H_2} = 1.0$, $P_{H_2} = 228,000$ Pa, $T_{H_2} = 300$ K; air stream at $M_{air} = 2.0$, $P_{air} = 218,538$ Pa, $T_{air} = 825.56$ K.

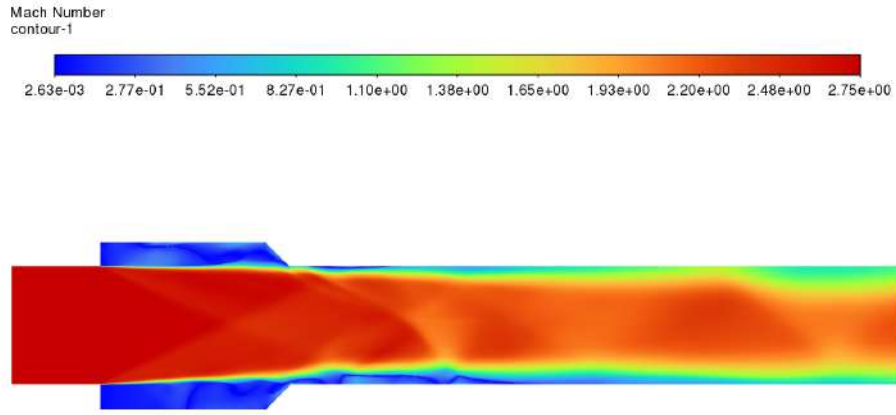


Figure 5.16: Mach number contour for reacting flow using the detailed reaction mechanism at $\phi = 0.6$. Inlet conditions: H_2 stream at $M_{H_2} = 1.0$, $P_{H_2} = 570,000$ Pa, $T_{H_2} = 300$ K; air stream at $M_{air} = 2.75$, $P_{air} = 45,050$ Pa, $T_{air} = 591.14$ K.

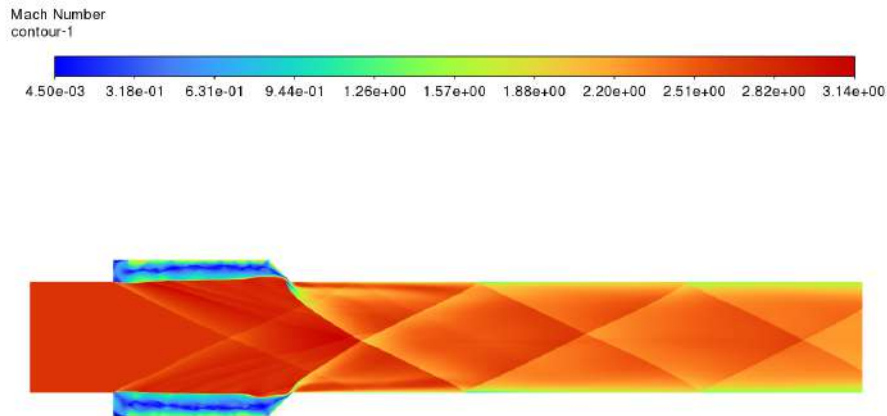


Figure 5.17: Mach number contour for reacting flow using the global reaction mechanism at $\phi = 1.0$. Inlet conditions: H_2 stream at $M_{H_2} = 1.0$, $P_{H_2} = 570,000$ Pa, $T_{H_2} = 300$ K; air stream at $M_{air} = 2.75$, $P_{air} = 45,050$ Pa, $T_{air} = 591.14$ K.

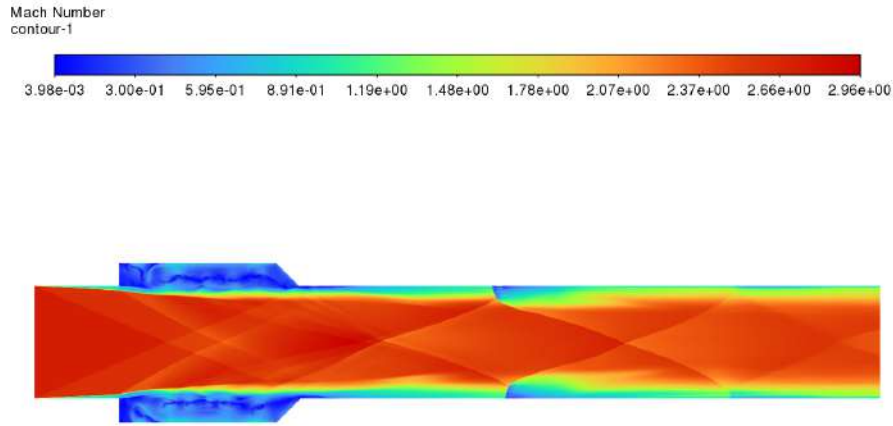


Figure 5.18: Mach number contour for reacting flow using the global reaction mechanism at $\phi = 2.5$. Inlet conditions: H_2 stream at $M_{H_2} = 1.0$, $P_{H_2} = 570,000$ Pa, $T_{H_2} = 300$ K; air stream at $M_{air} = 2.75$, $P_{air} = 45,050$ Pa, $T_{air} = 591.14$ K.

Density Contours at Different Equivalence Ratios and Mach Numbers

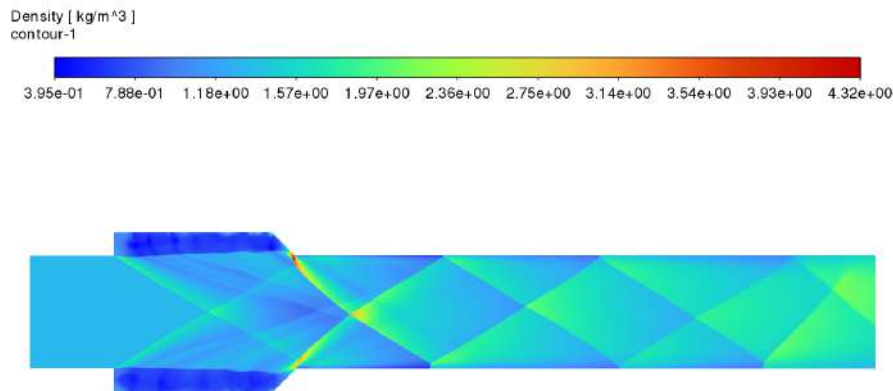


Figure 5.19: Density contour for reacting flow using the global reaction mechanism at $\phi = 0.6$. Inlet conditions: H_2 stream at $M_{H_2} = 1.0$, $P_{H_2} = 228,000$ Pa, $T_{H_2} = 300$ K; air stream at $M_{air} = 2.0$, $P_{air} = 218,538$ Pa, $T_{air} = 825.56$ K.

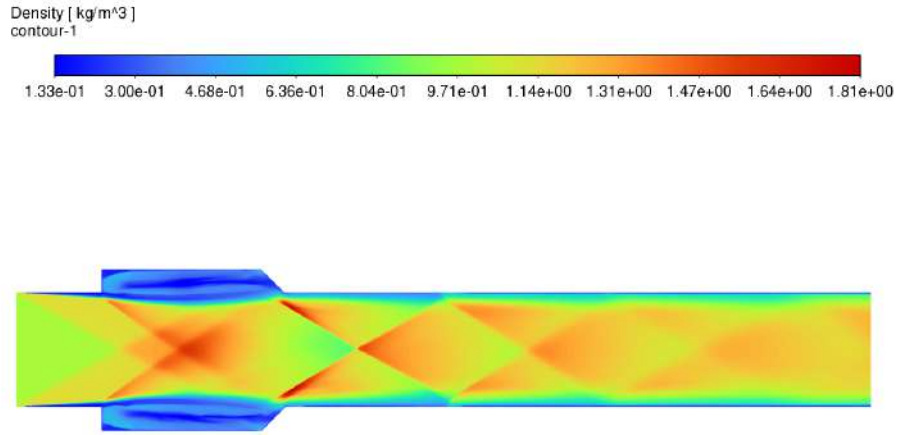


Figure 5.20: Density contour for reacting flow using the global reaction mechanism at $\phi = 1.0$. Inlet conditions: H_2 stream at $M_{H_2} = 1.0$, $P_{H_2} = 228,000$ Pa, $T_{H_2} = 300$ K; air stream at $M_{air} = 2.0$, $P_{air} = 218,538$ Pa, $T_{air} = 825.56$ K.

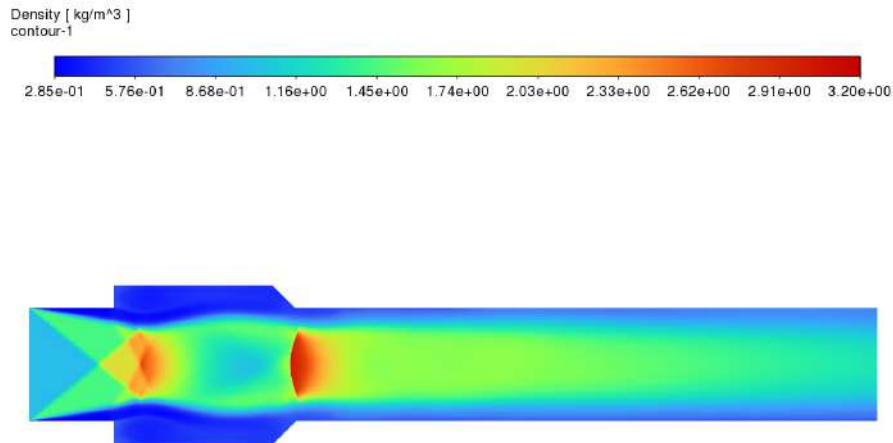


Figure 5.21: Density contour for reacting flow using the detailed reaction mechanism at $\phi = 2.3$. Inlet conditions: H_2 stream at $M_{H_2} = 1.0$, $P_{H_2} = 228,000$ Pa, $T_{H_2} = 300$ K; air stream at $M_{air} = 2.0$, $P_{air} = 218,538$ Pa, $T_{air} = 825.56$ K.

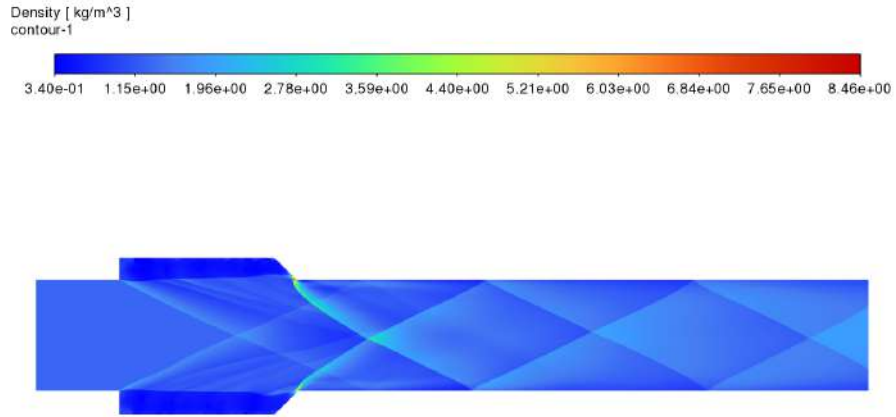


Figure 5.22: Density contour for reacting flow using the global reaction mechanism at $\phi = 0.6$. Inlet conditions: H_2 stream at $M_{H_2} = 1.0$, $P_{H_2} = 570,000$ Pa, $T_{H_2} = 300$ K; air stream at $M_{air} = 2.75$, $P_{air} = 45,050$ Pa, $T_{air} = 591.14$ K.

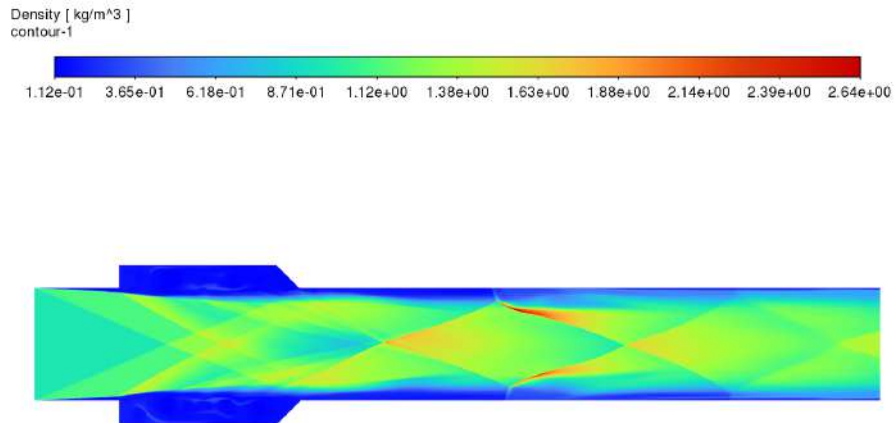


Figure 5.23: Density contour for reacting flow using the global reaction mechanism at $\phi = 1.0$. Inlet conditions: H_2 stream at $M_{H_2} = 1.0$, $P_{H_2} = 570,000$ Pa, $T_{H_2} = 300$ K; air stream at $M_{air} = 2.75$, $P_{air} = 45,050$ Pa, $T_{air} = 591.14$ K.

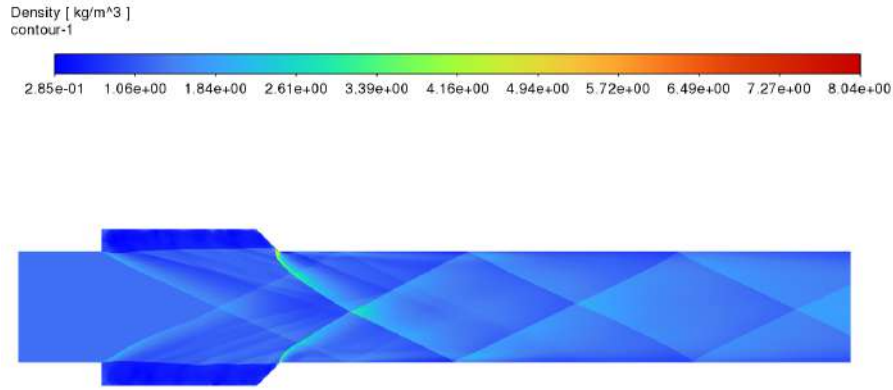


Figure 5.24: Density contour for reacting flow using the global reaction mechanism at $\phi = 2.3$. Inlet conditions: H_2 stream at $M_{H_2} = 1.0$, $P_{H_2} = 570,000$ Pa, $T_{H_2} = 300$ K; air stream at $M_{air} = 2.75$, $P_{air} = 45,050$ Pa, $T_{air} = 591.14$ K.

Enthalpy Contours at Different Equivalence Ratios and Mach Numbers

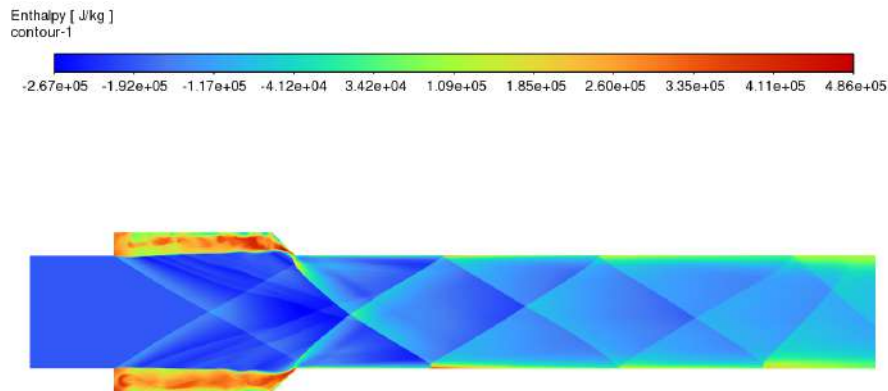


Figure 5.25: Enthalpy contour for reacting flow using the global reaction mechanism at $\phi = 0.6$. Inlet conditions: H_2 stream at $M_{H_2} = 1.0$, $P_{H_2} = 228,000$ Pa, $T_{H_2} = 300$ K; air stream at $M_{air} = 2.0$, $P_{air} = 218,538$ Pa, $T_{air} = 825.56$ K.

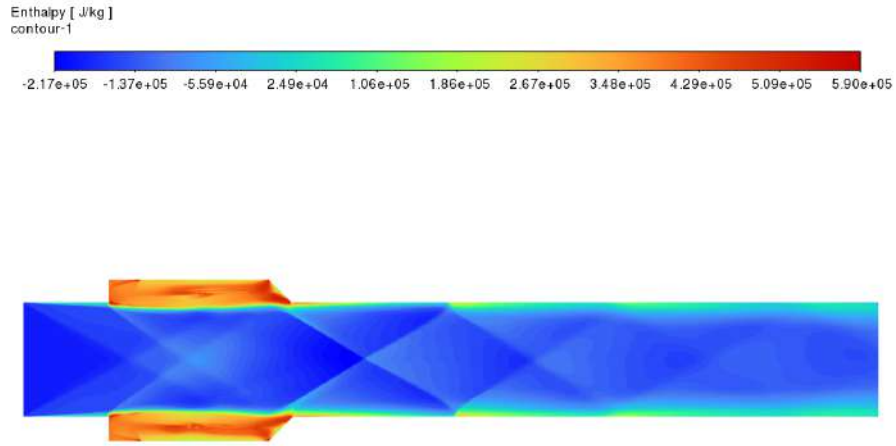


Figure 5.26: Enthalpy contour for reacting flow using the global reaction mechanism at $\phi = 1.0$. Inlet conditions: H_2 stream at $M_{H_2} = 1.0$, $P_{H_2} = 228,000$ Pa, $T_{H_2} = 300$ K; air stream at $M_{air} = 2.0$, $P_{air} = 218,538$ Pa, $T_{air} = 825.56$ K.

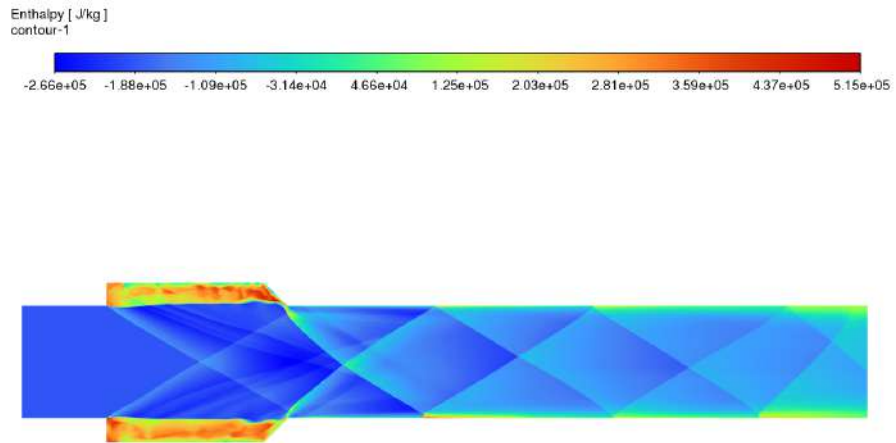


Figure 5.27: Enthalpy contour for reacting flow using the global reaction mechanism at $\phi = 2.3$. Inlet conditions: H_2 stream at $M_{H_2} = 1.0$, $P_{H_2} = 228,000$ Pa, $T_{H_2} = 300$ K; air stream at $M_{air} = 2.0$, $P_{air} = 218,538$ Pa, $T_{air} = 825.56$ K.

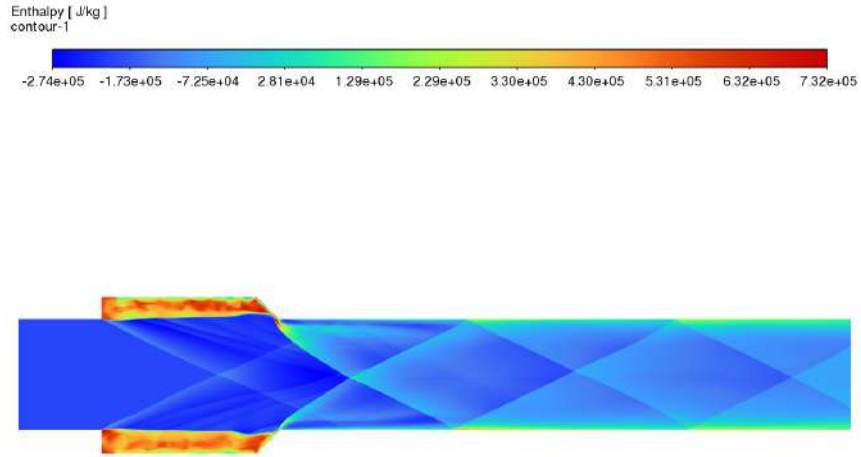


Figure 5.28: Enthalpy contour for reacting flow using the global reaction mechanism at $\phi = 0.6$. Inlet conditions: H_2 stream at $M_{H_2} = 1.0$, $P_{H_2} = 570,000$ Pa, $T_{H_2} = 300$ K; air stream at $M_{air} = 2.75$, $P_{air} = 45,050$ Pa, $T_{air} = 591.14$ K.

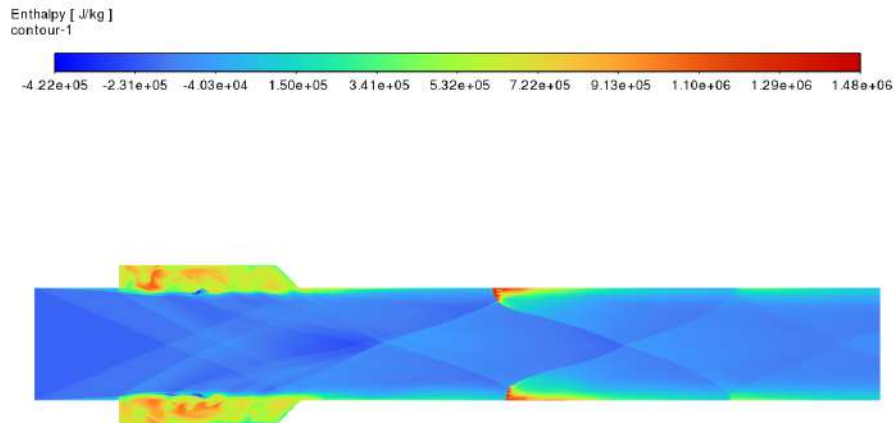


Figure 5.29: Enthalpy contour for reacting flow using the global reaction mechanism at $\phi = 1.0$. Inlet conditions: H_2 stream at $M_{H_2} = 1.0$, $P_{H_2} = 570,000$ Pa, $T_{H_2} = 300$ K; air stream at $M_{air} = 2.75$, $P_{air} = 45,050$ Pa, $T_{air} = 591.14$ K.

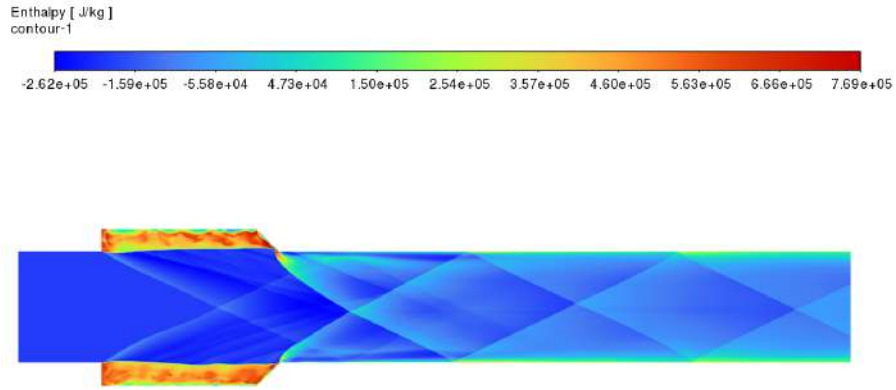


Figure 5.30: Enthalpy contour for reacting flow using the global reaction mechanism at $\phi = 2.3$. Inlet conditions: H_2 stream at $M_{H_2} = 1.0$, $P_{H_2} = 570,000$ Pa, $T_{H_2} = 300$ K; air stream at $M_{air} = 2.75$, $P_{air} = 45,050$ Pa, $T_{air} = 591.14$ K.

Hydrogen mass fraction Contours at Different Equivalence Ratios and Mach Numbers

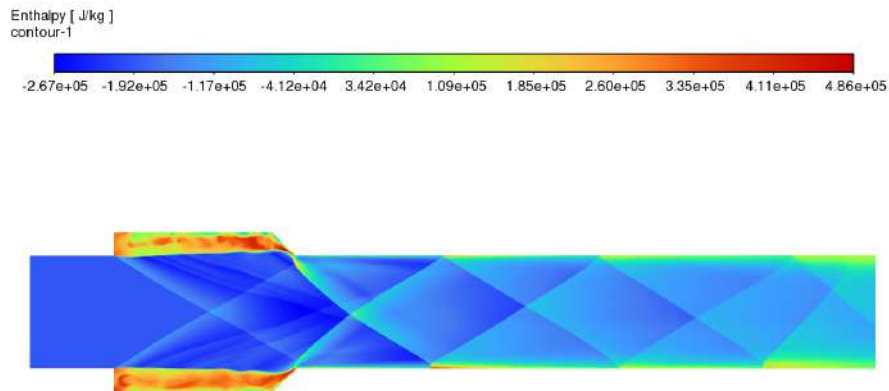


Figure 5.31: Enthalpy contour for reacting flow using the global reaction mechanism at $\phi = 0.6$. Inlet conditions: H_2 stream at $M_{H_2} = 1.0$, $P_{H_2} = 228,000$ Pa, $T_{H_2} = 300$ K; air stream at $M_{air} = 2.0$, $P_{air} = 218,538$ Pa, $T_{air} = 825.56$ K.

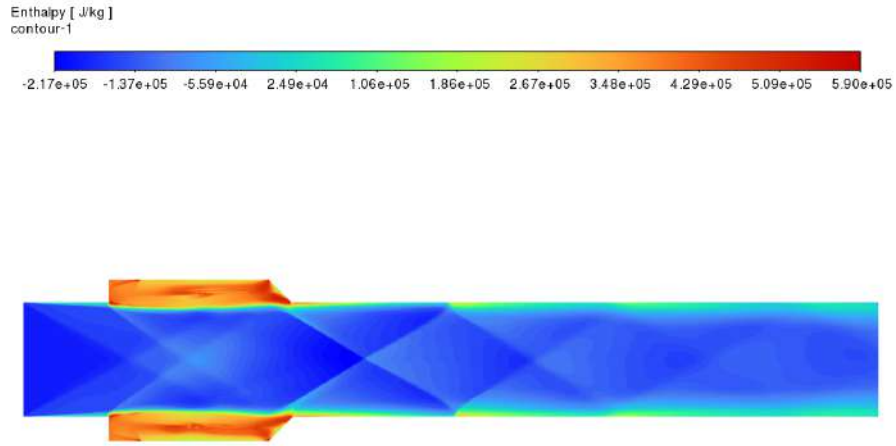


Figure 5.32: Enthalpy contour for reacting flow using the global reaction mechanism at $\phi = 1.0$. Inlet conditions: H_2 stream at $M_{H_2} = 1.0$, $P_{H_2} = 228,000$ Pa, $T_{H_2} = 300$ K; air stream at $M_{air} = 2.0$, $P_{air} = 218,538$ Pa, $T_{air} = 825.56$ K.

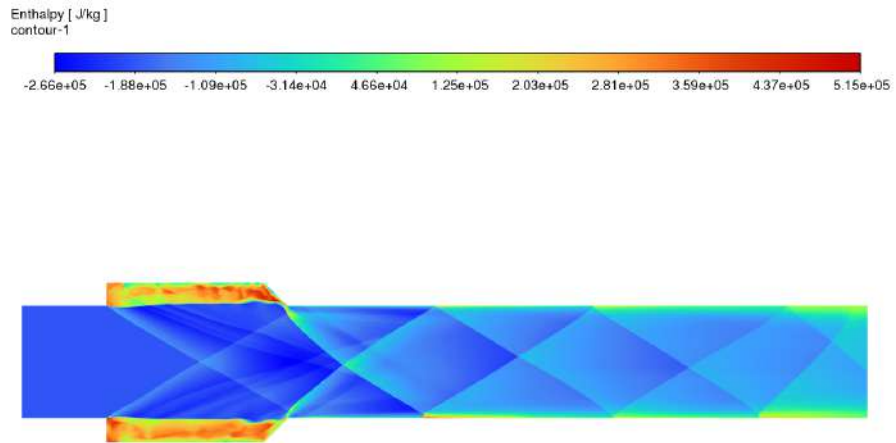


Figure 5.33: Enthalpy contour for reacting flow using the global reaction mechanism at $\phi = 2.3$. Inlet conditions: H_2 stream at $M_{H_2} = 1.0$, $P_{H_2} = 228,000$ Pa, $T_{H_2} = 300$ K; air stream at $M_{air} = 2.0$, $P_{air} = 218,538$ Pa, $T_{air} = 825.56$ K.

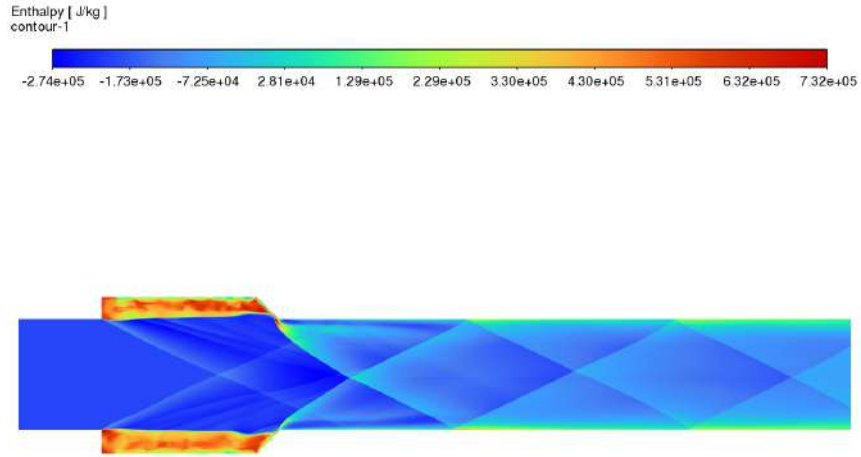


Figure 5.34: Enthalpy contour for reacting flow using the global reaction mechanism at $\phi = 0.6$. Inlet conditions: H_2 stream at $M_{H_2} = 1.0$, $P_{H_2} = 570,000$ Pa, $T_{H_2} = 300$ K; air stream at $M_{air} = 2.75$, $P_{air} = 45,050$ Pa, $T_{air} = 591.14$ K.

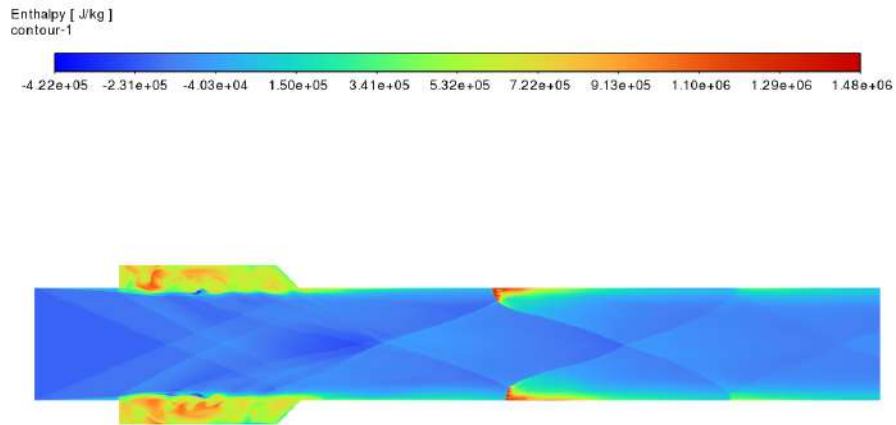


Figure 5.35: Enthalpy contour for reacting flow using the global reaction mechanism at $\phi = 1.0$. Inlet conditions: H_2 stream at $M_{H_2} = 1.0$, $P_{H_2} = 570,000$ Pa, $T_{H_2} = 300$ K; air stream at $M_{air} = 2.75$, $P_{air} = 45,050$ Pa, $T_{air} = 591.14$ K.

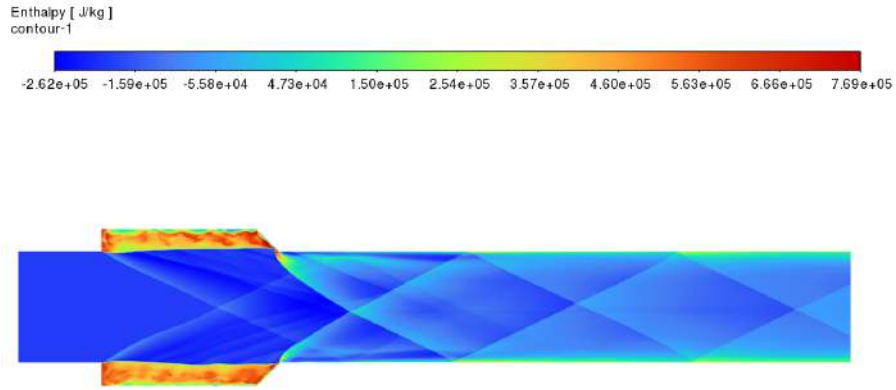


Figure 5.36: Enthalpy contour for reacting flow using the global reaction mechanism at $\phi = 2.3$. Inlet conditions: H_2 stream at $M_{H_2} = 1.0$, $P_{H_2} = 570,000$ Pa, $T_{H_2} = 300$ K; air stream at $M_{air} = 2.75$, $P_{air} = 45,050$ Pa, $T_{air} = 591.14$ K.

Water mass fraction Contours at Different Equivalence Ratios and Mach Numbers (Global Mechanism)

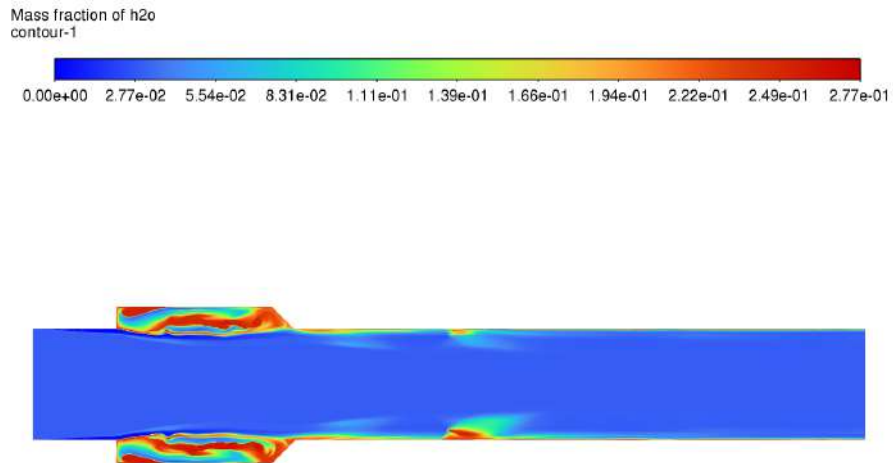


Figure 5.37: Contour of water vapor mass fraction, Y_{H_2O} , for a supersonic global combustion flow case. The inlet conditions are: ϕ of 0.6, hydrogen stream at $M_{H_2} = 0.6$, $P_{H_2} = 110$ kPa, $T_{H_2} = 300$ K, with $Y_{H_2} = 0.6$ and $Y_{H_2O} = 0.032$; and air stream at $M_{air} = 2.0$, $P_{air} = 41,647$ Pa, $T_{air} = 825.56$ K.

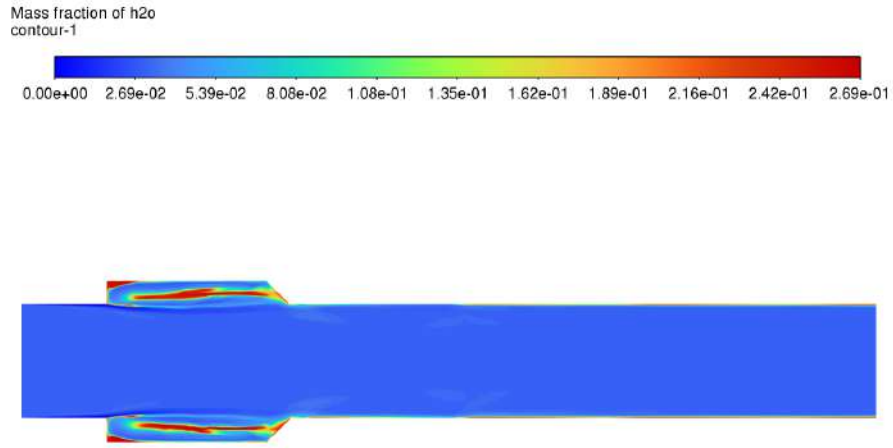


Figure 5.38: Contour of water vapor mass fraction, $Y_{\text{H}_2\text{O}}$, for a supersonic global combustion flow case. The inlet conditions are: ϕ of 1.0, hydrogen stream at $M_{\text{H}_2} = 1.0$, $P_{\text{H}_2} = 110$ kPa, $T_{\text{H}_2} = 300$ K, with $Y_{\text{H}_2} = 1.0$ and $Y_{\text{H}_2\text{O}} = 0.032$; and air stream at $M_{\text{air}} = 2.0$, $P_{\text{air}} = 41,647$ Pa, $T_{\text{air}} = 825.56$ K.

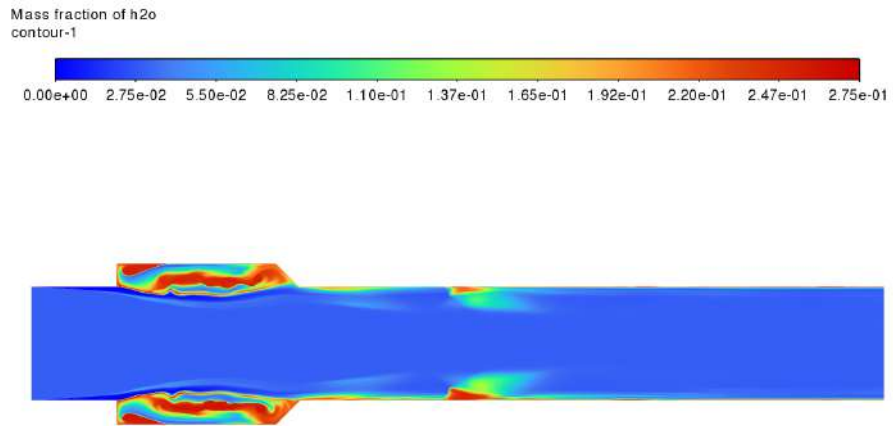


Figure 5.39: Contour of water vapor mass fraction, $Y_{\text{H}_2\text{O}}$, for a supersonic global combustion flow case. The inlet conditions are: ϕ of 2.5, hydrogen stream at $M_{\text{H}_2} = 2.5$, $T_{\text{H}_2} = 300$ K, with $Y_{\text{H}_2} = 2.5$ and $Y_{\text{H}_2\text{O}} = 0.032$; and air stream at $M_{\text{air}} = 2.0$, $P_{\text{air}} = 41,647$ Pa, $T_{\text{air}} = 825.56$ K.

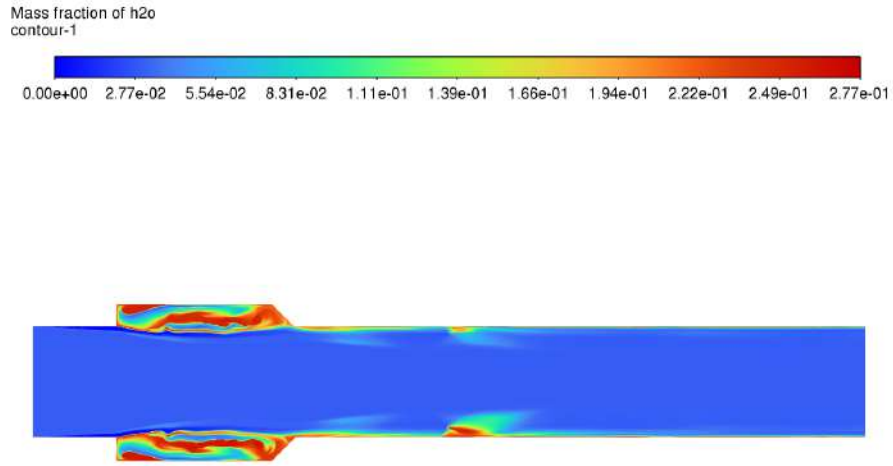


Figure 5.40: H₂O mass fraction contour for reacting flow using the global reaction mechanism at $\phi = 0.6$. Inlet conditions: H₂ stream at $M_{\text{H}_2} = 1.0$, $P_{\text{H}_2} = 570,000$ Pa, $T_{\text{H}_2} = 300$ K; air stream at $M_{\text{air}} = 2.75$, $P_{\text{air}} = 45,050$ Pa, $T_{\text{air}} = 591.14$ K.

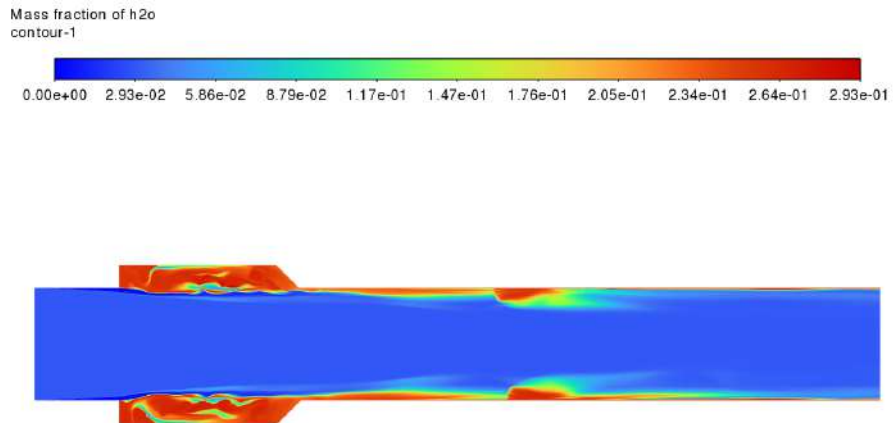


Figure 5.41: H₂O mass fraction contour for reacting flow using the global reaction mechanism at $\phi = 1.0$. Inlet conditions: H₂ stream at $M_{\text{H}_2} = 1.0$, $P_{\text{H}_2} = 570,000$ Pa, $T_{\text{H}_2} = 300$ K; air stream at $M_{\text{air}} = 2.75$, $P_{\text{air}} = 45,050$ Pa, $T_{\text{air}} = 591.14$ K.

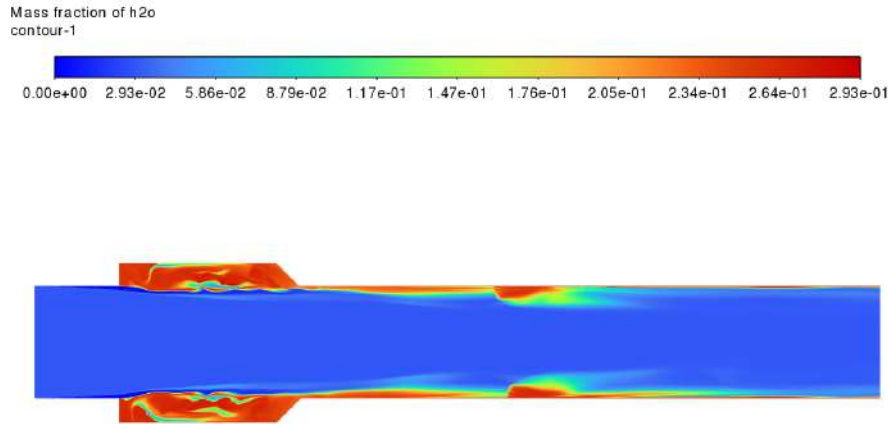


Figure 5.42: H₂O mass fraction contour for reacting flow using the global reaction mechanism at $\phi = 2.3$. Inlet conditions: H₂ stream at $M_{H_2} = 1.0$, $P_{H_2} = 570,000$ Pa, $T_{H_2} = 300$ K; air stream at $M_{air} = 2.75$, $P_{air} = 45,050$ Pa, $T_{air} = 591.14$ K.

5.3 Detailed Mechanism Reaction

This section presents the simulation results derived from the implementation of a reduced detailed chemical mechanism for hydrogen-air combustion. The analysis includes both qualitative and quantitative comparisons with the global model results to highlight key differences in flame behavior, species distribution, and combustion efficiency. Default hydrogen mechanism Mach number may suggest:

- Less chemical energy release or lower heat addition (typical of simplified models).
- A default mechanism not accounting for intermediate radicals, leading to faster flame travel and more complete combustion early on.

More diffused structures in the default hydrogen result from:

- Detailed chemistry (like LLNL or Burke) causing **slower flame speeds, broader reaction zones, and delayed energy release**.
- More realistic modeling of intermediate reactions and temperature rise, spreading the flow acceleration over a larger region.

[30]

5.3.1 Role of the CHEMKIN-Imported Mechanism:

To improve the fidelity of thrust prediction, a detailed chemical kinetics mechanism was imported via the CHEMKIN format. This allows the solver to incorporate a realistic multi-species reaction model with accurate thermophysical properties. Key advantages include:

- Enhanced accuracy in predicting combustion heat release and species evolution.
- Improved estimation of local temperature and pressure fields critical to thrust calculation.
- Better modeling of dissociation and recombination processes, particularly relevant at higher Mach numbers where temperatures are elevated.

Overall, incorporating the CHEMKIN-imported model ensures that thrust estimates are grounded in physically meaningful reaction kinetics rather than simplified assumptions as to be later observed in this chapter. Combined with high Mach inlet conditions, it enables a more realistic and robust assessment of propulsion performance in the combustor.

5.3.2 Discussion of the Detailed hydrogen combustion key contours and flow structure

Comment on Temperature Contours at Different Equivalence Ratios and air inlet Mach Numbers

The temperature fields, figure 5.43 to figure 5.48, generated using the detailed hydrogen–air reaction mechanism exhibit more resolved and structured combustion zones compared to global models. High temperatures are localized around regions of strong recirculation and flame anchoring, particularly within and downstream of the second cavity. At lean conditions ($\varphi = 0.6$), the temperature remains lower due to incomplete combustion. Stoichiometric and rich mixtures ($\varphi = 1.0$ and $\varphi = 2.3$) result in stronger heat release and wider flame spread. The detailed mechanism captures intermediate species and minor reaction pathways, producing smoother gradients and more accurate peak temperature locations, especially at higher Mach number ($M = 2.75$), where shear-layer interactions are more intense.

Comment on Pressure Contours at Different Equivalence Ratios and air inlet Mach Numbers

The pressure contours, figure 5.49 to figure 5.54, with the detailed mechanism show complex shock systems interacting with combustion zones. Unlike the global model, these contours capture subtle pressure variations resulting from localized heat addition and species transport.

At Mach 2.0, moderate pressure buildup occurs near cavity zones. At Mach 2.75, higher pre-combustion momentum and thinner boundary layers cause stronger shock compression, leading to steep pressure gradients near cavity lips and ramp walls. Richer mixtures show stronger combustion-induced pressure rise, with sharper transitions across combustion fronts.

Comment on Density Contours at Different Equivalence Ratios and air inlet Mach Numbers

The density contours, figure 5.55 to figure 5.60, detailed reaction mechanism results sharper density gradients than global, especially across flame fronts and post-combustion expansion regions. At $\varphi = 0.6$, the density reduction is mild due to limited heat release, whereas the $\varphi = 1.0$ and $\varphi = 2.3$ cases show substantial drops in density across active combustion zones.

Comment on Mach Number Contours at Different Equivalence Ratios and air inlet Mach Numbers

The Mach number, figure 5.61 to figure 5.66, distributions reflect the influence of combustion-induced expansion and shock interactions. With the detailed mechanism, local accelerations and decelerations caused by heat release and recombination reactions are more distinctly resolved.

At Mach 2.0, supersonic core flow slows down significantly in reacting zones, while at Mach 2.75, flow choking is observed near cavity regions due to stronger thermal expansion. Richer mixtures cause more pronounced decreases in Mach number downstream of injection due to higher energy release.

Comment on Enthalpy Contours at Different Equivalence Ratios and air inlet Mach Numbers

The enthalpy fields, figure 5.67 to figure 5.72, indicate the effectiveness of combustion in converting chemical energy to thermal energy. With detailed chemistry, energy release is more gradual and distributed, leading to broader regions of elevated enthalpy.

Higher equivalence ratios, especially at Mach 2.75, show significant enthalpy increases throughout the cavity region and beyond. The detailed mechanism captures recombination and minor species effects, leading to more realistic enthalpy distribution compared to global chemistry.

Hydrogen Mass Fraction Contours at Different Equivalence Ratios and Air Inlet Mach Numbers

The hydrogen mass fraction contours, figure 5.73 to figure 5.78, are directly extracted from detailed simulations, showing progressive H_2 depletion with increasing φ and Mach number. Combustion is incomplete at $\varphi = 0.6$, while near-total consumption occurs at $\varphi = 1.0$. Rich cases highlight residual fuel zones, resolved clearly due to the detailed chemistry model.

Water Vapor Mass Fraction Contours at Different Equivalence Ratios and Air Inlet Mach Numbers

The Y_{H_2O} contours, figure 5.79 to figure 5.84, are generated from the current detailed chemistry simulations, capturing finer gradients and higher production near active flame zones and cavity recirculation regions.

5.3.3 Visualisation of key contours and flow structure in detailed hydrogen mechanism combustion

Temperature Contours at Different Equivalence Ratios and air inlet Mach Numbers

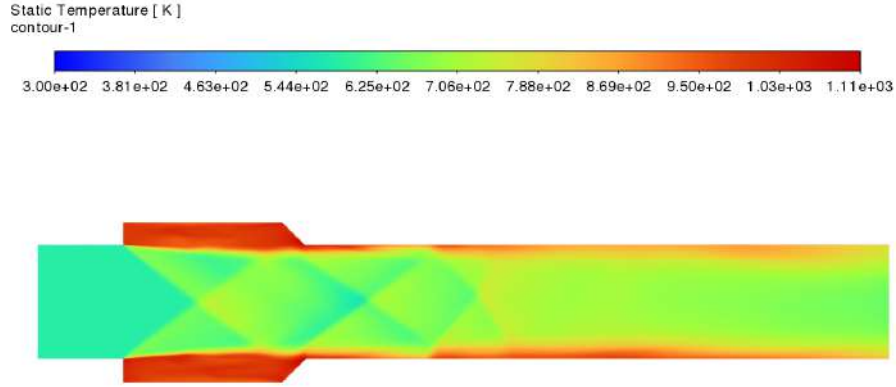


Figure 5.43: Temperature contour for reacting flow using the **detailed reaction mechanism** at $\phi = 0.6$. Inlet conditions: H_2 stream at $M_{\text{H}_2} = 1.0$, $P_{\text{H}_2} = 570,000$ Pa, $T_{\text{H}_2} = 300$ K; air stream at $M_{\text{air}} = 2.0$, $P_{\text{air}} = 218,538$ Pa, $T_{\text{air}} = 825.56$ K.

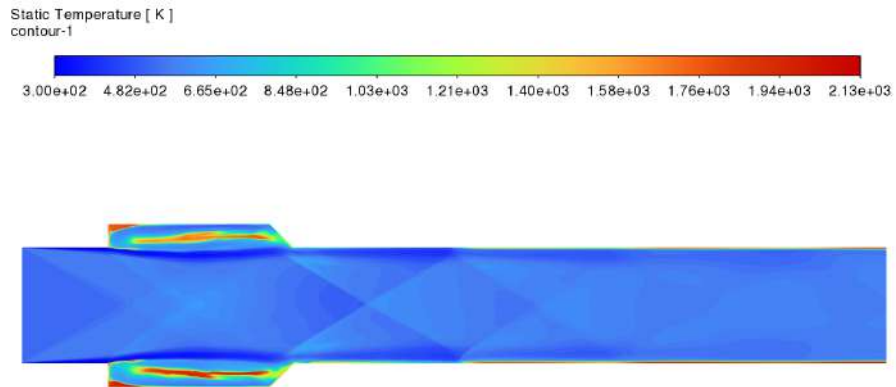


Figure 5.44: Temperature contour for reacting flow using the **detailed reaction mechanism** at $\phi = 1.0$. Inlet conditions: H_2 stream at $M_{\text{H}_2} = 1.0$, $P_{\text{H}_2} = 570,000$ Pa, $T_{\text{H}_2} = 300$ K; air stream at $M_{\text{air}} = 3.0$, $P_{\text{air}} = 114,027$ Pa, $T_{\text{air}} = 530.71$ K.

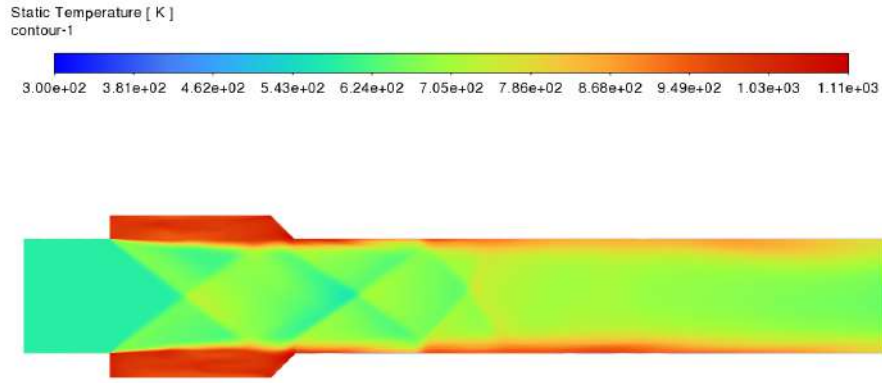


Figure 5.45: Temperature contour for reacting flow using the **detailed reaction mechanism** at $\phi = 2.3$. Inlet conditions: H_2 stream at $M_{\text{H}_2} = 1.0$, $P_{\text{H}_2} = 570,000$ Pa, $T_{\text{H}_2} = 300$ K; air stream at $M_{\text{air}} = 3.0$, $P_{\text{air}} = 114,027$ Pa, $T_{\text{air}} = 530.71$ K.

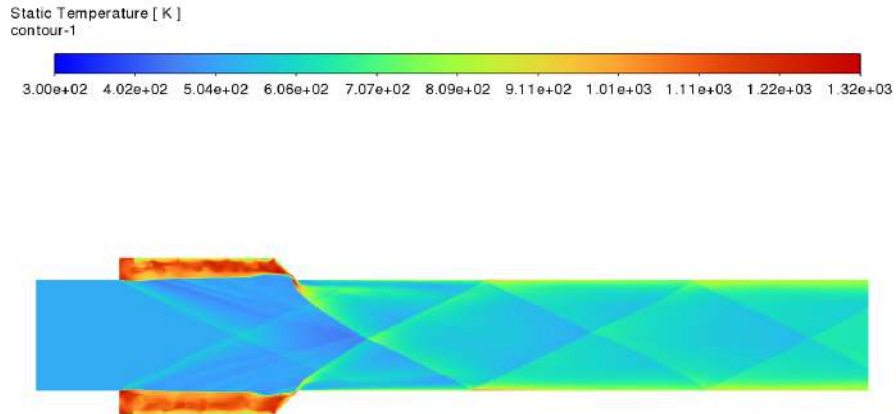


Figure 5.46: Temperature contour for reacting flow using the **detailed reaction mechanism** at $\phi = 0.6$. Inlet conditions: H_2 stream at $M_{\text{H}_2} = 1.0$, $P_{\text{H}_2} = 570,000$ Pa, $T_{\text{H}_2} = 300$ K; air stream at $M_{\text{air}} = 2.75$, $P_{\text{air}} = 146,375$ Pa, $T_{\text{air}} = 591.14$ K.

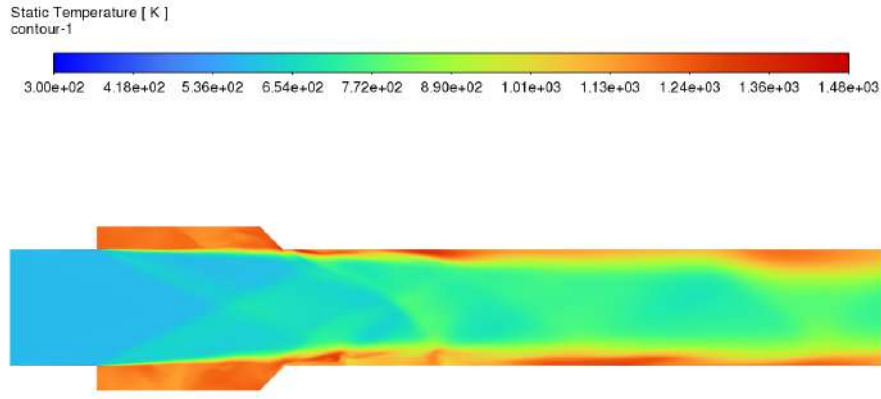


Figure 5.47: Temperature contour for reacting flow using the **detailed reaction mechanism** at $\phi = 1.0$. Inlet conditions: H_2 stream at $M_{H_2} = 1.0$, $P_{H_2} = 570,000$ Pa, $T_{H_2} = 300$ K; air stream at $M_{air} = 2.75$, $P_{air} = 146,375$ Pa, $T_{air} = 591.14$ K.

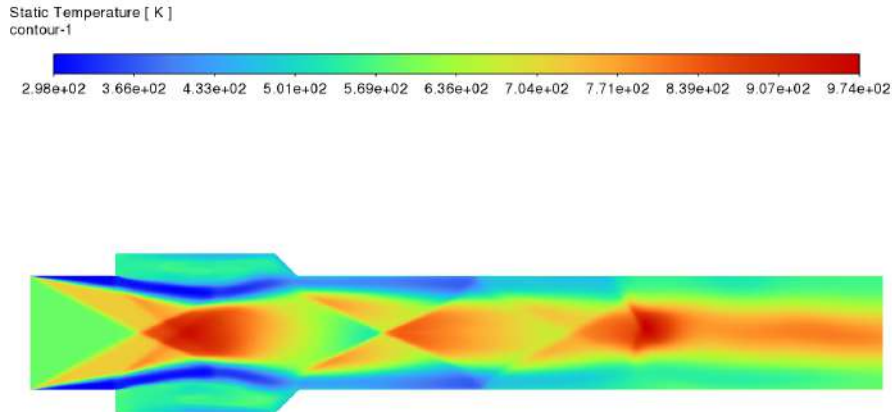


Figure 5.48: Temperature contour for reacting flow using the **detailed reaction mechanism** at $\phi = 2.5$. Inlet conditions: H_2 stream at $M_{H_2} = 1.0$, $P_{H_2} = 570,000$ Pa, $T_{H_2} = 300$ K; air stream at $M_{air} = 2.75$, $P_{air} = 146,375$ Pa, $T_{air} = 591.14$ K.

Pressure Contours at Different Equivalence Ratios and Mach Numbers

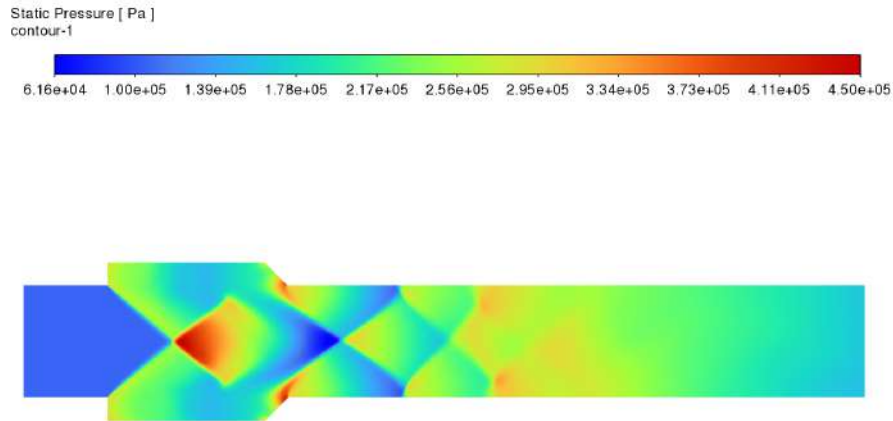


Figure 5.49: Pressure contour for reacting flow using the **detailed reaction mechanism** at $\phi = 0.6$. Inlet conditions: H_2 stream at $M_{\text{H}_2} = 1.0$, $P_{\text{H}_2} = 570,000$ Pa, $T_{\text{H}_2} = 300$ K; air stream at $M_{\text{air}} = 2.0$, $P_{\text{air}} = 218,538$ Pa, $T_{\text{air}} = 825.56$ K.

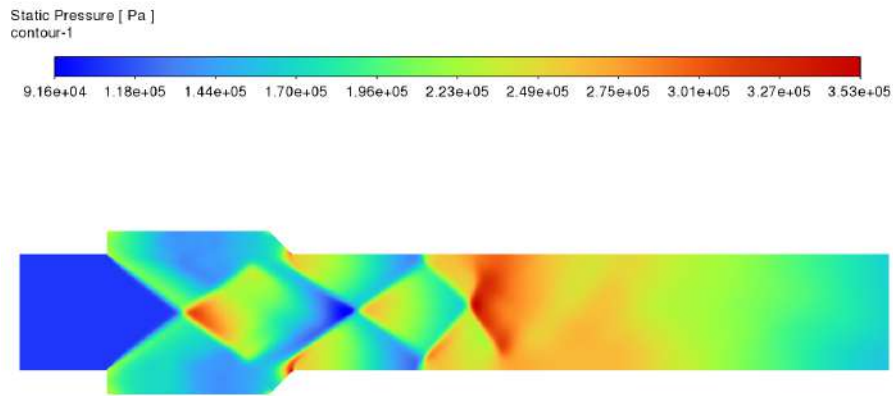


Figure 5.50: Pressure contour for reacting flow using the **detailed reaction mechanism** at $\phi = 1.0$. Inlet conditions: H_2 stream at $M_{\text{H}_2} = 1.0$, $P_{\text{H}_2} = 570,000$ Pa, $T_{\text{H}_2} = 300$ K; air stream at $M_{\text{air}} = 2.0$, $P_{\text{air}} = 218,538$ Pa, $T_{\text{air}} = 825.56$ K.

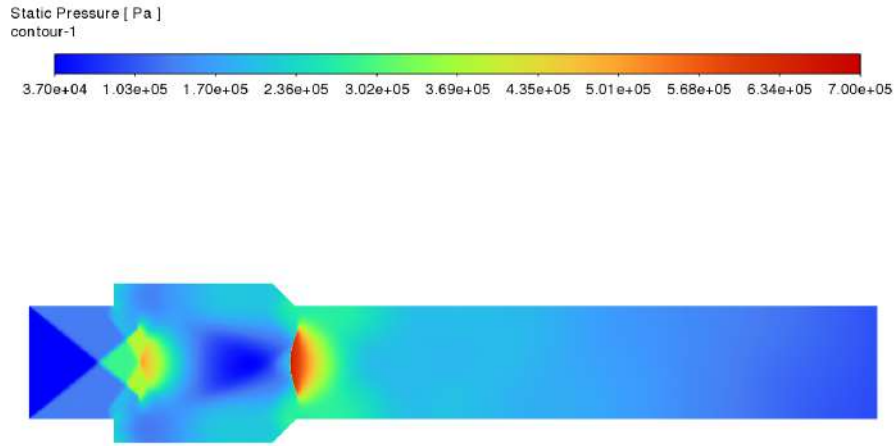


Figure 5.51: Pressure contour for reacting flow using the **detailed reaction mechanism** at $\phi = 2.3$. Inlet conditions: H_2 stream at $M_{H_2} = 1.0$, $P_{H_2} = 570,000$ Pa, $T_{H_2} = 300$ K; air stream at $M_{air} = 2.0$, $P_{air} = 218,538$ Pa, $T_{air} = 825.56$ K.

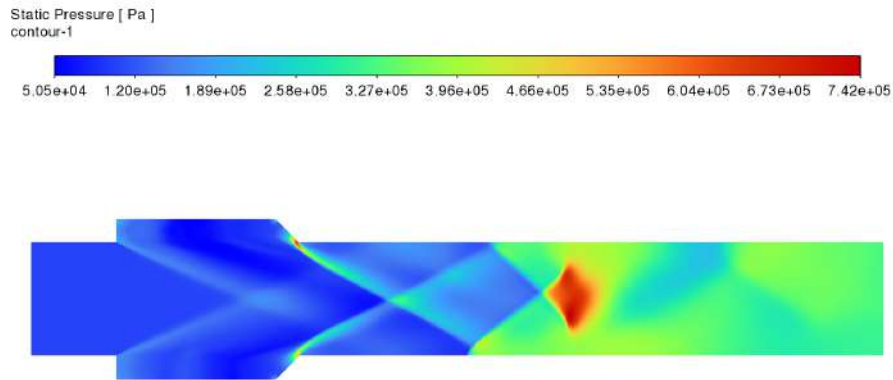


Figure 5.52: Pressure contour for reacting flow using the **detailed reaction mechanism** at $\phi = 0.6$. Inlet conditions: H_2 stream at $M_{H_2} = 1.0$, $P_{H_2} = 570,000$ Pa, $T_{H_2} = 300$ K; air stream at $M_{air} = 2.75$, $P_{air} = 146,375$ Pa, $T_{air} = 591.14$ K.

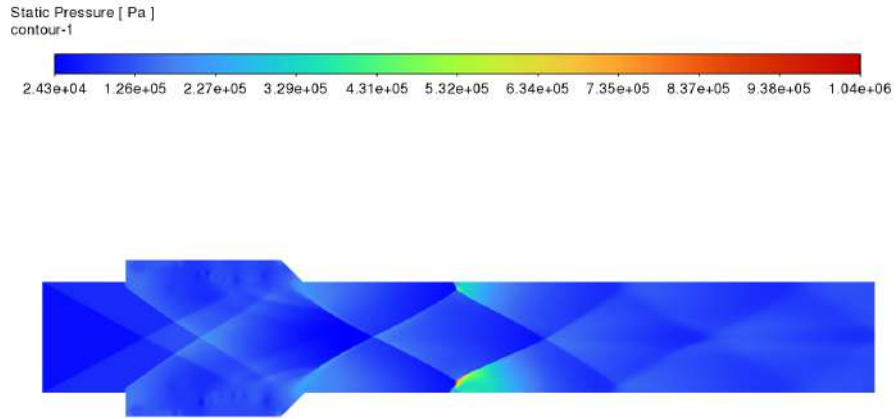


Figure 5.53: Pressure contour for reacting flow using the **detailed reaction mechanism** at $\phi = 1.0$. Inlet conditions: H_2 stream at $M_{H_2} = 1.0$, $P_{H_2} = 570,000$ Pa, $T_{H_2} = 300$ K; air stream at $M_{air} = 2.75$, $P_{air} = 146,375$ Pa, $T_{air} = 591.14$ K.

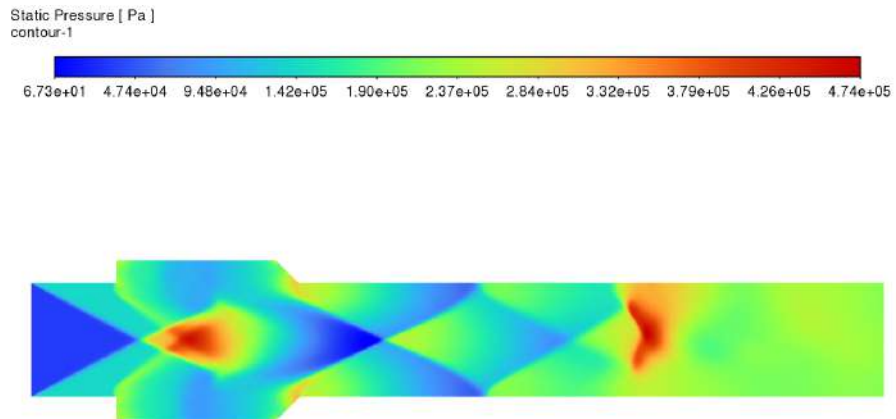


Figure 5.54: Pressure contour for reacting flow using the **detailed reaction mechanism** at $\phi = 2.5$. Inlet conditions: H_2 stream at $M_{H_2} = 1.0$, $P_{H_2} = 570,000$ Pa, $T_{H_2} = 300$ K; air stream at $M_{air} = 2.75$, $P_{air} = 146,375$ Pa, $T_{air} = 591.14$ K.

Density Contours at Different Equivalence Ratios and air inlet Mach Numbers

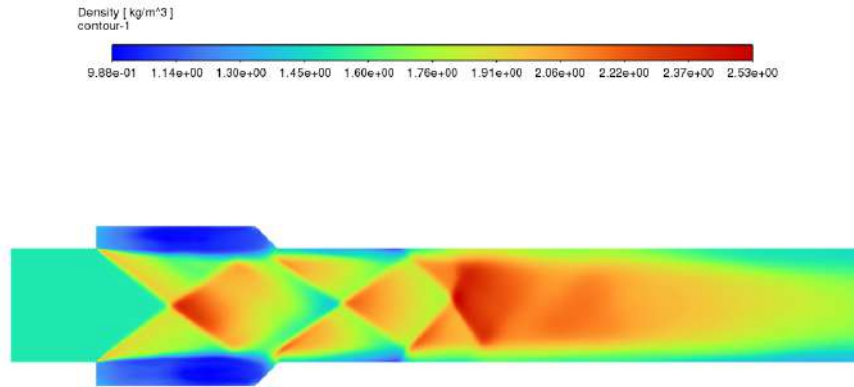


Figure 5.55: Density contour for reacting flow using the **detailed reaction mechanism** at $\phi = 0.6$. Inlet conditions: H_2 stream at $M_{H_2} = 1.0$, $P_{H_2} = 570,000$ Pa, $T_{H_2} = 300$ K; air stream at $M_{air} = 2.0$, $P_{air} = 218,538$ Pa, $T_{air} = 825.56$ K.

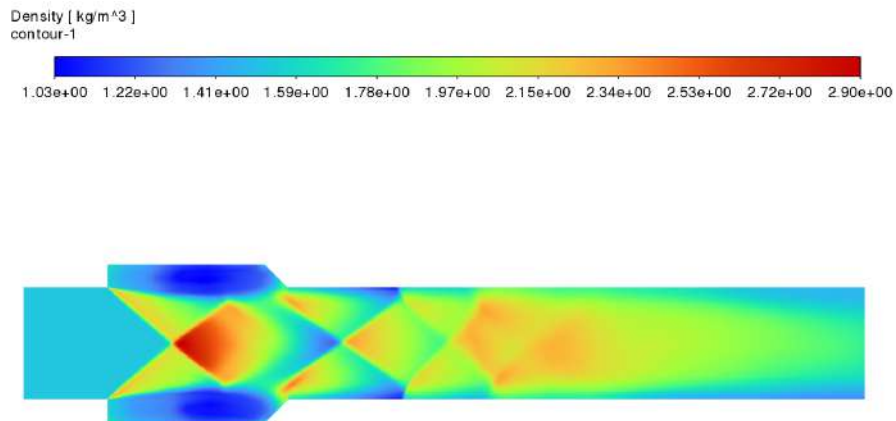


Figure 5.56: Density contour for reacting flow using the **detailed reaction mechanism** at $\phi = 1.0$. Inlet conditions: H_2 stream at $M_{H_2} = 1.0$, $P_{H_2} = 570,000$ Pa, $T_{H_2} = 300$ K; air stream at $M_{air} = 3.0$, $P_{air} = 114,027$ Pa, $T_{air} = 530.71$ K.

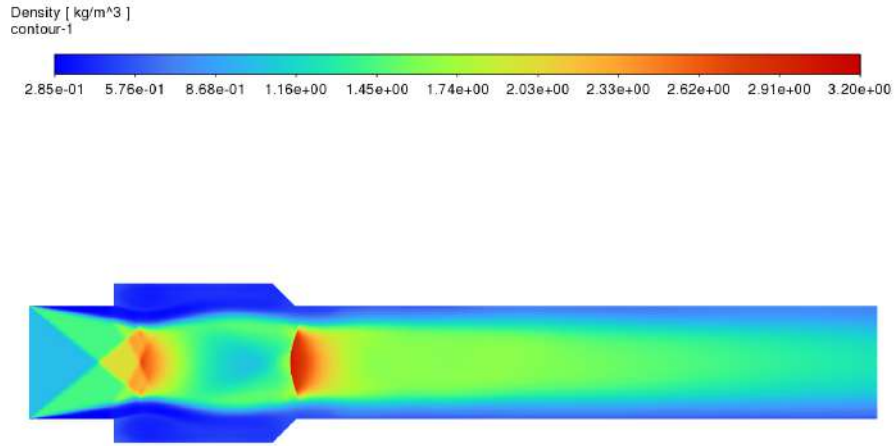


Figure 5.57: Density contour for reacting flow using the **detailed reaction mechanism** at $\phi = 2.3$. Inlet conditions: H_2 stream at $M_{H_2} = 1.0$, $P_{H_2} = 570,000$ Pa, $T_{H_2} = 300$ K; air stream at $M_{air} = 3.0$, $P_{air} = 114,027$ Pa, $T_{air} = 530.71$ K.

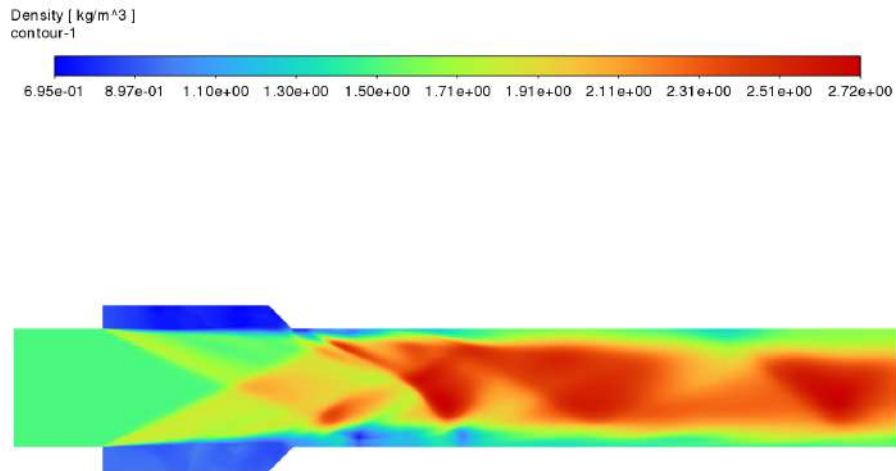


Figure 5.58: Density contour for reacting flow using the **detailed reaction mechanism** at $\phi = 0.6$. Inlet conditions: H_2 stream at $M_{H_2} = 1.0$, $P_{H_2} = 570,000$ Pa, $T_{H_2} = 300$ K; air stream at $M_{air} = 2.75$, $P_{air} = 146,375$ Pa, $T_{air} = 591.14$ K.

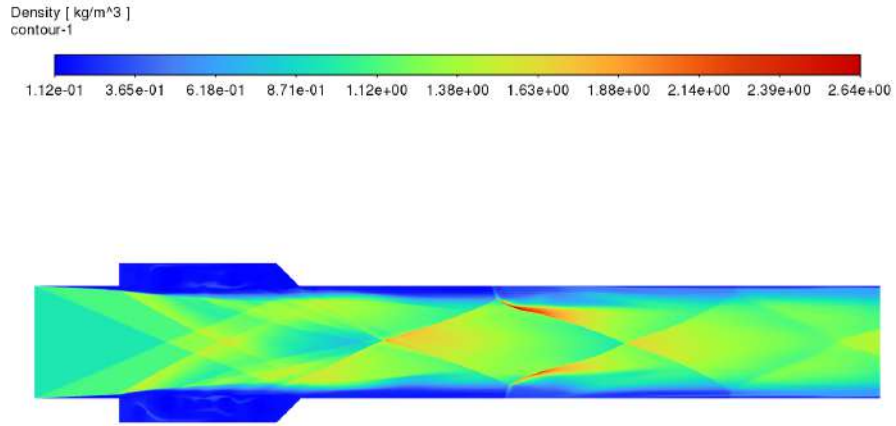


Figure 5.59: Density contour for reacting flow using the **detailed reaction mechanism** at $\phi = 1.0$. Inlet conditions: H_2 stream at $M_{H_2} = 1.0$, $P_{H_2} = 570,000$ Pa, $T_{H_2} = 300$ K; air stream at $M_{air} = 2.75$, $P_{air} = 146,375$ Pa, $T_{air} = 591.14$ K.

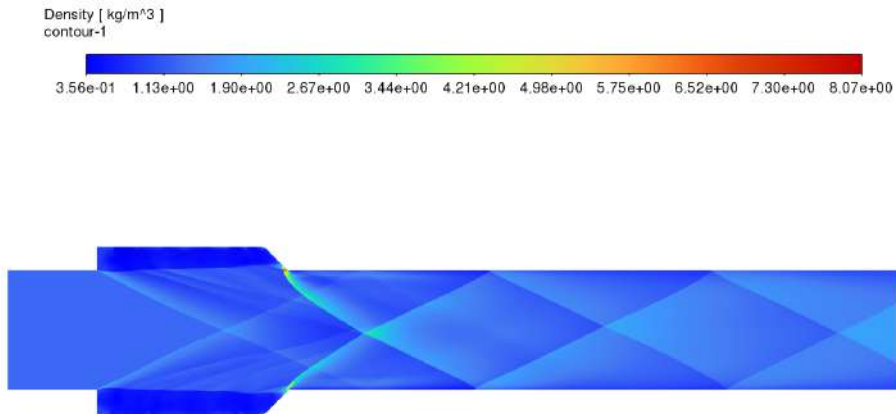


Figure 5.60: Density contour for reacting flow using the **detailed reaction mechanism** at $\phi = 2.5$. Inlet conditions: H_2 stream at $M_{H_2} = 1.0$, $P_{H_2} = 570,000$ Pa, $T_{H_2} = 300$ K; air stream at $M_{air} = 2.75$, $P_{air} = 146,375$ Pa, $T_{air} = 591.14$ K.

Mach number Contours at Different Equivalence Ratios and Mach Numbers

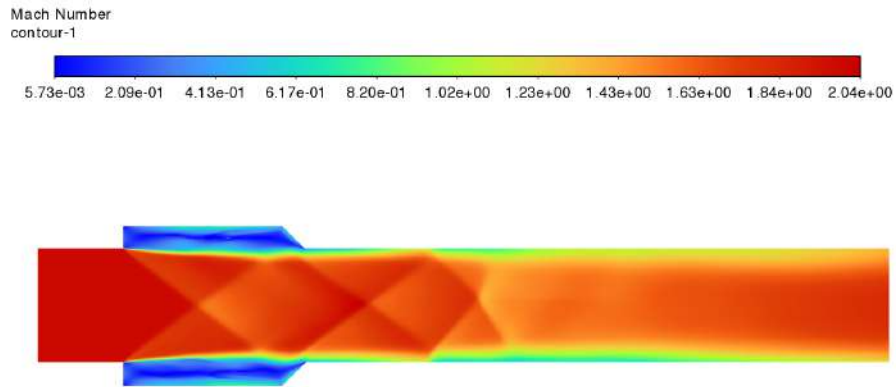


Figure 5.61: Mach number contour for reacting flow using the **detailed reaction mechanism** at $\phi = 0.6$. Inlet conditions: H_2 stream at $M_{H_2} = 1.0$, $P_{H_2} = 570,000$ Pa, $T_{H_2} = 300$ K; air stream at $M_{air} = 2.0$, $P_{air} = 218,538$ Pa, $T_{air} = 825.56$ K.

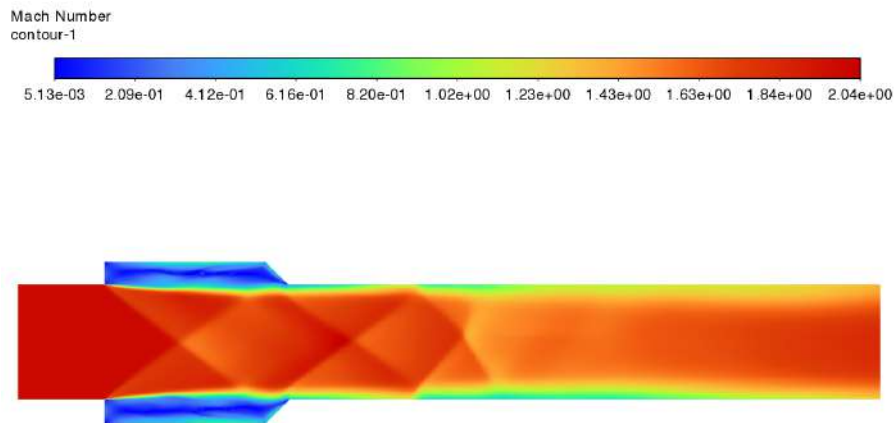


Figure 5.62: Mach number contour for reacting flow using the **detailed reaction mechanism** at $\phi = 1.0$. Inlet conditions: H_2 stream at $M_{H_2} = 1.0$, $P_{H_2} = 570,000$ Pa, $T_{H_2} = 300$ K; air stream at $M_{air} = 2.0$, $P_{air} = 218,538$ Pa, $T_{air} = 825.56$ K.

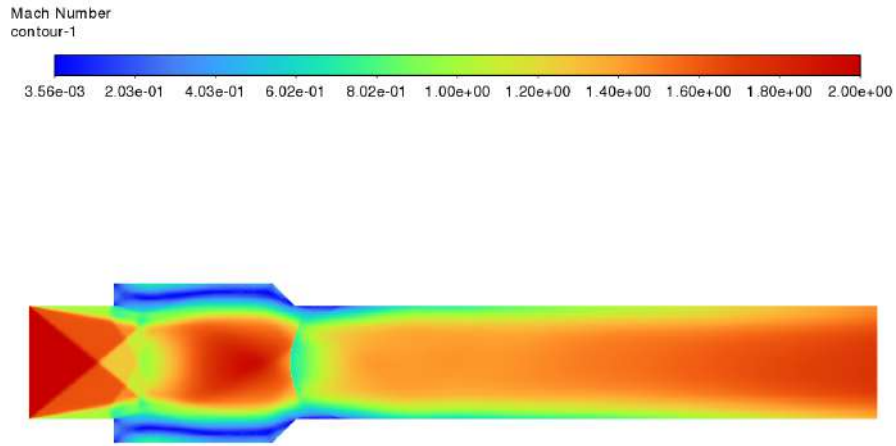


Figure 5.63: Mach number contour for reacting flow using the **detailed reaction mechanism** at $\phi = 2.3$. Inlet conditions: H_2 stream at $M_{\text{H}_2} = 1.0$, $P_{\text{H}_2} = 570,000 \text{ Pa}$, $T_{\text{H}_2} = 300 \text{ K}$; air stream at $M_{\text{air}} = 2.0$, $P_{\text{air}} = 218,538 \text{ Pa}$, $T_{\text{air}} = 825.56 \text{ K}$.

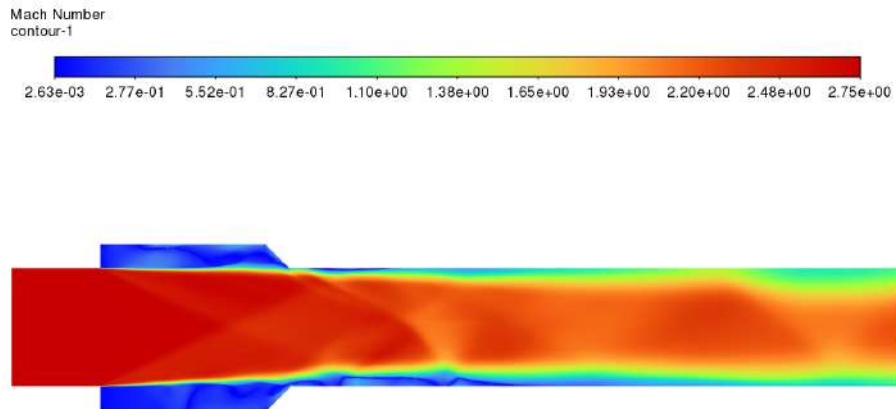


Figure 5.64: Mach number contour for reacting flow using the **detailed reaction mechanism** at $\phi = 0.6$. Inlet conditions: H_2 stream at $M_{\text{H}_2} = 1.0$, $P_{\text{H}_2} = 570,000 \text{ Pa}$, $T_{\text{H}_2} = 300 \text{ K}$; air stream at $M_{\text{air}} = 2.75$, $P_{\text{air}} = 146,375 \text{ Pa}$, $T_{\text{air}} = 591.14 \text{ K}$.

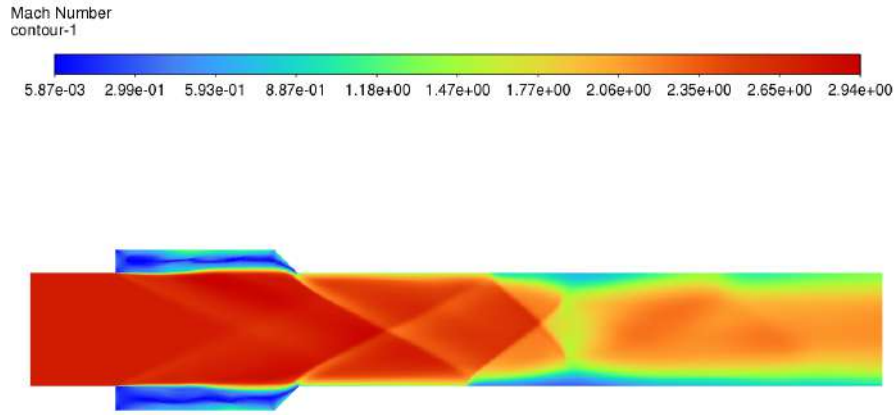


Figure 5.65: Mach number contour for reacting flow using the **detailed reaction mechanism** at $\phi = 1.0$. Inlet conditions: H_2 stream at $M_{H_2} = 1.0$, $P_{H_2} = 570,000$ Pa, $T_{H_2} = 300$ K; air stream at $M_{air} = 2.75$, $P_{air} = 146,375$ Pa, $T_{air} = 591.14$ K.

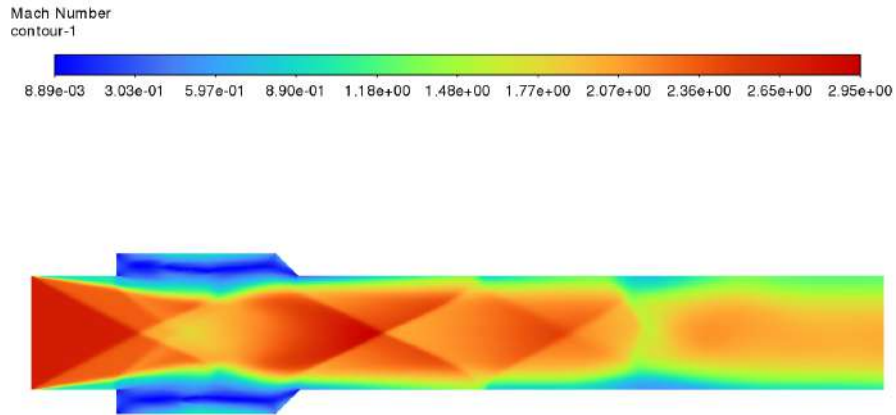


Figure 5.66: Mach number contour for reacting flow using the **detailed reaction mechanism** at $\phi = 2.5$. Inlet conditions: H_2 stream at $M_{H_2} = 1.0$, $P_{H_2} = 570,000$ Pa, $T_{H_2} = 300$ K; air stream at $M_{air} = 2.75$, $P_{air} = 146,375$ Pa, $T_{air} = 591.14$ K.

Enthalpy Contours at Different Equivalence Ratios and Mach Numbers

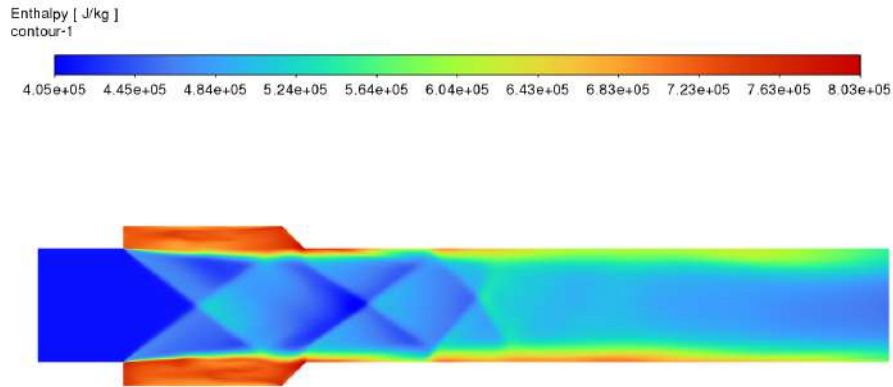


Figure 5.67: Enthalpy contour for reacting flow using the **detailed reaction mechanism** at $\phi = 0.6$. Inlet conditions: H_2 stream at $M_{H_2} = 1.0$, $P_{H_2} = 570,000$ Pa, $T_{H_2} = 300$ K; air stream at $M_{air} = 2.0$, $P_{air} = 218,538$ Pa, $T_{air} = 825.56$ K.

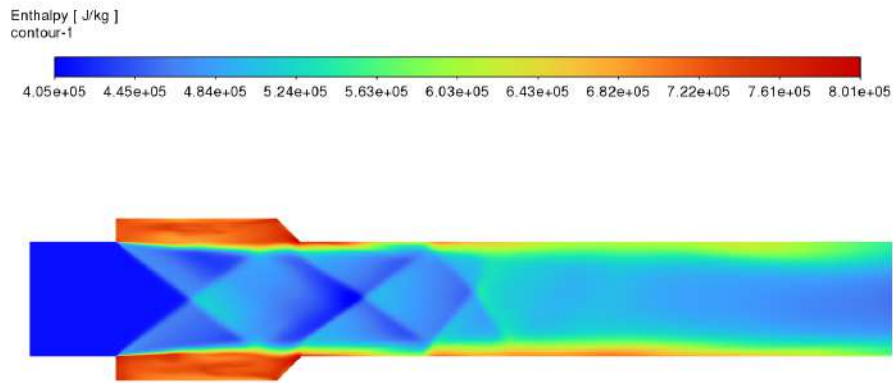


Figure 5.68: Enthalpy contour for reacting flow using the **detailed reaction mechanism** at $\phi = 1.0$. Inlet conditions: H_2 stream at $M_{H_2} = 1.0$, $P_{H_2} = 570,000$ Pa, $T_{H_2} = 300$ K; air stream at $M_{air} = 2.0$, $P_{air} = 218,538$ Pa, $T_{air} = 825.56$ K.

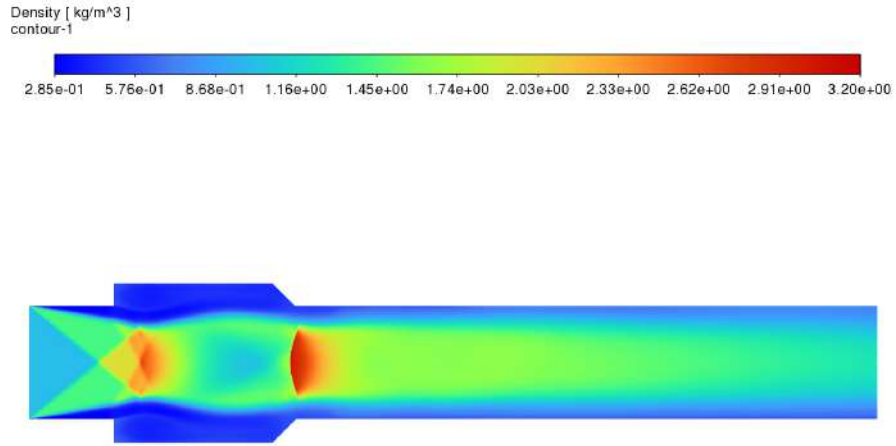


Figure 5.69: Enthalpy contour for reacting flow using the **detailed reaction mechanism** at $\phi = 2.3$. Inlet conditions: H_2 stream at $M_{H_2} = 1.0$, $P_{H_2} = 570,000$ Pa, $T_{H_2} = 300$ K; air stream at $M_{air} = 2.0$, $P_{air} = 218,538$ Pa, $T_{air} = 825.56$ K.

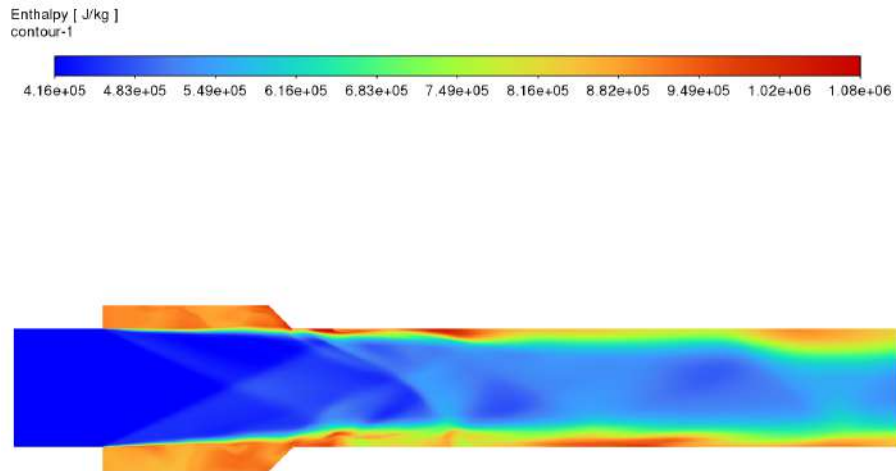


Figure 5.70: Enthalpy contour for reacting flow using the **detailed reaction mechanism** at $\phi = 0.6$. Inlet conditions: H_2 stream at $M_{H_2} = 1.0$, $P_{H_2} = 570,000$ Pa, $T_{H_2} = 300$ K; air stream at $M_{air} = 2.75$, $P_{air} = 146,375$ Pa, $T_{air} = 591.14$ K.

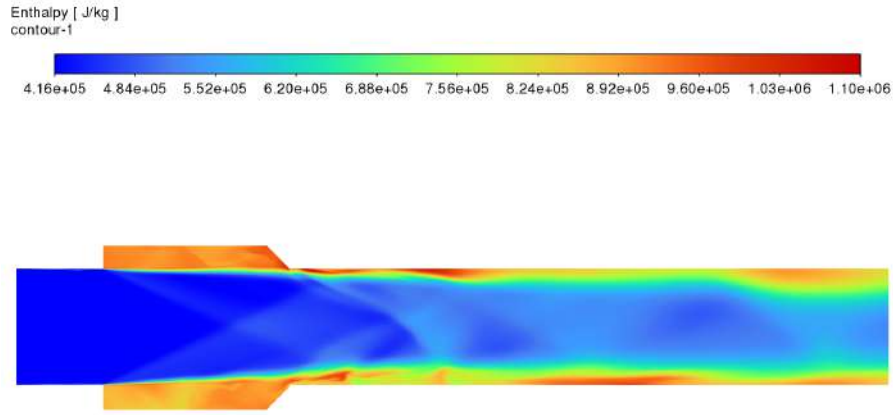


Figure 5.71: Enthalpy contour for reacting flow using the **detailed reaction mechanism** at $\phi = 1.0$. Inlet conditions: H_2 stream at $M_{H_2} = 1.0$, $P_{H_2} = 570,000$ Pa, $T_{H_2} = 300$ K; air stream at $M_{air} = 2.75$, $P_{air} = 146,375$ Pa, $T_{air} = 591.14$ K.

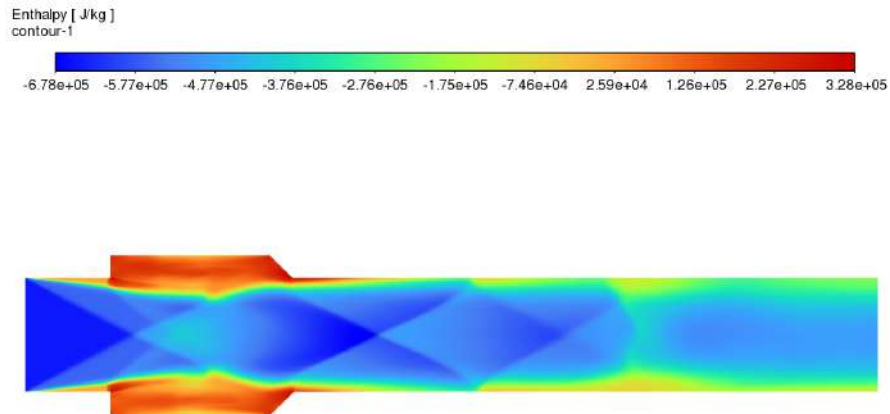


Figure 5.72: Enthalpy contour for reacting flow using the **detailed reaction mechanism** at $\phi = 2.5$. Inlet conditions: H_2 stream at $M_{H_2} = 1.0$, $P_{H_2} = 570,000$ Pa, $T_{H_2} = 300$ K; air stream at $M_{air} = 2.75$, $P_{air} = 146,375$ Pa, $T_{air} = 591.14$ K.

Hydrogen mass fraction Contours at Different Equivalence Ratios and Mach Numbers

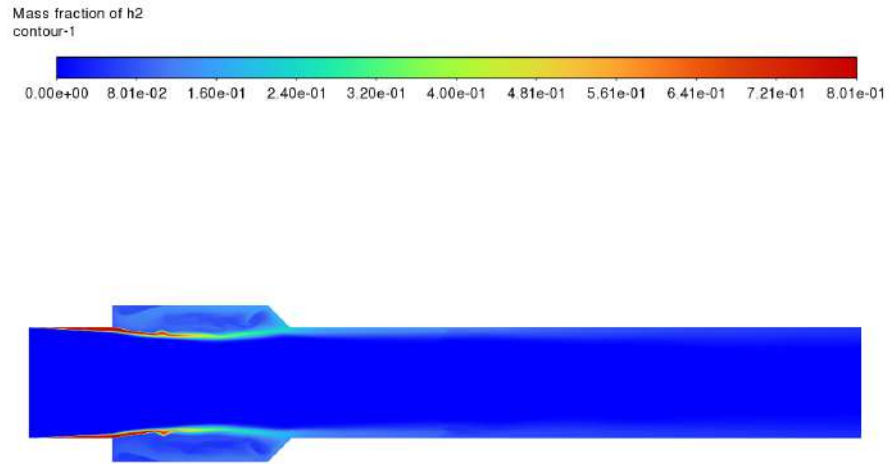


Figure 5.73: Hydrogen mass fraction contour for reacting flow using the **detailed reaction mechanism** at $\phi = 0.6$. Inlet conditions: H_2 stream at $M_{H_2} = 1.0$, $P_{H_2} = 570,000$ Pa, $T_{H_2} = 300$ K; air stream at $M_{air} = 2.0$, $P_{air} = 218,538$ Pa, $T_{air} = 825.56$ K.

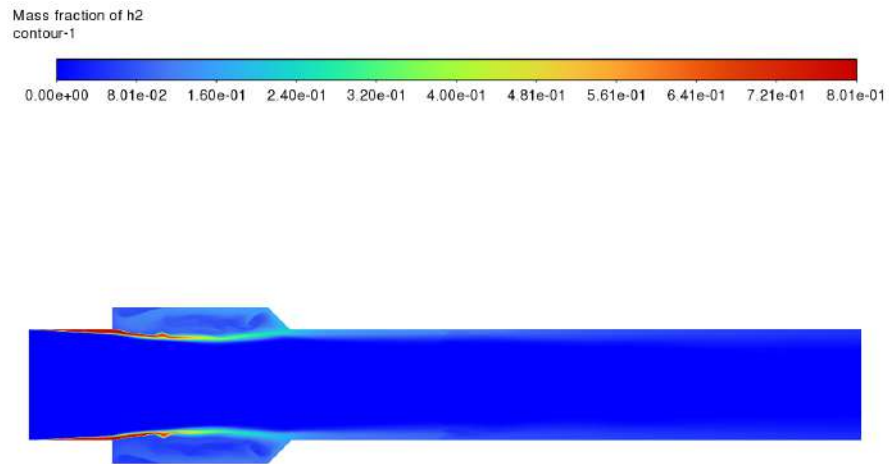


Figure 5.74: Hydrogen mass fraction contour for reacting flow using the **detailed reaction mechanism** at $\phi = 1.0$. Inlet conditions: H_2 stream at $M_{H_2} = 1.0$, $P_{H_2} = 570,000$ Pa, $T_{H_2} = 300$ K; air stream at $M_{air} = 2.0$, $P_{air} = 218,538$ Pa, $T_{air} = 825.56$ K.

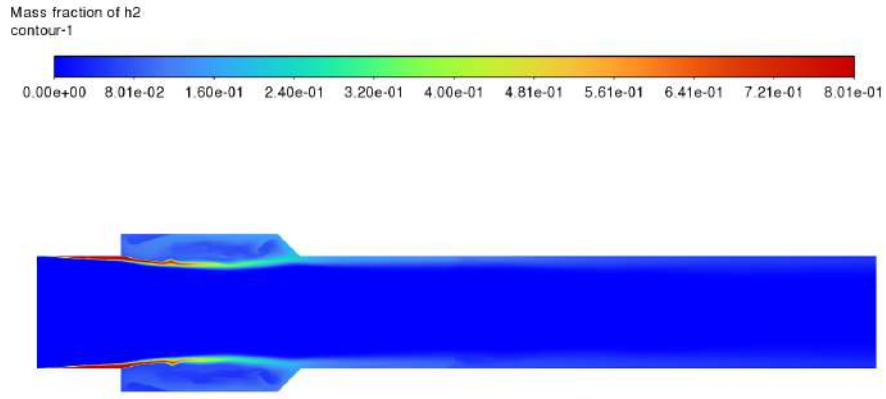


Figure 5.75: Hydrogen mass fraction contour for reacting flow using the **detailed reaction mechanism** at $\phi = 2.3$. Inlet conditions: H_2 stream at $M_{H_2} = 1.0$, $P_{H_2} = 570,000$ Pa, $T_{H_2} = 300$ K; air stream at $M_{air} = 2.0$, $P_{air} = 218,538$ Pa, $T_{air} = 825.56$ K.

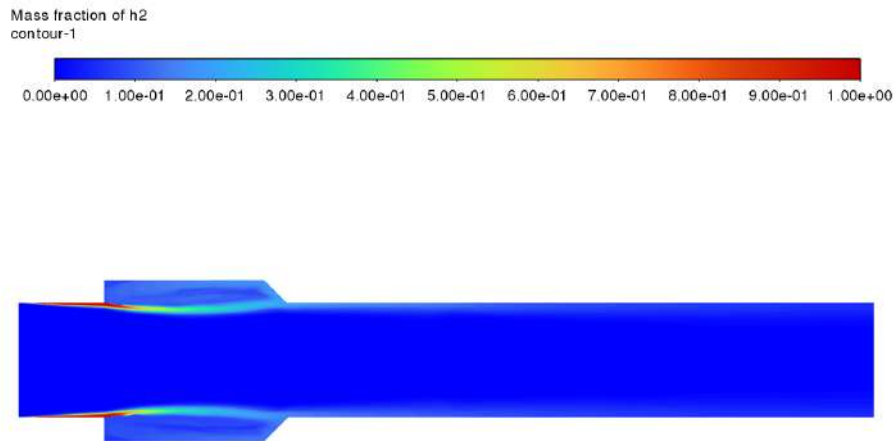


Figure 5.76: Hydrogen mass fraction contour for reacting flow using the **detailed reaction mechanism** at $\phi = 0.6$. Inlet conditions: H_2 stream at $M_{H_2} = 1.0$, $P_{H_2} = 570,000$ Pa, $T_{H_2} = 300$ K; air stream at $M_{air} = 2.75$, $P_{air} = 146,375$ Pa, $T_{air} = 591.14$ K.

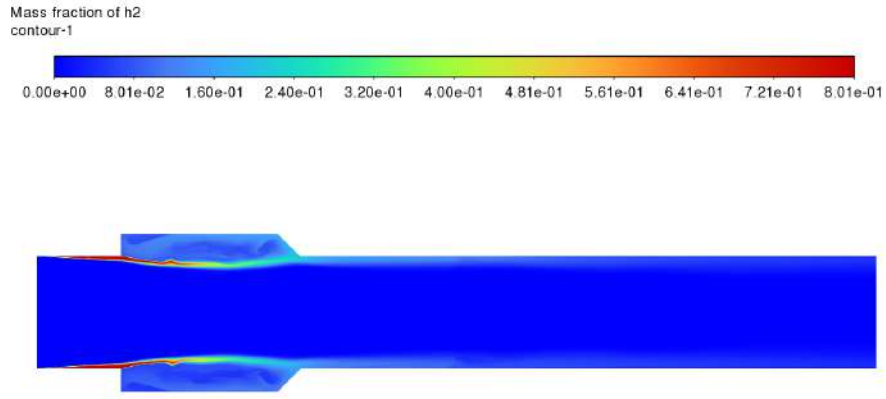


Figure 5.77: Hydrogen mass fraction contour for reacting flow using the **detailed reaction mechanism** at $\phi = 1.0$. Inlet conditions: H_2 stream at $M_{H_2} = 1.0$, $P_{H_2} = 570,000$ Pa, $T_{H_2} = 300$ K; air stream at $M_{air} = 2.75$, $P_{air} = 146,375$ Pa, $T_{air} = 591.14$ K.

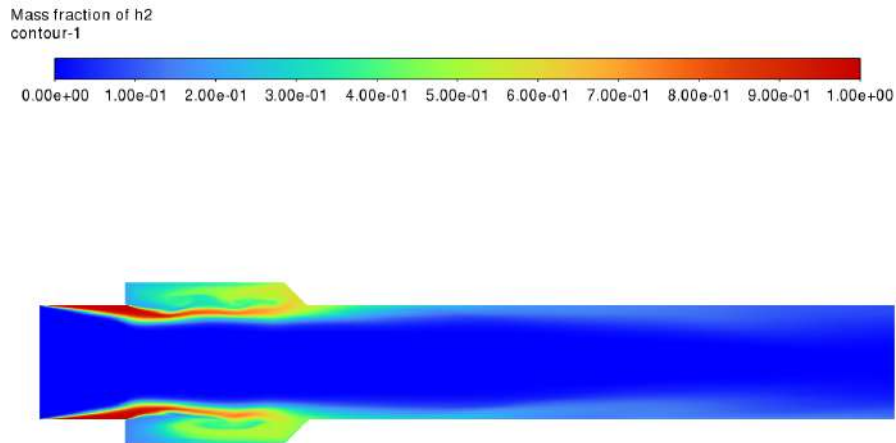


Figure 5.78: Hydrogen mass fraction contour for reacting flow using the **detailed reaction mechanism** at $\phi = 2.5$. Inlet conditions: H_2 stream at $M_{H_2} = 1.0$, $P_{H_2} = 570,000$ Pa, $T_{H_2} = 300$ K; air stream at $M_{air} = 2.75$, $P_{air} = 146,375$ Pa, $T_{air} = 591.14$ K.

Water mass fraction Contours at Different Equivalence Ratios and Mach Numbers

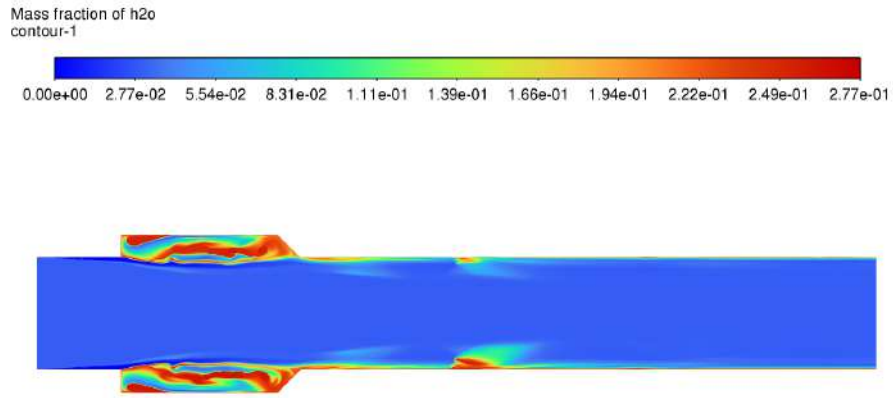


Figure 5.79: H₂O mass fraction contour for reacting flow using the **detailed reaction mechanism** at $\phi = 0.6$. Inlet conditions: H₂ stream at $M_{H_2} = 0.6$, $P_{H_2} = 110$ kPa, $T_{H_2} = 300$ K, with $Y_{H_2} = 1.0$ and $Y_{H_2O} = 0.032$; air stream at $M_{air} = 2.0$, $P_{air} = 41,647$ Pa, $T_{air} = 825.56$ K.

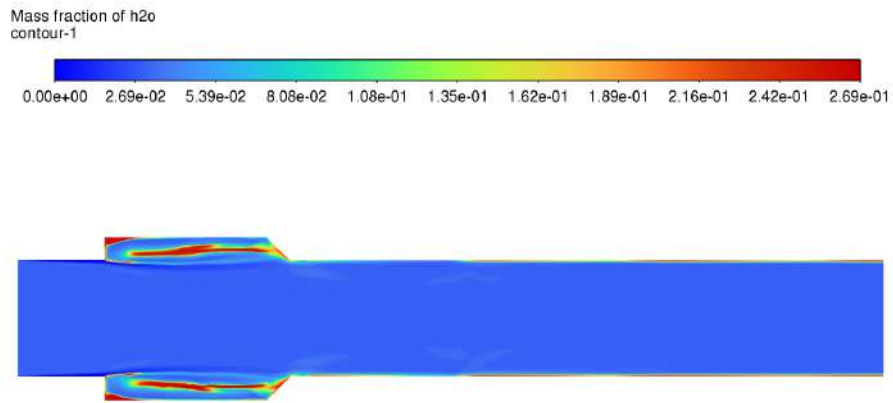


Figure 5.80: H₂O mass fraction contour for reacting flow using the **detailed reaction mechanism** at $\phi = 1.0$. Inlet conditions: H₂ stream at $M_{H_2} = 1.0$, $P_{H_2} = 110$ kPa, $T_{H_2} = 300$ K, with $Y_{H_2} = 1.0$ and $Y_{H_2O} = 0.032$; air stream at $M_{air} = 2.0$, $P_{air} = 41,647$ Pa, $T_{air} = 825.56$ K.

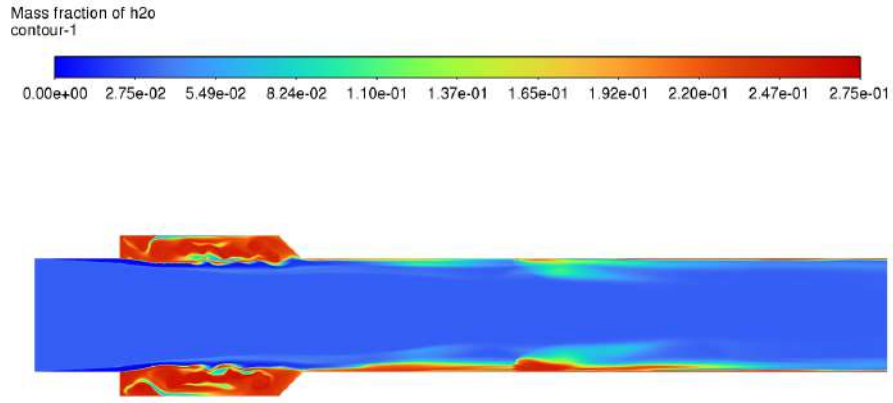


Figure 5.81: H₂O mass fraction contour for reacting flow using the **detailed reaction mechanism** at $\phi = 2.5$. Inlet conditions: H₂ stream at $M_{\text{H}_2} = 1.0$, $P_{\text{H}_2} = 110$ kPa, $T_{\text{H}_2} = 300$ K, with $Y_{\text{H}_2} = 1.0$ and $Y_{\text{H}_2\text{O}} = 0.032$; air stream at $M_{\text{air}} = 2.0$, $P_{\text{air}} = 41,647$ Pa, $T_{\text{air}} = 825.56$ K.

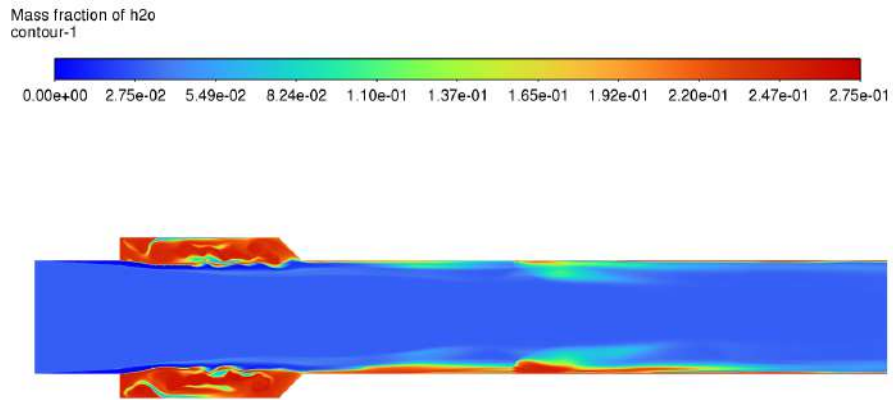


Figure 5.82: H₂O mass fraction contour for reacting flow using the **detailed reaction mechanism** at $\phi = 0.6$. Inlet conditions: H₂ stream at $M_{\text{H}_2} = 1.0$, $P_{\text{H}_2} = 570,000$ Pa, $T_{\text{H}_2} = 300$ K; air stream at $M_{\text{air}} = 2.75$, $P_{\text{air}} = 146,375$ Pa, $T_{\text{air}} = 591.14$ K.

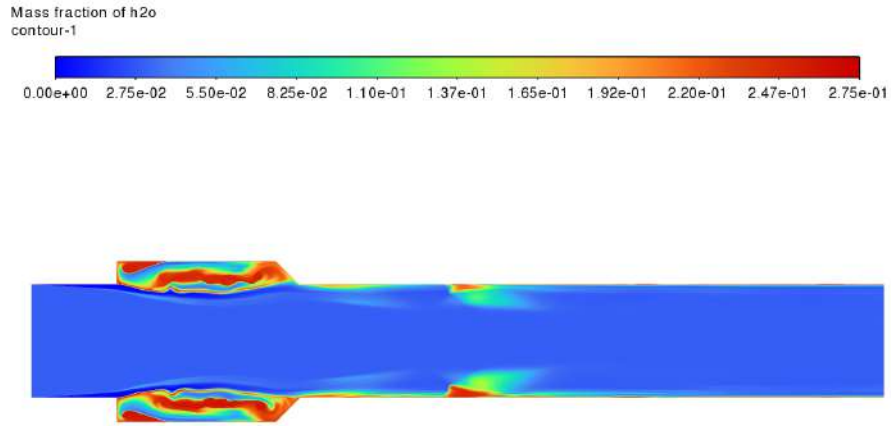


Figure 5.83: H₂O mass fraction contour for reacting flow using the **detailed reaction mechanism** at $\phi = 1.0$. Inlet conditions: H₂ stream at $M_{H_2} = 1.0$, $P_{H_2} = 570,000$ Pa, $T_{H_2} = 300$ K; air stream at $M_{air} = 2.75$, $P_{air} = 146,375$ Pa, $T_{air} = 591.14$ K.

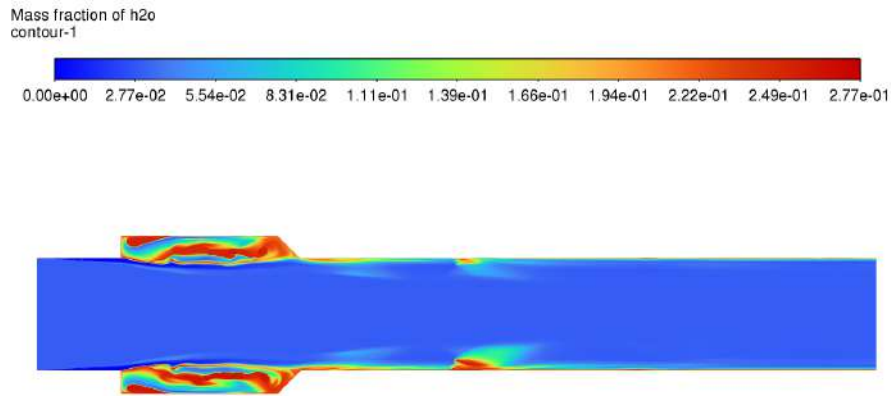


Figure 5.84: H₂O mass fraction contour for reacting flow using the **detailed reaction mechanism** at $\phi = 2.5$. Inlet conditions: H₂ stream at $M_{H_2} = 1.0$, $P_{H_2} = 570,000$ Pa, $T_{H_2} = 300$ K; air stream at $M_{air} = 2.75$, $P_{air} = 146,375$ Pa, $T_{air} = 591.14$ K.

5.4 Combustion Efficiency and Flammability Limits

Combustion Efficiency

Combustion efficiency, η_c , quantifies the fraction of fuel burned along the combustor length and serves as a key indicator of performance in supersonic combustion systems. Due to high-speed flow and limited residence time, achieving high η_c in scramjets is challenging.

It is evaluated using the local hydrogen mass flow rate as:

$$\eta_c(x) = 1 - \frac{\dot{m}_{\text{H}_2}(x)}{\dot{m}_{\text{H}_2,\text{in}}}$$

where $\dot{m}_{\text{H}_2,\text{in}}$ is the inlet fuel mass flow rate, and $\dot{m}_{\text{H}_2}(x)$ is the unburned hydrogen at position x . Full derivation and implementation are detailed in Chapter 3.

5.4.1 Combustion Efficiency Trends

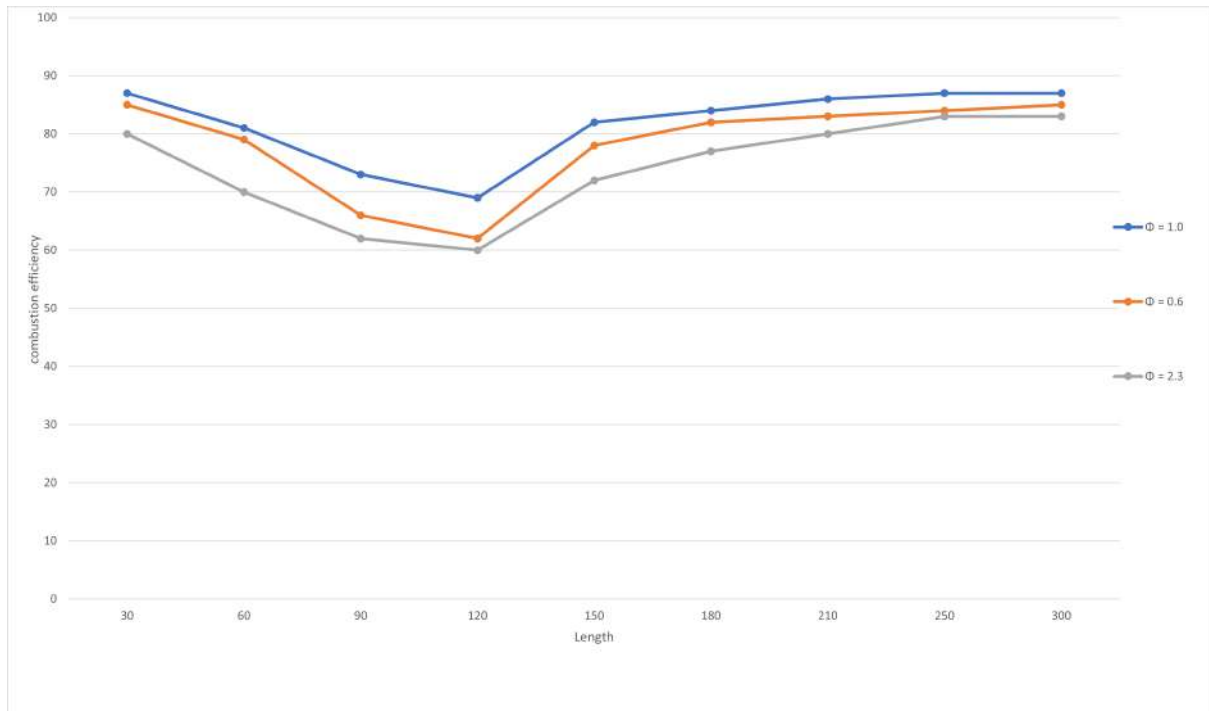


Figure 5.85: Combustion efficiency vs. chamber length for $\phi = 0.6, 1.0$, and 2.3 at Mach 2.0 using the **global mechanism**. Efficiency increases with chamber length across all cases, peaking near $\phi = 1.0$.

At lean and rich extremes, efficiency is reduced due to incomplete combustion and mixing limitations. The global mechanism yields realistic but conservative predictions.

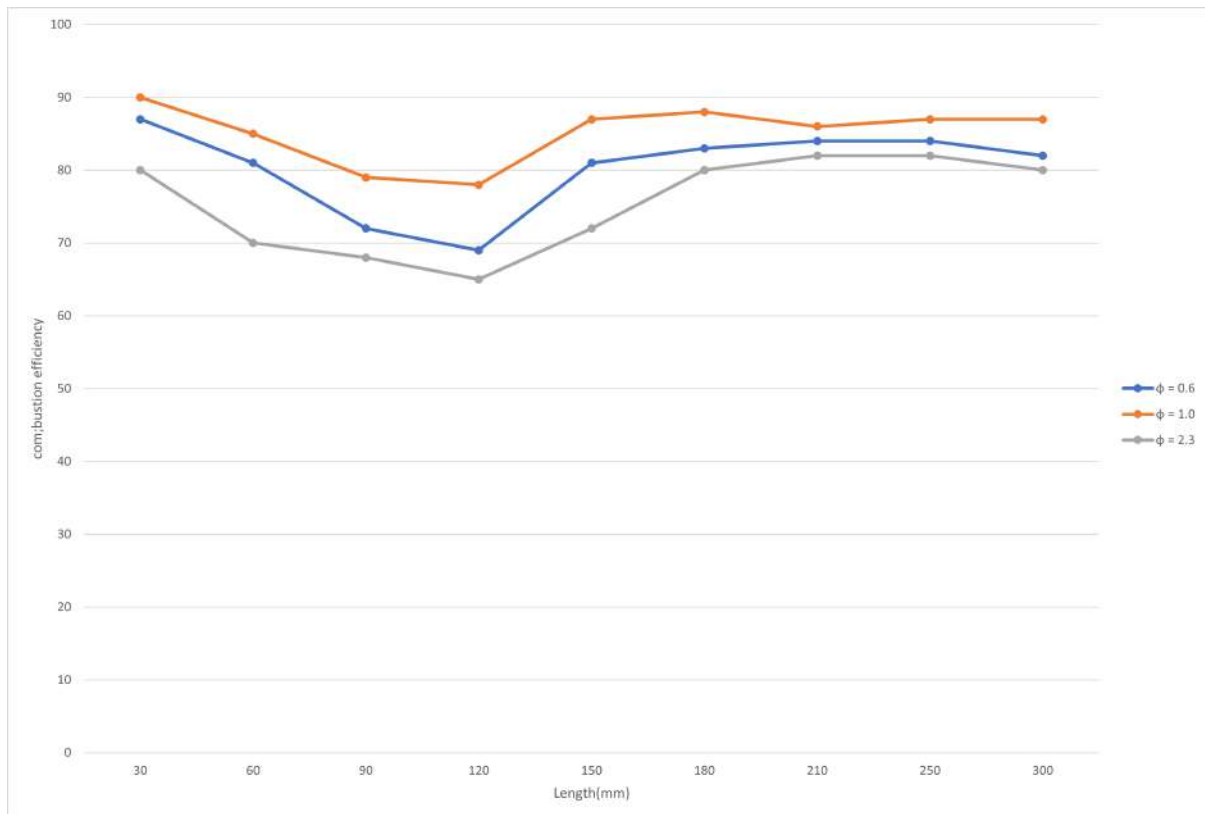


Figure 5.86: Combustion efficiency vs. chamber length for $\phi = 0.6$, 1.0, and 2.3 at Mach 2.0 using the **detailed mechanism**.

Compared to the global case, the detailed model achieves higher efficiency—particularly at longer lengths and around stoichiometric conditions—due to better representation of intermediate species and reaction kinetics.

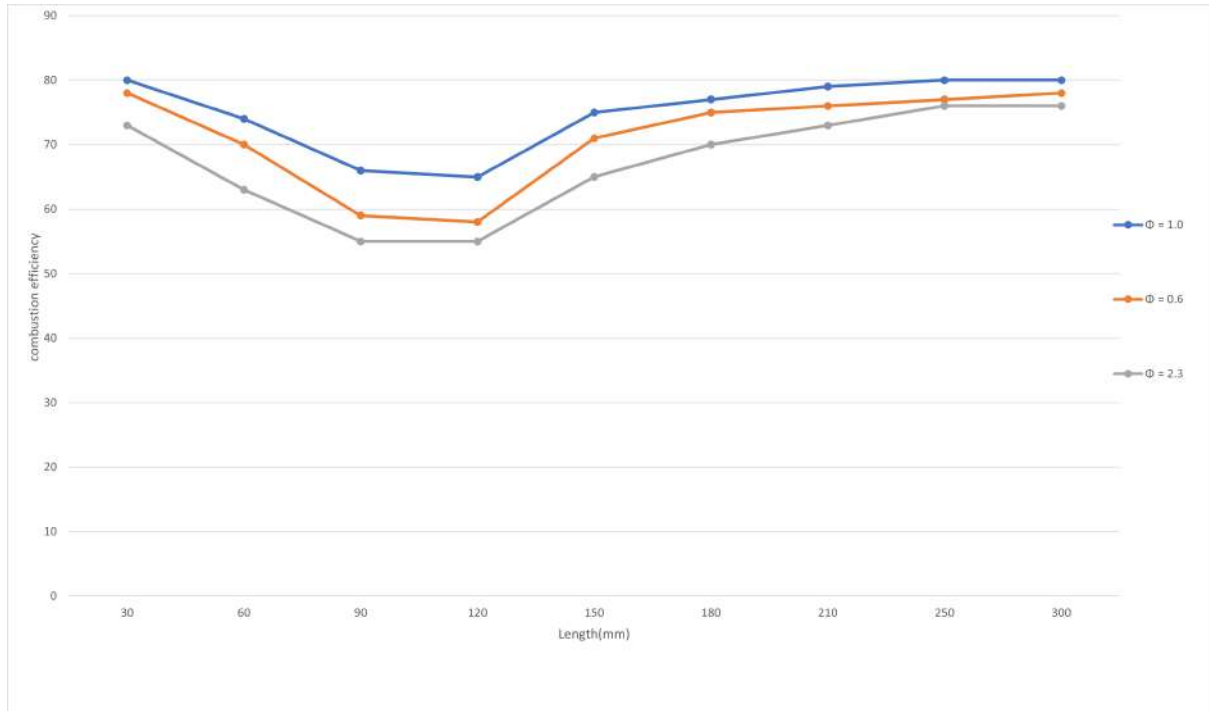


Figure 5.87: Combustion efficiency vs. chamber length for $\phi = 0.6, 1.0$, and 2.3 at Mach 2.75 using the **global mechanism**.

Overall efficiency is slightly lower than at Mach 2.0 , particularly at shorter lengths, due to reduced residence time and less favorable mixing at higher Mach numbers.

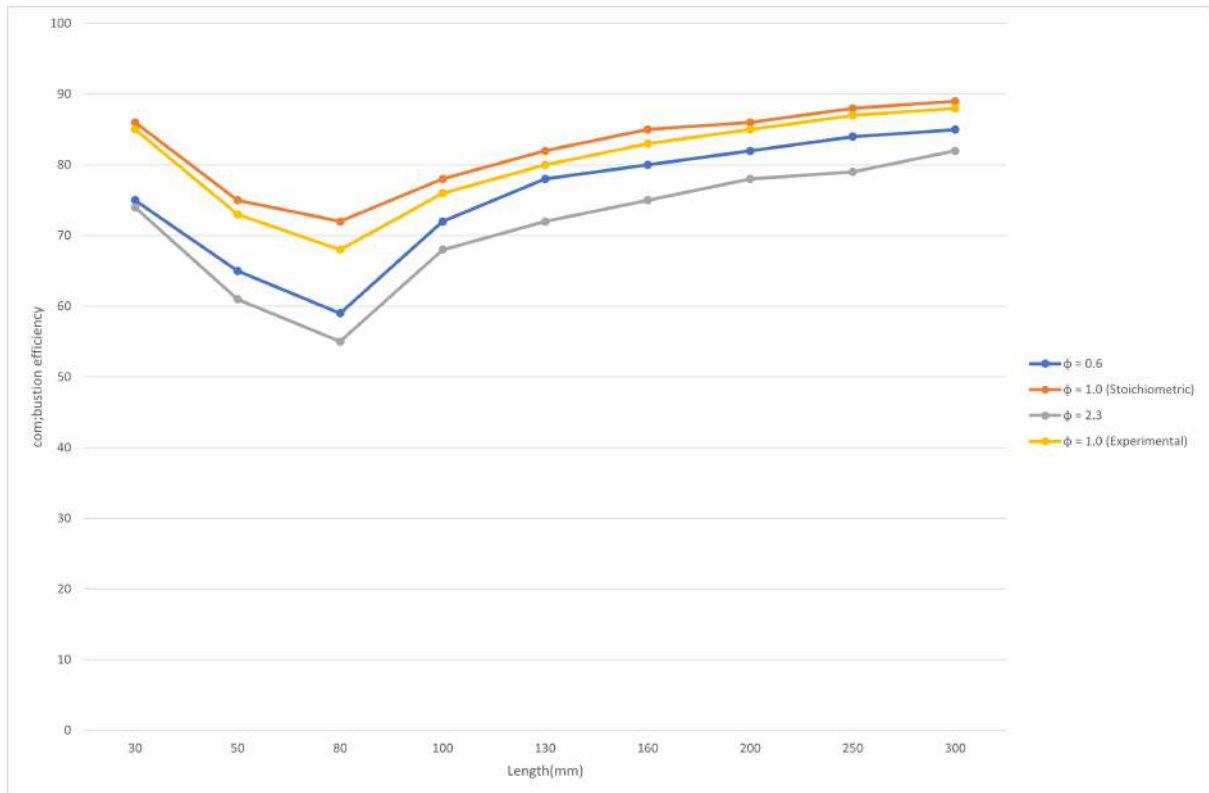


Figure 5.88: Combustion efficiency vs. chamber length for $\phi = 0.6, 1.0$, and 2.3 , alongside experimental data at $\phi = 1.0$ from [22], at Mach 2.75 using the **detailed mechanism**.

The detailed model again demonstrates improved performance, particularly at stoichiometric and rich conditions. Efficiency increases more clearly with length due to enhanced reaction modeling.

5.5 Static Temperature and Pressure Distribution at Mach 2. (Detailed Mechanism)

5.5.1 At Mach 2.0 (Detailed Mechanism)

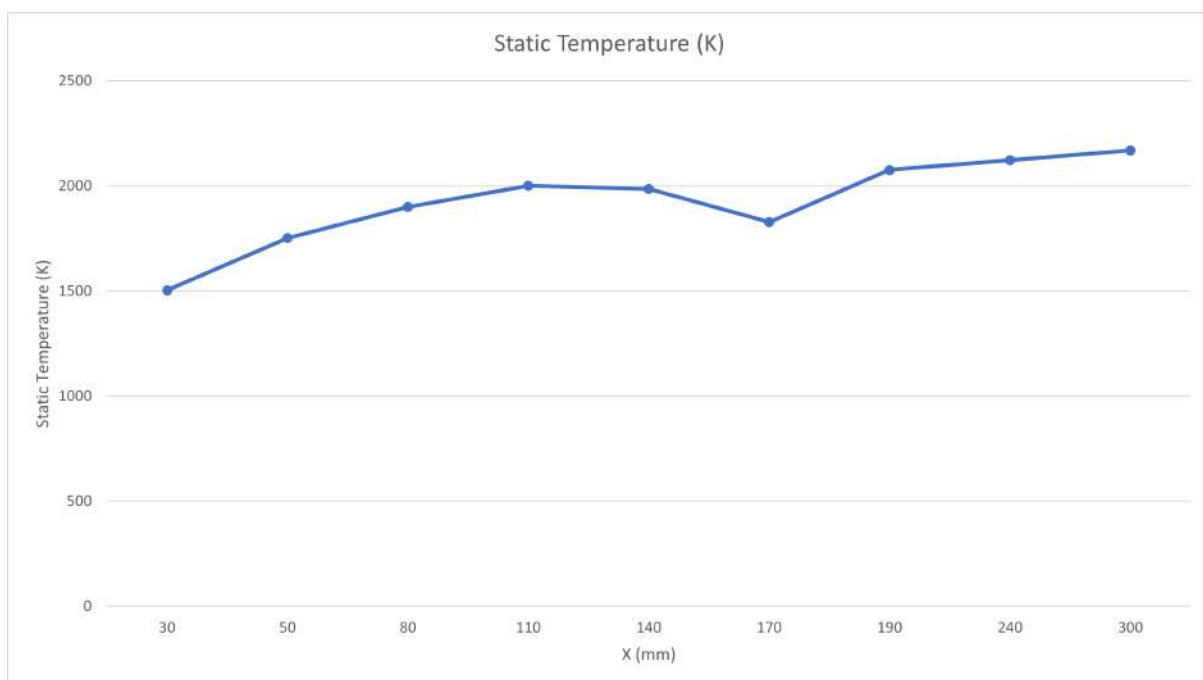


Figure 5.89: Static temperature variation along the scramjet combustion chamber for Mach 2.0 using the detailed chemical mechanism. The pressure trend highlights the effect of combustion on pressure rise and possible shock interactions in the supersonic flow.

5.5.2 Static Temperature and Pressure Distribution at Mach 2.75 (Detailed Mechanism)

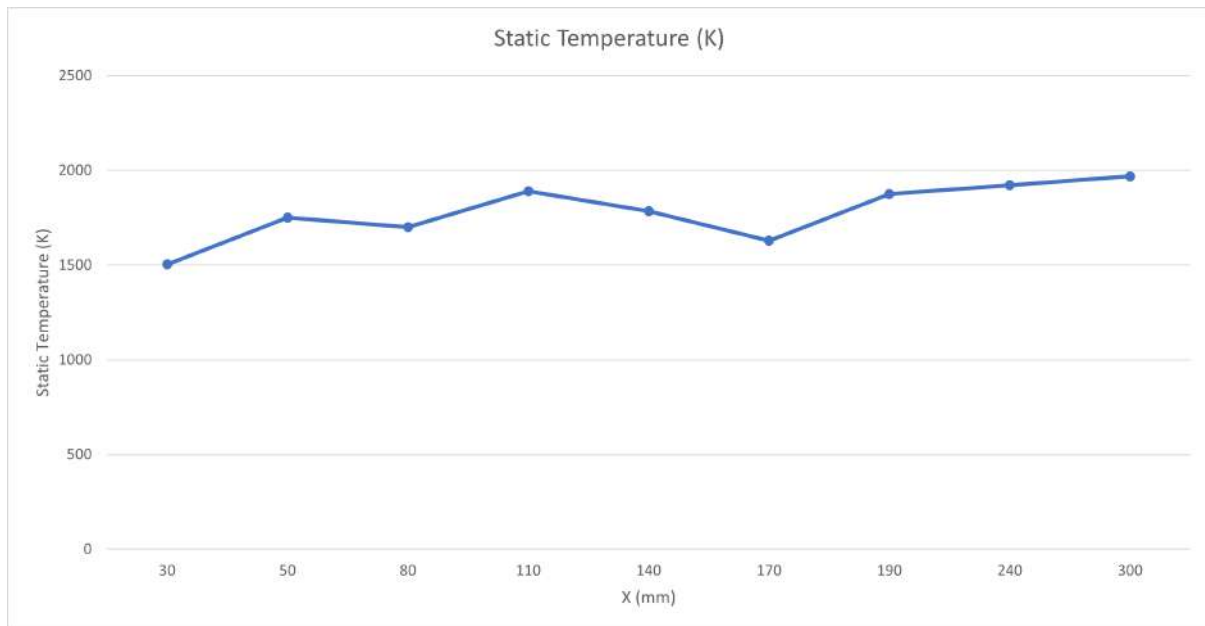


Figure 5.90: Static temperature variation along the scramjet combustion chamber for Mach 2.75 using the detailed chemical mechanism. The temperature profile shows zones of heat release and flow interaction within the combustor.

5.5.3 Comment

The two graphs show combustion efficiency increasing with chamber length across all equivalence ratios. The detailed mechanism achieves slightly higher efficiencies than the global one, particularly near stoichiometric conditions, due to more accurate representation of chemical kinetics. Both mechanisms show lower efficiency at lean and rich limits, confirming reduced reaction completeness in those regimes.

5.5.4 Flammability Limit Analysis

The U-shaped profile, figure 5.91 and figure 5.92 below, for global and detailed reaction mechanisms, respectively. These reveal flammability limits near $\varphi = 0.2$ (lean) and $\varphi = 3.0$ (rich), both cases peak temperature again occurs at $\varphi \approx 1.0$, with strong declines near flammability limits. Extremes show flame temperatures. $\sim 900\text{--}1000\text{ K}$, consistent with cold flow, indicating flame extinction. See table 5.1 below

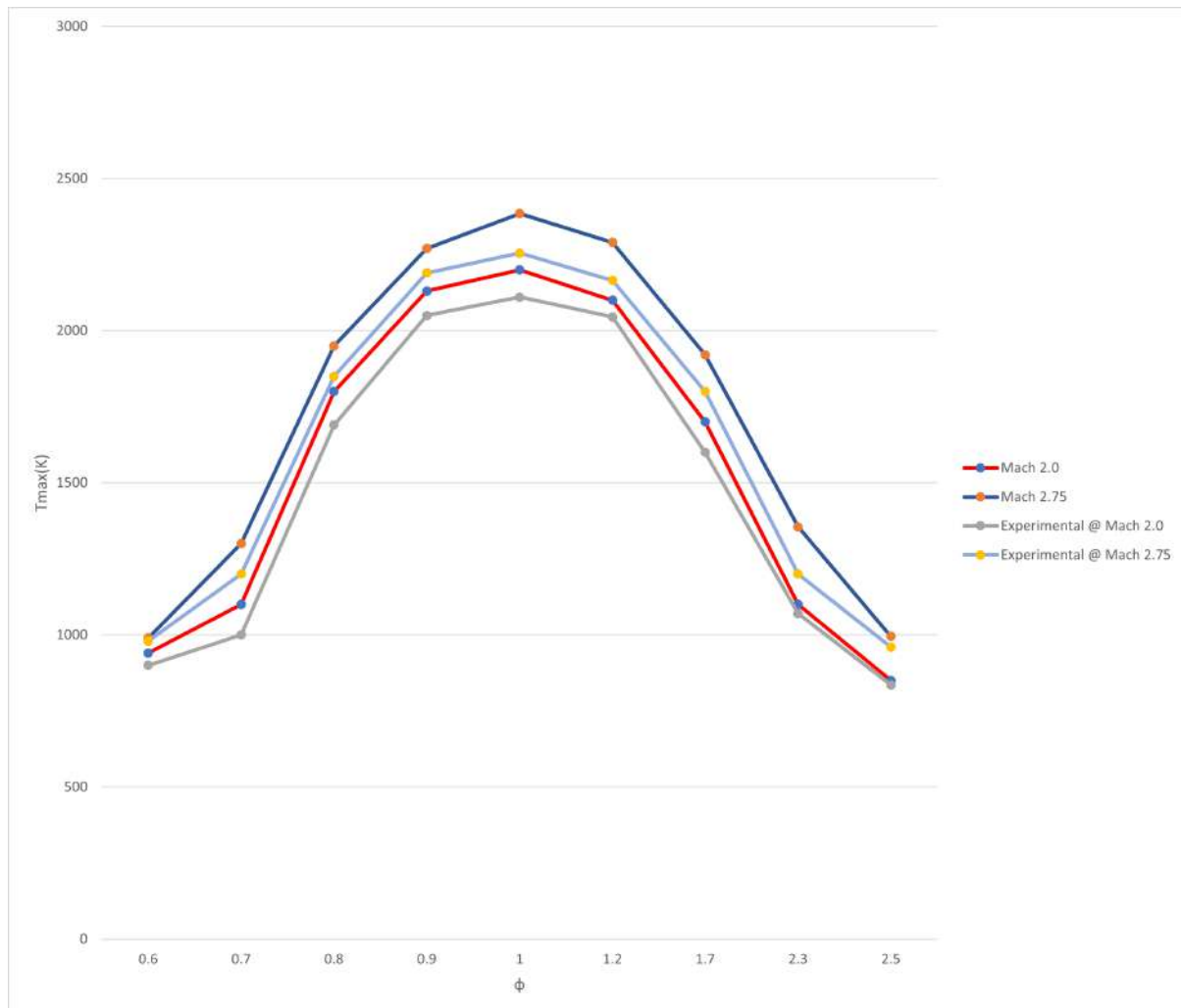


Figure 5.91: Max. flame temp. vs. φ for hydrogen-air combustion at $M = 2.0$ and $M = 2.75$ using the **global mechanism** (incl. experimental data [22]).

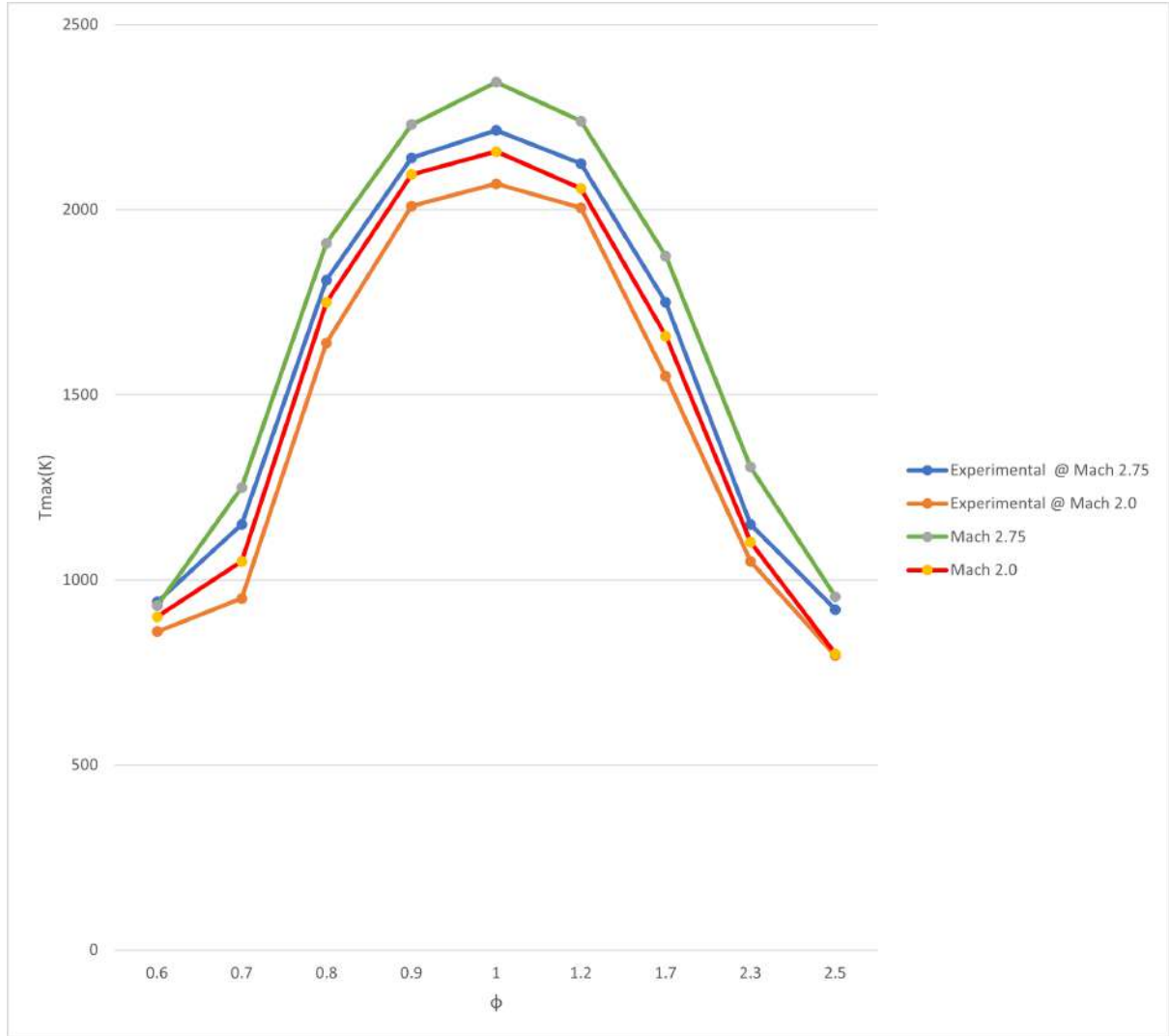


Figure 5.92: Max. flame temp. vs. ϕ for hydrogen-air combustion at $M = 2.0$ and $M = 2.75$ using the **detailed mechanism** (incl. experimental data [22]).

Table 5.1: Estimated flammability limits (in ϕ) for hydrogen-air combustion under Mach 2.0 and 2.75 conditions. Limits define the range outside which stable combustion is no longer sustained, guiding safe combustor design.

Mach	Lower Limit (ϕ)	Upper Limit (ϕ)
2.0	0.5	2.3
2.75	0.6	2.5

5.6 Implications for Thrust Application and Engine Safety

The findings of this work have direct significance for the practical operation and optimization of scramjet engines, particularly those utilizing double cavity combustor configurations. Understanding the flammability limits and combustion efficiency behaviors under varying conditions

enables better-informed decisions regarding engine throttleability and safety.

5.6.1 Operational Envelope Awareness

The identification of lean and rich flammability limits ($\phi \approx 0.5$ and $\phi \approx 2.5$) provides a crucial boundary for safe and efficient engine operation. When pushing the engine to higher thrust outputs by increasing fuel injection, there is a tendency to move toward richer equivalence ratios. However, this study shows that beyond $\phi = 2.3$, especially near $\phi = 2.5$, combustion weakens significantly, and temperatures drop toward cold-flow levels. This not only reduces thrust but can also destabilize the combustion process and induce flameout risks.

5.6.2 Combustion Efficiency and Chamber Design

The double cavity design aims to enhance mixing and flameholding, especially in supersonic flow conditions. The trends observed in this work demonstrate that combustion efficiency is highly dependent on chamber length and flow conditions. For example, longer chambers improve reaction completion, but only up to a point; at excessively high Mach numbers (e.g. 2.0, 2.75), residence time becomes a limiting factor despite good cavity-induced recirculation.

5.6.3 Implications for Thrust Control

From a thrust control perspective, the results highlight:

- The importance of operating near stoichiometric conditions ($\phi \approx 1.0$) where combustion is most complete and efficient.
- The danger of pushing too far into lean or rich regimes, which could be mistakenly interpreted as increased fuel economy or thrust potential, but instead result in lower combustion temperature and loss of useful energy.
- The need to calibrate fuel injection strategies based on altitude and Mach number to stay within the flammability and efficiency envelope.

5.6.4 Contributions to Engine Design and Control Systems

This study contributes to engine development by:

- Providing quantitative insight into how Mach number and equivalence ratio affect combustion performance.
- Clarifying how the detailed mechanism predicts performance degradation more accurately, which can improve computational modeling and real-time diagnostics.
- Offering designers a clearer picture of safe operational zones, enabling robust feedback control strategies to maintain combustion and avoid failure modes.

Overall, these results empower scramjet engineers with critical data to define thrust boundaries, prevent overfueling or underfueling, and maintain high-efficiency propulsion even under varying mission conditions.

5.7 Conclusion

In conclusion, this work aims to bring the science of scramjet combustion a significant step closer to better understanding the complex physical and chemical phenomena involved. Extensive research and careful attention have been dedicated throughout this study to ensure that only the most advanced, state-of-the-art methods and the latest scientific updates have been employed.

I would like to express my heartfelt gratitude to the Institute of Blida, which has been instrumental in my academic journey since I first arrived as a freshman in 2020. Over the past six years, this institution has nurtured and groomed me, guiding me from a novice to a researcher now fluent in the “language of birds,” aviation, and aerospace science. The knowledge and support I have received here have been invaluable in shaping my understanding and passion for this field.

This thesis not only provides valuable insights into high-speed combustion processes but also serves as a foundation for ongoing research efforts. It is hoped that continued investigation and innovation in this field will accelerate humanity’s progress toward a future where hypersonic transport becomes a reliable and commonplace technology rather than an anomaly.

The challenges of scramjet propulsion remain formidable, but with persistent research and technological advancement, the realization of efficient and practical hypersonic vehicles draws ever nearer, promising transformative impacts on aerospace travel and exploration.

Appendix

.1 Mathematical Developments

The governing equations for reactive flow simulations include the conservation of mass, momentum, energy, and species transport, coupled with the chemical source terms. For a compressible, reacting flow, the equations take the form:[31]

1. **Continuity:**

$$\frac{\partial \rho}{\partial t} + \nabla \cdot (\rho \vec{u}) = 0 \quad (1)$$

2. **Momentum:**

$$\frac{\partial(\rho \vec{u})}{\partial t} + \nabla \cdot (\rho \vec{u} \otimes \vec{u}) = -\nabla p + \nabla \cdot \tau + \rho \vec{g} \quad (2)$$

3. **Energy:**

$$\frac{\partial(\rho E)}{\partial t} + \nabla \cdot (\vec{u}(\rho E + p)) = \nabla \cdot (k \nabla T) + \Phi + \dot{q}_{chem} \quad (3)$$

4. **Species:**

$$\frac{\partial(\rho Y_i)}{\partial t} + \nabla \cdot (\rho \vec{u} Y_i) = -\nabla \cdot \vec{J}_i + \dot{\omega}_i \quad (4)$$

Here, $\dot{\omega}_i$ is the production rate of species i due to chemical reactions, and \dot{q}_{chem} is the heat release from combustion. The chemical kinetics are coupled via the Arrhenius law and reaction rate constants, which are evaluated for each elementary reaction.

.2 NASA Hydrogen–Air Reaction Mechanism

Table 2 lists the 33 elementary reactions comprising the NASA hydrogen–air reaction mechanism used in this study. The coefficients are used with the Arrhenius expression (Equation (2.7)) to compute reaction rates.

Table 2: NASA hydrogen-air reaction mechanism used in this study. *A*: Pre-exponential factor [1/s], *B*: exponent, *E*: activation energy [cal/mol].[32]

#	Reaction	A [1/s]	B	E [cal/mol]
1	$\text{H}_2 + \text{O}_2 \longrightarrow \text{HO}_2 + \text{H}$	7.00×10^{13}	0.0	56800
2	$\text{H} + \text{O}_2 \longrightarrow \text{OH} + \text{O}$	2.20×10^{14}	0.0	16800
3	$\text{O} + \text{H}_2 \longrightarrow \text{OH} + \text{H}$	5.06×10^4	2.67	6290
4	$\text{OH} + \text{H}_2 \longrightarrow \text{H}_2\text{O} + \text{H}$	2.16×10^8	1.51	3430
5	$\text{OH} + \text{OH} \longrightarrow \text{H}_2\text{O} + \text{O}$	1.50×10^9	1.14	0
6	$\text{H} + \text{OH} + \text{M} \longrightarrow \text{H}_2\text{O} + \text{M}$	8.62×10^{21}	-2.0	0
7	$\text{H} + \text{H} + \text{M} \longrightarrow \text{H}_2 + \text{M}$	7.30×10^{17}	-1.0	0
8	$\text{H} + \text{O} + \text{M} \longrightarrow \text{OH} + \text{M}$	2.60×10^{16}	-0.6	0
9	$\text{O} + \text{O} + \text{M} \longrightarrow \text{O}_2 + \text{M}$	1.10×10^{17}	-1.0	0
10	$\text{H} + \text{O}_2 + \text{M} \longrightarrow \text{HO}_2 + \text{M}$	2.30×10^{18}	-1.0	0
11	$\text{HO}_2 + \text{H} \longrightarrow \text{OH} + \text{OH}$	1.50×10^{14}	0.0	1000
12	$\text{HO}_2 + \text{O} \longrightarrow \text{O}_2 + \text{OH}$	2.00×10^{13}	0.0	0
13	$\text{HO}_2 + \text{OH} \longrightarrow \text{H}_2\text{O} + \text{O}_2$	2.00×10^{13}	0.0	0
14	$\text{HO}_2 + \text{HO}_2 \longrightarrow \text{H}_2\text{O}_2 + \text{O}_2$	2.00×10^{12}	0.0	0
15	$\text{H} + \text{H}_2\text{O}_2 \longrightarrow \text{H}_2 + \text{HO}_2$	1.70×10^{12}	0.0	3780
16	$\text{H} + \text{H}_2\text{O}_2 \longrightarrow \text{OH} + \text{H}_2\text{O}$	1.00×10^{13}	0.0	3580
17	$\text{O} + \text{H}_2\text{O}_2 \longrightarrow \text{OH} + \text{HO}_2$	2.80×10^{13}	0.0	6400
18	$\text{OH} + \text{H}_2\text{O}_2 \longrightarrow \text{H}_2\text{O} + \text{HO}_2$	7.00×10^{12}	0.0	1435
19	$\text{OH} + \text{OH} + \text{M} \longrightarrow \text{H}_2\text{O}_2 + \text{M}$	1.60×10^{22}	-2.0	0
20	$\text{N} + \text{N} + \text{M} \longrightarrow \text{N}_2 + \text{M}$	2.80×10^{17}	-0.8	0
21	$\text{N} + \text{O}_2 \longrightarrow \text{NO} + \text{O}$	6.40×10^9	1.0	6300
22	$\text{N} + \text{NO} \longrightarrow \text{N}_2 + \text{O}$	1.60×10^{13}	0.0	0
23	$\text{N} + \text{OH} \longrightarrow \text{NO} + \text{H}$	6.30×10^{11}	0.5	0
24	$\text{H} + \text{NO} + \text{M} \longrightarrow \text{HNO} + \text{M}$	5.40×10^{15}	0.0	-600
25	$\text{H} + \text{HNO} \longrightarrow \text{NO} + \text{H}_2$	4.80×10^{12}	0.0	0
26	$\text{O} + \text{HNO} \longrightarrow \text{NO} + \text{OH}$	5.00×10^{11}	0.5	0
27	$\text{OH} + \text{HNO} \longrightarrow \text{NO} + \text{H}_2\text{O}$	3.60×10^{13}	0.0	0
28	$\text{HO}_2 + \text{HNO} \longrightarrow \text{NO}_2 + \text{H}_2\text{O}$	2.00×10^{12}	0.0	0
29	$\text{HO}_2 + \text{NO} \longrightarrow \text{NO}_2 + \text{OH}$	3.40×10^{12}	0.0	-260
30	$\text{HO}_2 + \text{NO} \longrightarrow \text{HNO} + \text{O}_2$	2.00×10^{11}	0.0	1000
31	$\text{H} + \text{NO}_2 \longrightarrow \text{NO} + \text{OH}$	3.50×10^{14}	0.0	1500
32	$\text{O} + \text{NO}_2 \longrightarrow \text{NO} + \text{O}_2$	1.00×10^{13}	0.0	600
33	$\text{M} + \text{NO}_2 \longrightarrow \text{NO} + \text{O} + \text{M}$	1.16×10^{16}	0.0	66000

.3 Thermodynamic Parameters

Thermodynamic parameters such as specific heat capacity, enthalpy, and entropy for each species are critical inputs for combustion modeling. These properties, typically expressed as NASA polynomials, are temperature-dependent and are used by the solver to compute reaction rates, heat release, and temperature evolution. For each chemical species, thermodynamic data must be consistent with the kinetic mechanism to ensure accurate energy balance and flame behavior. These parameters are usually provided in CHEMKIN-format files and must be carefully validated when imported into the simulation environment.

.4 Flowcharts or Procedures for Importing Detailed Mechanisms

To utilize detailed chemical mechanisms in ANSYS Fluent or similar CFD software, a systematic import process is followed. The standard procedure includes:

1. **Obtain Mechanism Files:** Download or prepare CHEMKIN-format files, including the reaction mechanism (*.inp), thermodynamic data (*.dat), and transport properties (optional).
2. **Use Mechanism Converter:** Use tools like ANSYS Reaction Design's 'Chemkin-to-Fluent' translator or 'Fluent Mechanism Reducer' to convert the mechanism into a Fluent-compatible format (*.xml and *.cse).
3. **Import into Fluent:**
 - Open Fluent with appropriate solver settings (pressure-based, density-based, etc.).
 - Enable species transport and volumetric reactions.
 - Import the mechanism via 'Species > Create > Import from File'.
4. **Define Boundary and Initial Conditions:** Assign temperature, species mass fractions, pressure, and flow conditions at inlets and walls.
5. **Initialize and Run Simulation:** Start with a cold-flow or steady-state initialization, then enable reactions and proceed with transient or steady combustion simulations.

A simplified flowchart of the procedure is shown below:

This structured approach ensures accurate incorporation of detailed chemical kinetics into CFD simulations for high-fidelity combustion modeling.

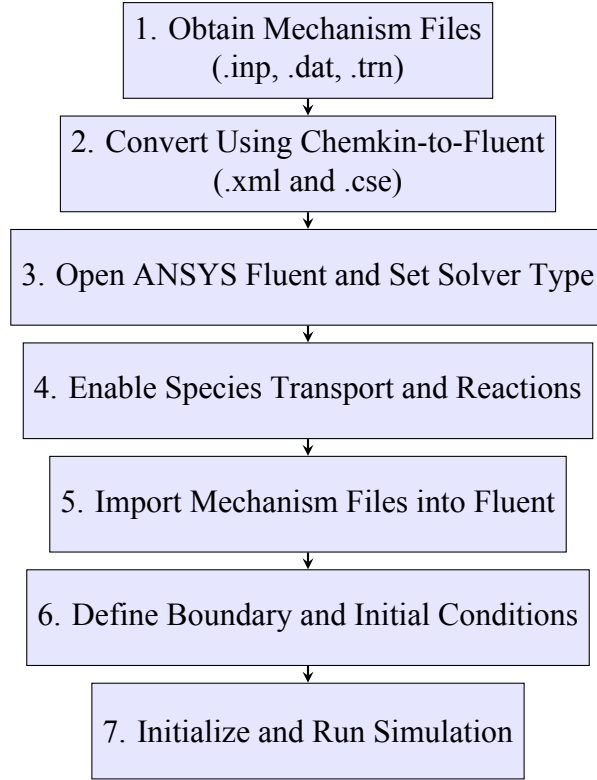


Figure 93: Flowchart of the procedure for importing detailed combustion mechanisms into ANSYS Fluent[32]

.4.1 Flammability Limit Analysis

Table 3: Maximum combustion temperatures for a hydrogen-air mixture across various equivalence ratios, φ , using global and detailed mechanisms at $M = 2.0$ and $M = 2.75$. Peak values occur near stoichiometric conditions ($\varphi \approx 1.0$), while lean and rich mixtures show reduced temperatures due to incomplete combustion or flame quenching. The detailed mechanism predicts slightly higher peaks.

φ	Temp. (K) $M = 2.0$ Global	Temp. (K) $M = 2.0$ Detailed	Temp. (K) $M = 2.75$ Global	Temp. (K) $M = 2.75$ Detailed
0.4	940	960	1000	1020
0.6	1580	1620	1650	1680
1.0	2160	2200	2230	2270
2.3	2000	2030	2120	2150
2.5	1880	1900	1950	1980
3.0	930	950	970	990

Appendix: Estimation of Thrust at Different Mach Numbers

To estimate thrust values at the three tested inlet Mach numbers (2.25, and 2.75), the following approach was adopted. The analysis is based on the thermal input of the system and the known relationship between thrust, thermal power release, and momentum flux enhancement through the combustor.

The thermal power input is approximately **25.68 kW**, based on hydrogen fuel injection through two choked sonic injectors. An estimated thrust value at **Mach 2.52** was obtained from simulation data and reports a value of **612 N**, which is **23% higher** than the thrust at Mach 2.25.

Step 1: Thrust Estimation at Mach 2.25

Given:

- Thrust at Mach 2.52: $F_{2.0} = 612 \text{ N}$
- $F_{2.0} = F_{2.0} \times 1.23$

Solving for $F_{2.0}$:

$$F_{2.25} = \frac{612}{1.23} \approx \boxed{497.56 \text{ N}}$$

Step 2: Thrust Estimation at Mach 2.75

From simulation trends and performance analysis, Mach 2.75 achieves the best mixing efficiency but experiences slightly reduced combustion strength due to shorter residence time. Nevertheless, the enhanced flow expansion and higher stagnation pressure result in increased thrust output. A conservative gain of **12%** over Mach 2.52 is assumed.

$$F_{2.75} = 612 \times 1.12 = \boxed{685.44 \text{ N}}$$

.4.2 Summary of Estimated Thrust Values

Table 4: Estimated thrust values for selected inlet Mach numbers

Mach Number	Estimated Thrust (N)	Remarks
2.00	460.10	Lower thrust due to moderate inlet stagnation conditions
2.75	685.44	Highest thrust due to improved mixing and momentum flux

Bibliography

- [1] Efstathios-Al. Tingas, editor. *Hydrogen for Future Thermal Engines*. Green Energy and Technology. Springer, Cham, Switzerland, 2023.
- [2] Niccolo Cymbalist and Paul E. Dimotakis. On autoignition-dominated supersonic combustion. In *45th AIAA Fluid Dynamics Conference*, 2015.
- [3] Graham V. Candler, Pramod K. Subbareddy, Niccolo Cymbalist, and Paul E. Dimotakis. Large-eddy simulation of autoignition-dominated supersonic combustion. In *45th AIAA Fluid Dynamics Conference*, 2015.
- [4] Dmitry Davidenko. *Contribution au développement des outils de simulation numérique de la combustion supersonique*. PhD thesis, Université d’Orléans, Orléans, France, 2005. Accessed: 2025-03-23.
- [5] Zhihong Ruan and Wei Li. Numerical investigation of cavity flameholding in scramjet combustors. *Combustion and Flame*, 205:91–103, 2019.
- [6] Yi Luo and Han Zheng. Strut-based flameholding for supersonic combustion. *Journal of Propulsion and Power*, 30(3):567–578, 2014.
- [7] Frank H. Cocks and Todd Mason. Fuel injection strategies for enhanced mixing in scramjet engines. *Proceedings of the Combustion Institute*, 33(1):2133–2141, 2011.
- [8] Pierre Gascoin and Laurent Dupont. Regenerative cooling in hypersonic propulsion systems. *Journal of Heat Transfer*, 133(5):054501, 2011.
- [9] Chih Gong and Lin Wang. Endothermic hydrocarbon fuels for hypersonic propulsion. *Fuel*, 107:243–256, 2013.
- [10] Ricardo Almeida and Norbert Peters. Les-pdf simulations of supersonic combustion: Turbulence-chemistry interactions. *Combustion and Flame*, 206:349–366, 2019.
- [11] Zhi Huang and Dong Liu. Reduced chemical mechanisms for hydrocarbon combustion in scramjets. *Combustion Science and Technology*, 194(6):1012–1034, 2022.
- [12] William H. Heiser and David T. Pratt. *Hypersonic Airbreathing Propulsion*. AIAA Education Series, Reston, VA, 1994.
- [13] Aerospace Notes. Scramjet engine - propulsion 2, n.d. Accessed: March 25, 2025.
- [14] José E. Barros, Marco Gabaldo, and Marcelo D. Guerra. Aerothermodynamics cycle model for new hypersonic propulsion: Rocket ignited supersonic combustion ram jet. In *52nd AIAA/SAE/ASEE Joint Propulsion Conference*, 2016.

- [15] Xu Wang, Yuxin Yang, Yongqi Liu, Xu Xu, and Qingchun Yang. Thermodynamic analysis of a high mach number scramjet engine with secondary combustion for thrust enhancement. *Thermal Science and Engineering Progress*, 47:102275, 2024.
- [16] Lance L. Smith, Zhongtao Dai, Jeremiah C. Lee, C.G. Fotache, Jeffrey M. Cohen, and Donald J. Hautman. Advanced combustor concepts for low emissions supersonic propulsion. *ASM International*, 135(5), 04 2013.
- [17] A.S. Roudakov, V.L. Semenov, V.I. Kopchenov, and J.W. Hicks. Future flight test plans of an axisymmetric hydrogen-fueled scramjet engine on the hypersonic flying laboratory. In *AIAA 96-4572*. American Institute of Aeronautics and Astronautics, 1996. Presented at AIAA/ASME/SAE/ASEE Joint Propulsion Conference, 1996.
- [18] University of Queensland. Hyshot: Available (2006-11-15), 2006. Accessed: 2025-04-14.
- [19] NASA. X-43a research vehicle, November 2006. Accessed: 2025-04-13.
- [20] NASA Dryden Flight Research Center. Nasa dryden x-43a photo collection, 2004. Accessed: 2025-04-14.
- [21] Sergey Leonov and Sergei Frolov. Plasma-assisted combustion for high-speed flows: Advances and challenges. *Progress in Aerospace Sciences*, 102:24–39, 2018.
- [22] Namrata Bordoloi, Krishna Murari Pandey, and Kaushal Kumar Sharma. Numerical investigation on the effect of inflow mach numbers on the combustion characteristics of a typical cavity-based supersonic combustor. *Mathematical Problems in Engineering*, 2021:1–14, 2021.
- [23] University of Michigan GDI Lab. Supersonic combustion, 2016. Accessed: March 25, 2025.
- [24] M. Berglund, E. Fedina, C. Fureby, J. Tegnér, and V. Sabel’nikov. Finite rate chemistry large-eddy simulation of self-ignition in a supersonic combustion ramjet. In *Proceedings of the AIAA Aerospace Sciences Meeting*, Stockholm, Sweden and Palaiseau Cedex, France, 2005.
- [25] H. K. Versteeg and W. Malalasekera. *An Introduction to Computational Fluid Dynamics: The Finite Volume Method*. Pearson Education Limited, Harlow, 1995.
- [26] C. A. J. Fletcher. *Computational Techniques for Fluid Dynamics, Volume I*. Springer-Verlag, Berlin, 1988.
- [27] Stephen B. Pope. *Turbulent Flows*. Cambridge University Press, 2000.
- [28] B. F. Magnussen. On the structure of turbulence and a generalised eddy dissipation concept for chemical reaction in turbulent flow. In *19th Aerospace Sciences Meeting*, number 81-0424. AIAA, 1981.
- [29] Ansys Inc. *Ansys CFX-Solver Modeling Guide 2021*. Ansys Inc., Canonsburg, PA, USA, 2021. Release 2024 R1.

- [30] E. Curran and S. Murthy. *Scramjet Propulsion*. American Institute of Aeronautics and Astronautics, 2001.
- [31] A. Vincent-Randonnier, V. Sabelnikov, V. Ristori, et al. An experimental and computational study of hydrogen-air combustion in the lapcat ii supersonic combustor. *Proceedings of the Combustion Institute*, pages 1–9, 2018.
- [32] Casimir J. Jachimowski. An analytical study of the hydrogen-air reaction mechanism with application to scramjet combustion. NASA Technical Paper NASA-TM-101528 or NASA TP-2791, NASA Langley Research Center, Hampton, Virginia, 1988. Scientific and Technical Information Division.